YEAR END TECHNICAL REPORT
September 17, 2013 to May 17, 2014

Chemical Process Alternatives for Radioactive Waste

Date submitted:

June 30, 2014

Principal Investigator:

Leonel E. Lagos, Ph.D., PMP®

.

Florida International University Collaborators:

Dwayne McDaniel, Ph.D., P.E. (Project Manager)
Amer Awwad, M.S., P.E.
Seckin Gokaltun, Ph.D.
Romani Patel, M.S.
Tomas Pribanic, M.S., P.E.
David Roelant, Ph.D.
Jario Crespo
DOE Fellows

Submitted to:

U.S. Department of Energy
Office of Environmental Management
Under Cooperative Agreement No. DE-EM0000598

FIU | Applied Research Center
FLORIDA INTERNATIONAL UNIVERSITY

Addendum:

This document represents one (1) of five (5) reports that comprise the Year End Reports for the period of September 17, 2013 to May 17, 2014 prepared by the Applied Research Center at Florida International University for the U.S. Department of Energy Office of Environmental Management (DOE-EM) under Cooperative Agreement No. DE-EM0000598.

The complete set of FIU's Year End Reports for this reporting period includes the following documents and are available at the DOE Research website for the Cooperative Agreement between the U.S. Department of Energy Office of Environmental Management and the Applied Research Center at Florida International University (http://doeresearch.fiu.edu):

Project 1: Chemical Process Alternatives for Radioactive Waste
Document number: FIU-ARC-2014-800000393-04b-233

Project 2: Rapid Deployment of Engineered Solutions for Environmental Problems
Document number: FIU-ARC-2014-800000438-04b-223

Project 3: Remediation and Treatment Technology Development and Support
Document number: FIU-ARC-2014-800000439-04b-225

Project 4: Waste and D&D Engineering and Technology Development
Document number: FIU-ARC-2014-800000440-04b-220

Project 5: DOE-FIU Science & Technology Workforce Development Initiative
Document number: FIU-ARC-2014-800000394-04b-079

Each document will be submitted to OSTI separately under the respective project title and document number as shown above.

TABLE OF CONTENTS

LIST OF FIGURES

PROJECT 1 OVERVIEW

The Department of Energy's (DOE's) Office of Environmental Management (EM) has a mission to clean up the contaminated soils, groundwater, buildings and wastes generated over the past 60 years by the R&D and production of nuclear weapons. The nation's nuclear weapons complex generated complex radioactive and chemical wastes. This project is focused on tasks to support the safe and effective storage, retrieval and treatment of high-level waste (HLW) from tanks at the Hanford and Savannah River Sites. The objective of this project is to provide the sites with modeling, pilot-scale studies on simulated wastes, technology assessment and testing, and technology development to support critical issues related to HLW retrieval and processing. Florida International University (FIU) engineers work directly with site engineers to plan, execute and analyze results of applied research and development.

During FIU Year 4 (FY13), Project 1, titled "Chemical Process Alternatives for Radioactive Waste", focused on four tasks related to HLW research at FIU. Detailed task descriptions and deliverables and milestones can be found in the Project Technical Plan (Appendix 1). These tasks are listed below and this report contains a detailed summary of the work accomplished for FIU Year 4 (FY13).

Task 2 - Pipeline Unplugging and Plug Prevention

Subtask 2.1 - Development of Alternative Unplugging Technologies: The objective of this task is to qualify (test & evaluate) pipeline unplugging technologies for deployment at the DOE sites. Additionally, FIU has worked closely with engineers from Hanford's tank farms and Waste Treatment and Immobilization Plant on developing alternative pipeline unplugging technologies. After extensive evaluation of available commercial unplugging technologies in the previous years, two novel approaches are being developed at FIU including a peristaltic crawler and an asynchronous pulsing method.

Subtask 2.2 - Computational Simulation and Evolution of HLW Pipeline Plugs: The objective of this task is to develop a model that is aimed at predicting the formation of plugs in HLW lines with an emphasis on the effects of pipeline geometry. The goal is to develop a tool that can assist in providing guidelines to plug prevention.

Task 17 - Advanced Topics for HLW Mixing and Processing

Subtask 17.1 - Multiple-Relaxation-Time Lattice Boltzmann Model for Multiphase Flows: The objective of this task is to develop stable computational models based on the multiple-relaxation-time lattice Boltzmann method. The computational modeling will assist site engineers with critical issues related to HLW retrieval and processing that involves the analysis of gas-fluid interactions in tank waste.

Task 18 - Technology Development and Instrumentation Evaluation

Subtask 18.1 - Evaluation of FIU's SLIM for Rapid Measurement of HLW Solids on Tank Bottoms: The objective of this task is to determine if FIU's sonar (SLIM) can provide images of tank floors of mixing tanks during, or in between, pulse jet mixing (PJM) cycles. The goal is to provide a tool that can evaluate the ability of the PJMs to keeps the particles in the slurry suspended.

Subtask 18.2 - Development of Inspection Tools for DST Primary Tanks: The objective of this task is to develop an inspection tool that can travel through the air slots of the tank refractory pads and provide visual feedback of the tank bottom. This tool will assist engineers in determining potential problems with the tank floors and identify the source and location of leaks.

Task 19 - Pipeline Integrity and Analysis

Subtask 19.1 - Pipeline Corrosion and Erosion Evaluation: The objective of this task is to analyze thickness measurement data obtained from HLW transfer system components and determine if any appreciable amount of erosion or corrosion has occurred. Trends will be assessed and the estimated remaining useful life will be determined based on the volume of flow transferred or time of service. This task will assist engineers in determining the integrity of the pipeline system and provide a framework for defining the design life of future pipeline systems.

TASK 2.1 FY13 YEAR END TECHNICAL REPORT
Development of Alternative Unplugging Technologies

EXECUTIVE SUMMARY

In previous years, Florida International University (FIU) has tested and evaluated a number of commercially available pipeline unplugging technologies. Based on the lessons learned from the evaluation of the technologies, two alternative approaches have been developed by FIU. These are an asynchronous pulsing system (APS) and a peristaltic crawler. The APS is based on the principle of creating pressure waves in the pipeline filled with water from both ends of the blocked section in order to break the bonds of the blocking material with the pipe wall via forces created by the pressure waves. The waves are created asynchronously in order to shake the blockage as a result of the unsteady forces created by the waves. The peristaltic crawler is a pneumatically operated crawler that propels itself by a sequence of pressurization/depressurization of cavities (inner tubes). The changes in pressure result in the translation of the vessel by peristaltic movements.

For this performance period, additional experiments were conducted to further validate the asynchronous pulsing system's ability to unplug a large-scale pipeline testbed and compare the performance of the APS to the data obtained from the testing conducted on small-scale testbeds.

Three-ft kaolin-plaster plugs were placed within a test pipeline loop constructed with two 135-foot runs on either side of the plug. The pipelines were instrumented with accelerometers and pressure transducers that can capture vibration and pressure data in the pipeline. Various conditions within the pipeline were evaluated, including lines with and without entrained air. Studies were conducted prior to the engineering scale testing to determine how air entrainment can be mitigated. For the engineering scale testing, parametric trials were conducted using an exemplar plug to determine the effects of varying static pressure, amplitude of the pulse pressure and pulse frequency. Research efforts also focused on manufacturing a plug that had the necessary material characteristics and could not be removed with static pressures less than 300 psi. Unplugging trials were conducted based on the results obtained from the parametric testing. Trials included using sine, triangle and saw tooth wave types as well as pulse frequencies of 1, 2 and 3 Hz under a static pressure of 50 psi. A successful unplugging was obtained during each trial. The results obtained during the experimental phase of the project are presented which include pressures and vibration measurements that capture the propagation of the pulses generated by the system.

During this performance period, efforts also focused on the continuation of the engineering-scale testing of the peristaltic crawler system (PCS). Previous tests showed that the front and rear cavities of the crawler presented durability issues. After conducting fatigue tests on the cavities, it was determined that stress risers around the circumference of the clamps caused the cavity material to rupture prematurely. The design was improved to have a 1-in distance between the clamps to provide more available material for expansion.

Manual tether pull tests were conducted to determine the axial load requirements on the unit as the tether length increased and as friction resistance increased with the addition of 90° elbows. In order to reduce the frictional force (axial load), the pipeline was flooded with water. After

flooding the pipeline, the maximum axial force requirement after the second elbow was reduced to approximately 45 lb. Using the information from the tether load tests, the crawler's response to axial loads was evaluated using a pulley-weight system. The largest load recorded was 25 lb with a maximum speed of 6.05 ft/hr. Other improvements included the addition of a ring on the bellow to aid the crawler's navigation through elbows.

Navigational tests revealed durability issues associated with the pneumatic lines and cavities. Premature failure of the cavities were likely caused by stress risers resulting from the axial deflection of the rubber material as the axial load increased. Alternative designs to improve the durability of the cavities continue to be investigated.

INTRODUCTION

As Hanford moves into a more aggressive retrieval and disposal program, site engineers will increase waste transfer activities using their cross-site pipelines. This increased activity comes with a corresponding increase in the probability of pipeline plugging. In the past, some of the pipelines have plugged during waste transfers, resulting in schedule delays and increased costs. Furthermore, pipeline plugging has been cited as one of the major issues that can result in unplanned outages at the Hanford Waste Treatment Plan (WTP), causing inconsistent waste throughput. As such, the availability of a pipeline unplugging tool/technology is crucial to ensure smooth operation of the waste transfers and to ensure Hanford tank farm cleanup milestones are met. Current commercially available pipeline unplugging technologies do not provide a safe, cost-effective and reliable means to address the current problems [1]. The Applied Research Center (ARC) at FIU has evaluated the lessons learned from previous technology testing, and has developed two pipeline unplugging concepts that can be added to the site's "toolbox" [2]. The concepts that FIU has developed will address various plug scenarios with improved deployability and performance. One of the concepts developed is called the asynchronous pulsing system (APS). This document presents a summary of the technology development as well as the results from the experimental testing for APS performed at FIU. Experimental testing included parametric and unplugging tests using a testbed that has 135 ft of pipe on each side of a plug.

In addition, this report presents the design improvements and experimental testing results of the peristaltic crawler system (PCS). It provides the experimental results that show the necessary requirements that will enable the PCS to conduct unplugging and inspection operations in a 430-ft pipeline. The general configuration of the system remained similar to that of the unit tested previously, but changes were implemented to improve the crawler's navigational speed and also to equip the system with a camera for inspection capability. Additionally, a 430-ft engineering testbed was designed and assembled and the system was placed in a compact platform for easy deployment. Preliminary navigational tests in the engineering scale testbed were conducted and a number of issues associated with operating the system in longer pipelines were found. Proposed solutions to the issues are presented and conclusions and recommendations for further improvement of the system are provided.

EXPERIMENTAL TESTING OF THE ASYNCHRONOCUS PULSING SYSTEM

Background

In order to clear plugged radioactive waste transfer lines, non-invasive techniques can have significant advantages since problems such as contamination clean-up and exposure to radioactive waste of invasive devices can be avoided. During previous work, FIU evaluated two technologies that fall into this category, namely, NuVision's wave erosion method and AIMM Technologies' Hydrokinetics method. These technologies fill the plugged pipeline with water up to an operating pressure level and induce a pressure variation at the inlet of the pipeline to dislodge the plug. Using the experience obtained during experimental evaluations of both technologies, FIU has developed a non-invasive unplugging technology called the asynchronous pulsing system (APS) that combines the attributes of previously tested technologies. The APS is based on the idea of creating pressure waves in the pipeline filled with water from both ends of the blocked section in order to dislodge the blocking material via forces created by the pressure waves. The waves are generated asynchronously in order to break the mechanical bonds between the blockage and the pipe walls as a result of the vibration caused by the unsteady forces created by the waves. A pipeline unplugging technology using similar principles for generating pressure pulses in pipelines has previously been tested at the Idaho National Laboratory (INL) by Zollinger and Carney [2]. The most relevant difference in the current technology from the unplugging method developed at INL is that both sides of the pipeline are used to create the asynchronous pulsing in the current technology. Figure 1 shows a sketch of how this technology can be utilized for a typical plugging scenario. During last year's work, the asynchronous pulsing system's ability to unplug an engineering scale pipeline testbed was validated. This year's work involved conducting a larger engineering scale test matrix. Testing included conducting parameteric tests to determine the optimal operating parameters as well as applying these parameters to unplug the pipeline. The experiments consisted of placement of a 3-ft. kaolin-plaster plug between two 135-foot pipeline sections.

The experiments consisted of placement of 3-ft kaolin-plaster plugs within a test pipeline loop and using the system to unplug the pipeline.

Figure 1. Pipeline unplugging scenario in a horizontal pipe.

General Description

The asynchronous pulsing method is based on the idea of creating asynchronous pressure waves in a blocked section of a pipeline filled with water in order to dislodge the blockage by the forces created by the pressure waves. The waves break the mechanical bonds between the blockage and the pipe walls as a result of the vibration caused by the unsteady forces that are created by the waves. Figure 2 illustrates the basic principle and components of the technology.

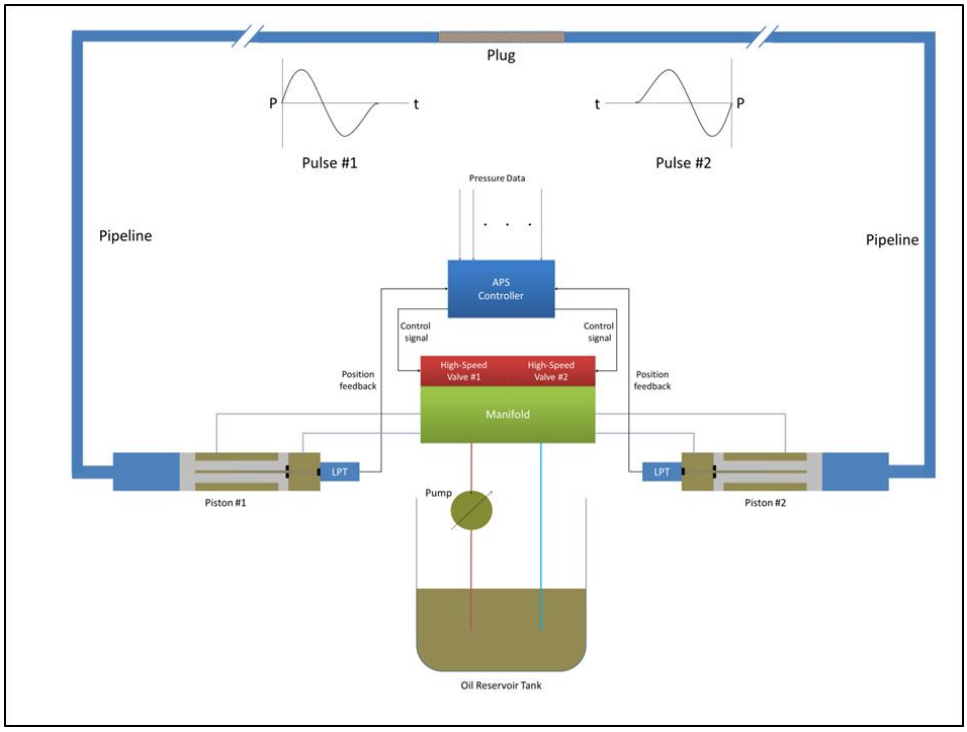

Figure 2. Principles of asynchronous pulsing method with major components labeled.

The pressure waves are created by a pair of hydraulically operated piston water pumps that are attached to both ends of the pipeline. The hydraulic oil that drives the pumps is provided by a hydraulic unit that is powered by a 10 HP/240-volt 3-phase electric motor which drives a hydraulic oil pump to generate oil pressure. The hydraulic unit is equipped with an oil pressure regulator to control the pressure of the oil leaving the unit between 100 to 2000 psi. A pair of rapid acting proportional valves control the direction and quantity of oil entering each of the water pumps. This controls the position, direction of movement and speed of each water pump's piston. By varying the hydraulic oil pressure along with the opening speed of the proportioning valves, each water pump is used to create a pressure pulse into the pipeline.

TESTING AND RESULTS - ASYNCHRONOCUS PULSING SYSTEM

Engineering Scale Testbed

Figure 3 shows the piping and instrumentation diagram of the engineering scale loop which consists of two 135-foot runs on either side of a plug. The elevations of the pipeline supports were surveyed and adjusted to provide a pipeline slope of 0.14 degrees. As can be seen in Figure 4, the hydraulic power unit was placed inside a shed to protect it from the rain.

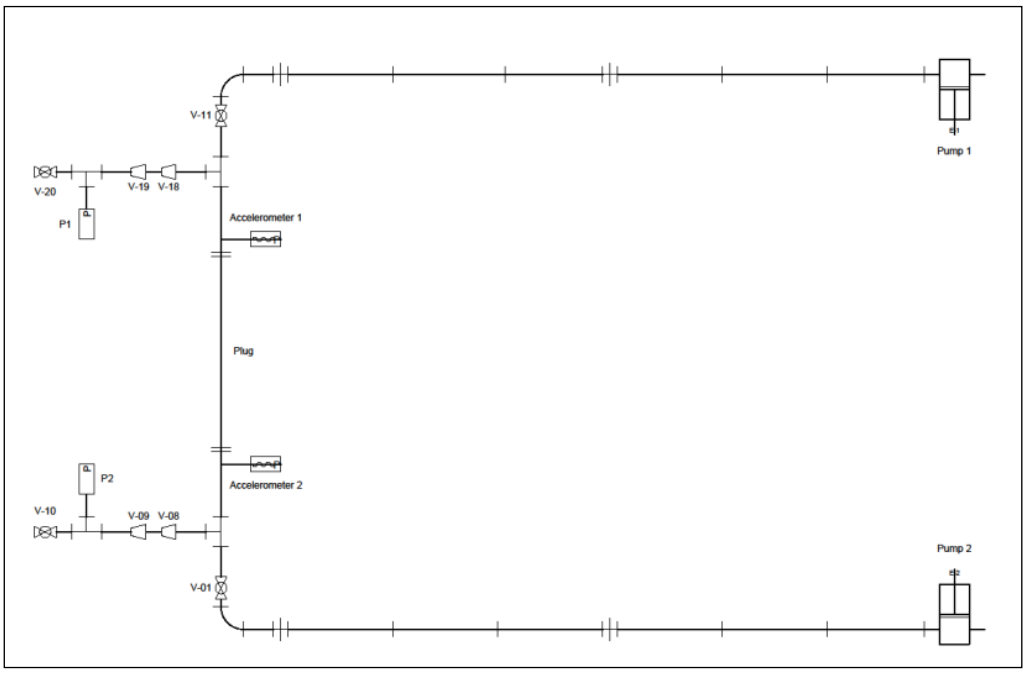

Figure 3. Engineering scale asynchronous pulsing test loop piping and instrumentation diagram.

Figure 4. Engineering scale testbed images for asynchronous pulsing system.

Parametric Tests

Parametric tests were conducted in order to determine the optimal operating parameters for pipeline unplugging. For these tests a simulated plug made from solid piece of aluminum was used instead of a simulant plug to allow for multiple tests to be conducted without the need for plug replacement. Tests were conducted at a static pressure of 50 psi while varying the operating parameters. The parameters included the pulse wave type, pulse amplitude and pulse frequency. The pulse wave types included saw tooth, triangle, square and sine waves. Each wave type was used to run tests at all the parameters shown in Table 1.

Table 1. Parametric Test Parameters

Pulse Amplitude (PSI)	Pulse Frequency (Hz)							
10	0.5	1.0	1.5	2.0	2.5	3.0	3.5	4.0
25	0.5	1.0	1.5	2.0	2.5	3.0	3.5	4.0
50	0.5	1.0	1.5	2.0	2.5	3.0	3.5	4.0
100	0.5	1.0	1.5	2.0	2.5	3.0	3.5	4.0

The pulse amplitude is the pressure setting that the controller attempts to achieve inside the pipeline. However, because of response delays in the control valves, this pressure is overshot. Due to the overshooting of the pressure pulse, the center of the pressure pulse wave also shifts to a higher amplitude. After analyzing the results of the parametric tests, it became apparent that the highest differential pressure applied to the plug section would occur when the controller is set to the highest amplitude along with the lowest frequency. The highest differential pressure of 265 psi occurred at an amplitude of 100 psi and a frequency of 0.5 Hz; however, at that frequency, the pump pistons travel reach their design limit. This is evident in Figure 5 by the flat peaks in the pressure pulse diagram where P3 and P4 are the pressure measurements on either side of the plug. Therefore, the lowest frequency used for the testing is 1.0 Hz. Figure 6 and Figure 7 show how the pulse amplitude is reduced as the frequency increases. In addition, as can be seen in Figure 8, as the frequency increased beyond 3.5 Hz, the pressure pulses deviated from each other. As in previous testing, pressure transducer failures were encountered. After consulting with and sending transducers back to the manufacturer for analysis, the failures were found to be due to over pressurization. The over pressurization was caused by expected pressure amplification as a result of the water hammer affect in the pipeline. Larger capacity transducers were installed and no other failures occurred.

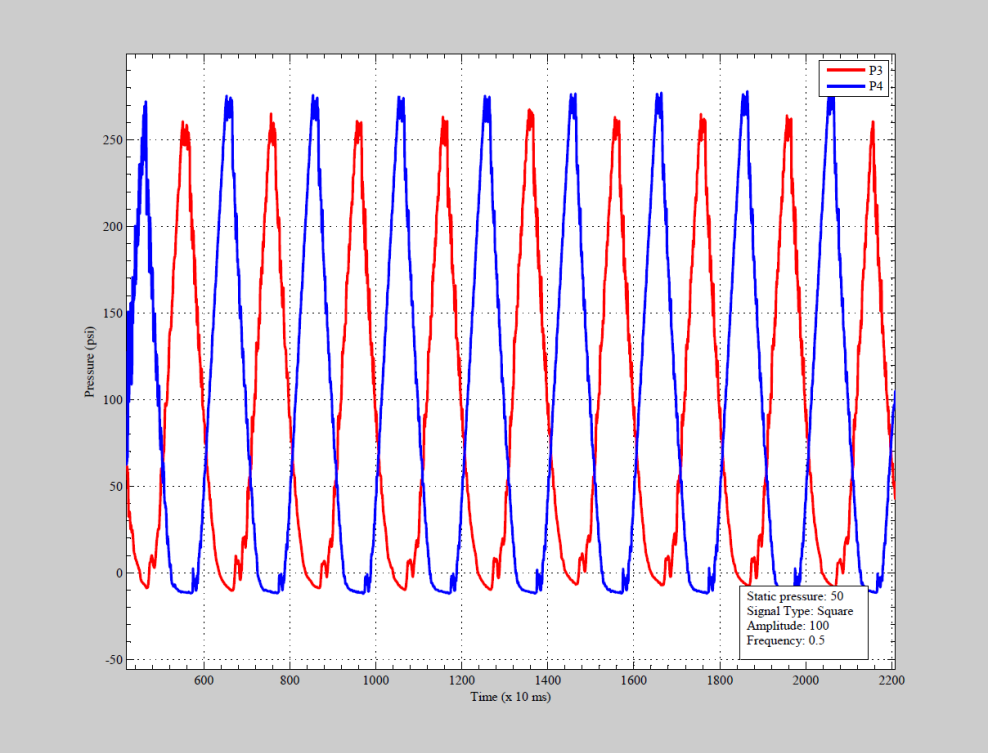

Figure 5. 100 psi amplitude with a 0.5 Hz pulse frequency.

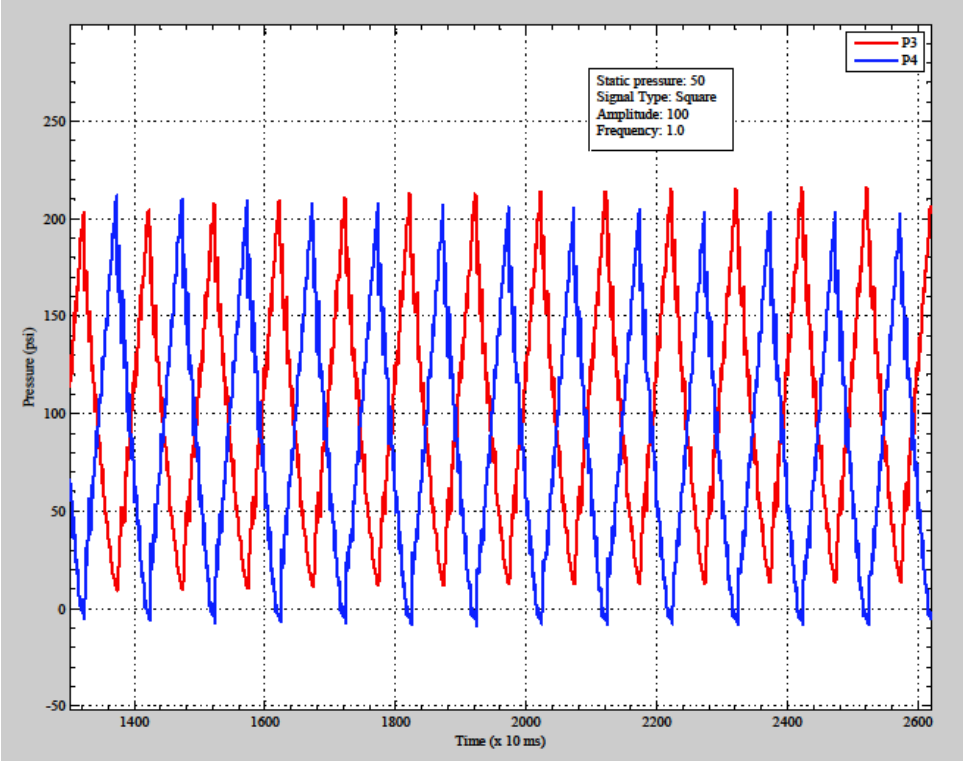

Figure 6. 100 psi amplitude with a 1.0 Hz pulse frequency.

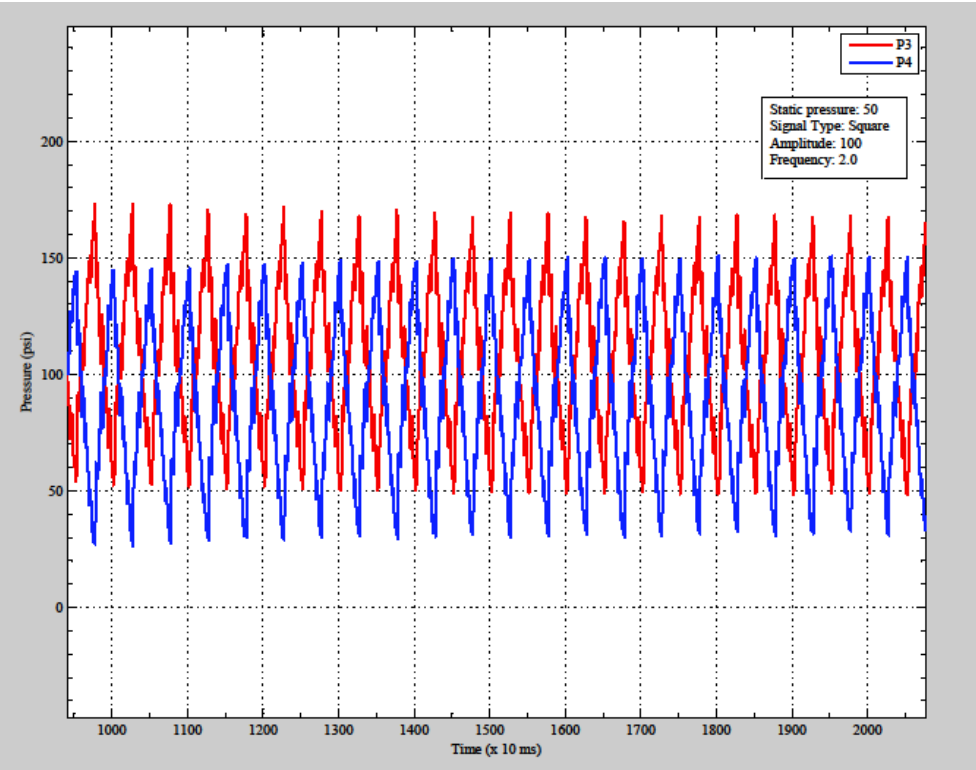

Figure 7. 100 psi amplitude with a 2.0 Hz pulse frequency.

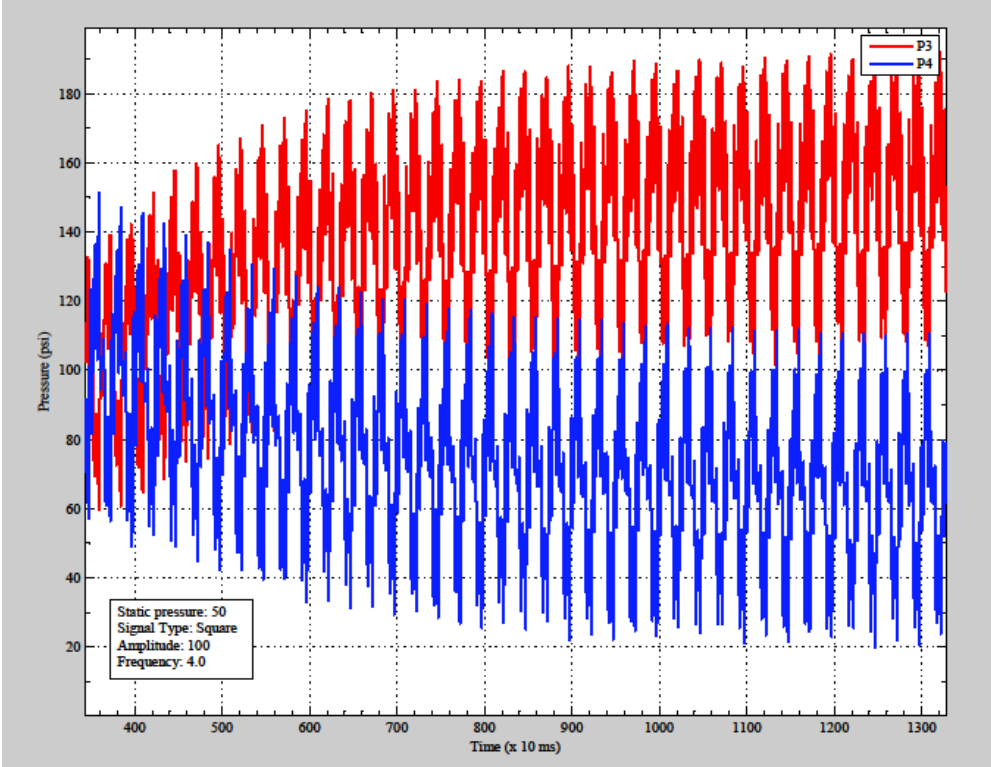

Figure 8. 100 psi amplitude with a 4.0 Hz pulse frequency.

Plug Development and Characterization

The primary objective behind the plug development is the development of a high shear strength 3-ft. plug that could withstand a maximum static pressure of 300 psi. In previous unplugging studies, several plugs made from k-mag, kaolin-bentonite, sodium-aluminum-silicate, etc. were tested. The kaolin-plaster plug of various compositions was reviewed that mimicked the physical behavior of actual waste. [3] For the current tests, a kaolin and plaster of Paris mixture was used to fabricate the plug material. Recipes and procedures were developed with input from Hanford site engineers. The optimal plug strength was obtained when the kaolin and plaster of Paris were mixed together with water at a weight-percent ratio of 35% kaolin, 35% plaster of Paris and 30% water. The plug was also easier to manufacture and had a texture which made it easier to fill the pipe before the initiation of the curing process. During the curing process, the plugs were wrapped in wet cloths and allowed to cure for at least 24 hours so that optimal strength was achieved. Since the plugs are exposed to water at pressure in the asynchronous pulsing system while preparing the unplugging test on the pipeline, it was necessary to ensure that the plug did not weaken before the testing began. As can be seen in Figure 9, experiments were conducted on saturated plugs by saturating the plugs at 50 psi for one hour, at 100 psi for one hour and 200 psi for another hour before performing a blowout test to determine if there is a reduction in the blowout strength. No reduction in strength was observed; blowout pressures were between 250 to 300 psi.

Figure 9. Plug blowout test.

Unplugging Tests

After analyzing the results of the parametric testing, FIU chose the parameters that produced the greatest pressure differential change across the plug. A test matrix was developed that included

triangle, square and sine wave types. The saw tooth wave type was omitted due to its tendency to allow the pulse waves to deviate. In order to avoid the problems of piston over travel and pulse deviation, pulse frequencies that are too low or too high were omitted from the unplugging tests. Pulse frequencies of 1 Hz, 2 Hz and 3 Hz were utilized for the unplugging tests. Table 2 shows the test parameters utilized for the unplugging tests. All tests were conducted at 100 psi pulse amplitude setting with a 50 psi static pressure. A 50 psi static pressure was used because this is the fairly constant supply pressure from the building's plumbing supply; it allowed for a consistent starting static pressure that was not affected by the temperature of the pipeline.

Table 2. Unplugging Test Parameters

Pulse Wave Type	Pulse Frequency (Hz)		
Triangle	1.0	2.0	3.0
Square	1.0	2.0	3.0
Sine	1.0	2.0	3.0

Just as in the parametric tests, the results of the unplugging tests presented in Table 3 show that as the pulse frequency increased, the pressure amplitude decreased. In addition, it was observed that the pulse wave type had an effect on the pressure amplitude. The triangle waves had the greatest average pressure amplitude and was followed by the sine wave and finally by the square wave with the smallest amplitude. In addition, the time required to dislodge the plug (cycling time) was measured. Both the shortest and longest cycling times occurred during triangle wave tests. The shortest time of 23 minutes was achieved at 2 hz, while the longest cycling time of 88 minutes was achieved at 3 hz.

Table 3. Unplugging Test Results

Pulse Wave Type	Pulse Frequency (Hz)	Unplugged (Y/N)	Average Pressure Amplitude (PSI)	Cycle Count	Cycling Time (min)
Triangle	1.0	Yes	192.5	1973	33
Triangle	2.0	Yes	96.5	2805	23
Triangle	3.0	Yes	92.5	15818	88
Square	1.0	Yes	162.5	2708	45
Square	2.0	Yes	123.5	4344	36
Square	3.0	Yes	97	9892	55
Sine	1.0	Yes	180.5	1816	30
Sine	2.0	Yes	106	5113	43
Sine	3.0	Yes	82.5	8162	45

Examples of a few of the test trials are shown in the following figures. Figure 10 shows the pressure pulse profile during a successful unplugging using a 1 Hz square wave, where P3 and P4 are the pressure reading on either side of the plug. As can be seen in the graph, the pulse peaks become flat when the plug becomes dislodged. Figure 11 shows the pressure profile for a successful unplugging trial using a 2 Hz triangle wave.

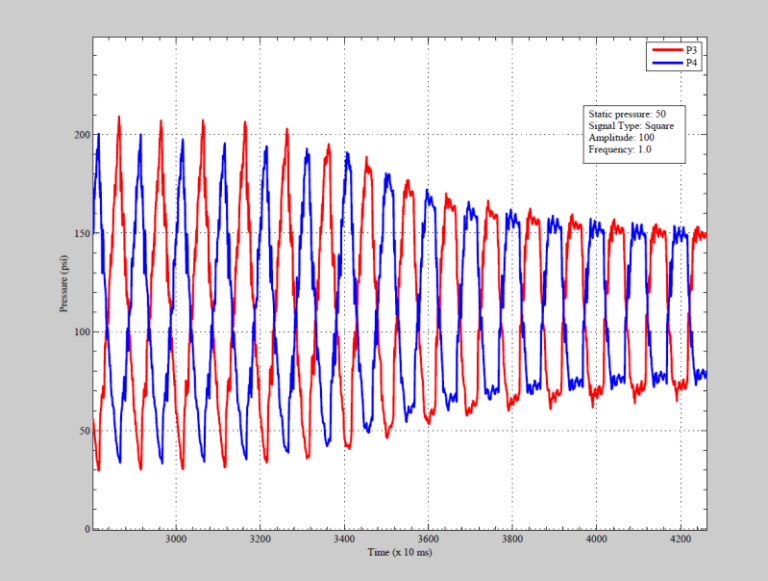

Figure 10. Pressure pulses during an unplugging at 1 Hz square wave.

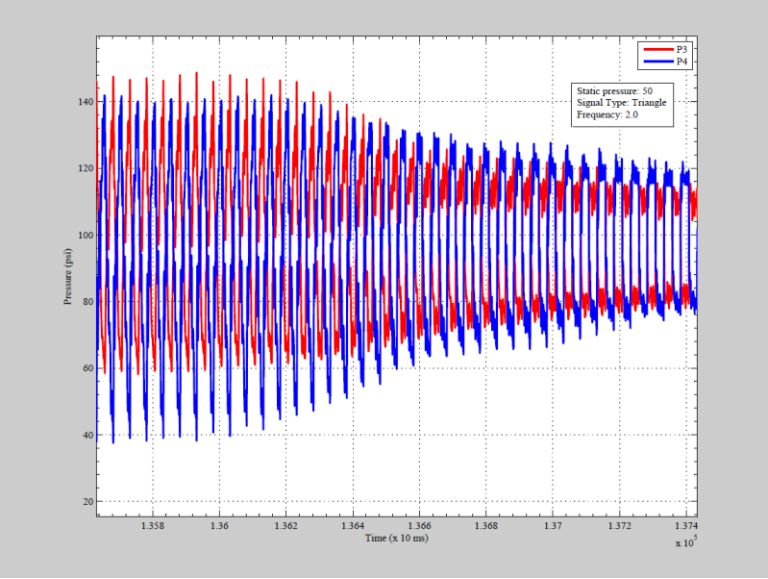

Figure 11. Pressure pulses during an unplugging at 2 Hz triangle wave.

For these tests, the pipeline was considered unplugged when the plug was dislodged and shifted inside the pipeline. Figure 12 shows a kaolin-plaster plug after unplugging. As can be seen by the pictures, the plug has been dislodged and shifted approximately ½-inch inside the pipeline.

Figure 12. Kaolin-plaster plug after unplugging.

ENGINEERING SCALE PIPELINE UNPLUGGING TESTING USING THE PERSITALTIC CRAWLER SYSTEM

Background

Past and current research efforts at FIU include the evaluation of commercially available technologies and the development of novel technologies for remediating pipeline unplugging incidents on HLW lines [4]. Part of this research includes the development of the PCS [5]. The PCS consists of a pneumatic/hydraulic powered unit which propels itself by a sequence of pressurization and depressurization of cavities constructed on a flexible assembly. The objective is to bring an unplugging tool in close proximity to a plug by navigating through 500 ft of pipeline from the inlet point. The flexible body of the unit allows the system to navigate through straight sections and 90° elbows and was sized to operate inside 3-in pipelines. The unit also has a camera so that it can be utilized as an inspection tool as well [6].

The PCS has evolved through three design iterations (generations), each having progressive improvements using lessons learned from each previous design. Results from the experimental testing of each generation were utilized to improve the system's performance and durability to withstand the rigors of performing pipeline unplugging and inspection operations.

The goal of the first generation PCS was to validate the principles demonstrated in the computational models. It also served to establish design and manufacturing procedures required to fabricate and assemble the PCS. The crawler unit was manufactured and assembled using rubber bellows and aluminum rims. All parts of the crawler unit were assembled together using simple clamps. The sequence of pressurization of the cavities was controlled manually. The system proved to work effectively in navigating in a straight pipeline section and also in pipeline sections coupled to a 90º elbow. The unplugging mechanism showed promise in performing unplugging operations but the structural integrity of the unit did not allow for complete successful unplugging operations.

Based on issues related to performance and durability observed with the first generation peristaltic crawler, a second generation unit was designed and fabricated. The materials and design were improved to ensure that the unit could function in a HLW environment. The bellow material was changed from reinforced rubber to hydroformed stainless steel. This allowed achieving higher pressures inside the bellows without rupture of the walls and in turn, increasing the pulling force capability of the crawler. Also, the attachments of the flanges to the bellows were changed so that they were securely attached using bolts and a high temperature gasket. Moreover, the flexible membranes forming the front and back cavity were changed to a flexible PVC material and secured to the flanges using high compression clamps to prevent any leaks at those locations.

The improvements on the third generation crawler included reducing the crawler outside diameter to improve the crawler's navigational ability, implementing an edge-welded inner bellow to reduce the compression time requirements, positioning the pneumatic valves in close proximity to the crawler to make the tether length independent of cycle time, and implementing on-board electronics for visual feedback of the conditions inside the pipeline.

System Description

The PCS consists of a crawler unit, a tether-reel assembly and a control station. As noted previously, the motion of the crawler is powered by pressurizing air into flexible cavities. Figure 13 shows the basic schematics of the pneumatic system used to propel the crawler. Pressurized air is provided from an air reservoir and is regulated down to the desired maximum pressure of the system (REG 4). The pressure is then directed to the manifold consisting of 3 valves controlled via a programmable logic controller (PLC). Additionally, vacuum pressure is provided to the manifold. The position of each of the valves determines whether positive pressure or vacuum pressure is provided to each of the lines that power the cavities of the crawler (C_LINE 1, C_LINE 2, C_LINE 3). The sequence in which the valves are activated/deactivated dictates the forward or backward motion of the crawler in the pipeline [7].

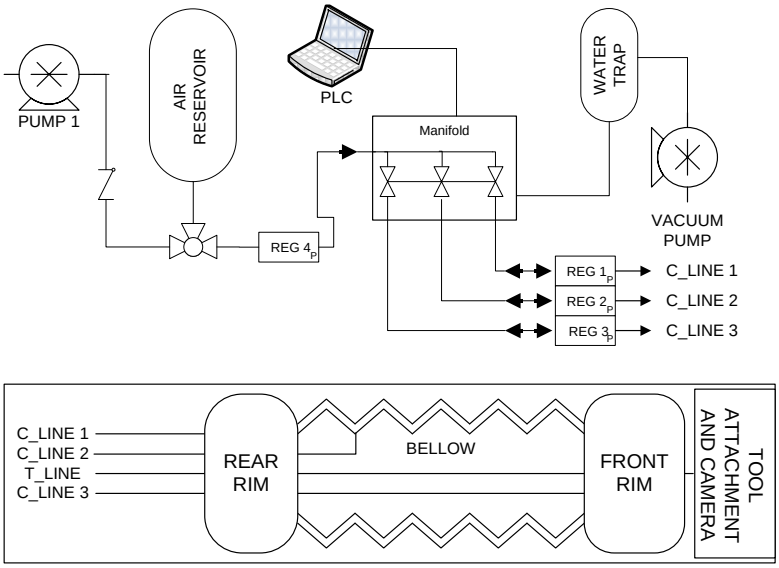

Figure 13. Schematics of pneumatic systems of PCS.

The unplugging tool is designed to be attached to the front of the unit and powered by pressurized water. The tether being pulled by the crawler unit includes the hydraulic line (T_Line). The video feedback system was also designed to be attached to the front of the unit. Figure 14 shows the basic schematics of the hydraulic system used to conduct the unplugging operations and the video feedback system.

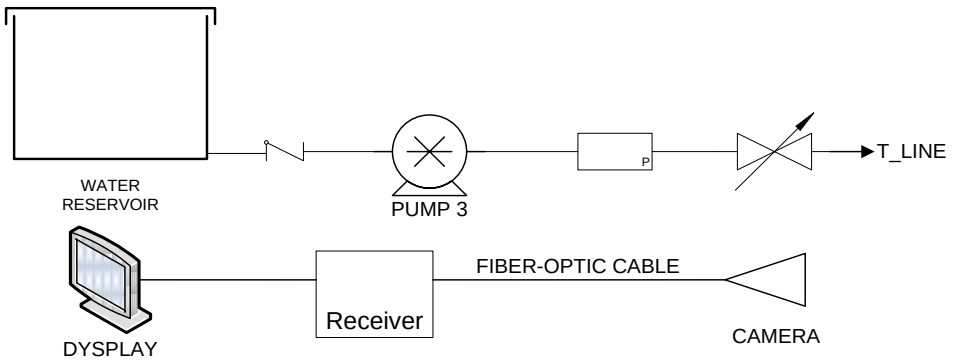

Figure 14. Schematics of hydraulic system to power unplugging attachment and video feedback system.

The crawler unit consists of a double walled bellow assembly and a front and back rim to which flexible sleeves are clamped forming the front and back cavities. The double walled bellow assembly creates a passage that allow particles of the plug that are set loose during the unplugging process to travel to the back of the unit. Attached to the front rim is a nose cap designed to hold the unplugging tools (high pressure water nozzle) and the camera. Figure 15 shows a rendering of the crawler unit and an exploded view of the assembly [6].

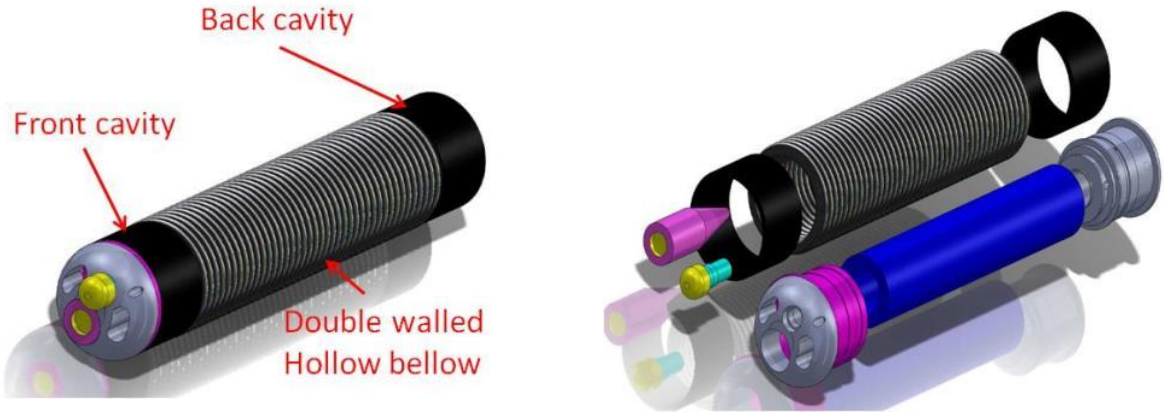

Figure 15. Rendering of crawler (left), exploded view of crawler assembly (right).

The tether-reel assembly connects the crawler to the control station and the power supply source. The tether consists of three pneumatic lines, one hydraulic line, and one multi-conductor cable jacketed together having a total length of 500 ft. The reel system was designed to accommodate the tether and provides rotating connections to the pneumatic, hydraulic, and electrical lines. The reel is electrically controlled using its 120 V motor. Figure 16 shows the tether connected to the crawler and the reel system with the tether wound on it [6].

Figure 16. Tether attached to the crawler unit (left), tether-reel assembly (right).

The control station includes the pneumatic pressure regulators, a vacuum pump, vacuum chamber and a controller box containing the PLC that controls the position (opened/closed) of the pneumatic valves. By programming an appropriate sequence on the PLC, the desired motion is achieved. The control station also has a monitor connected via a fiber optic cable to the on-board camera that provides real-time images of the conditions inside the pipeline. Figure 17 shows the control station with the pneumatic and control box and the display system connected to the camera.

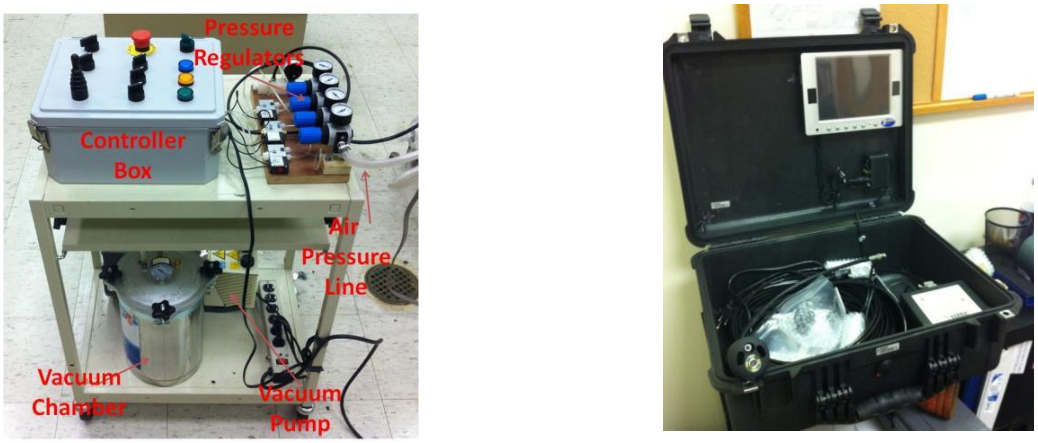

Figure 17. Control station (left), display monitor (right).

Engineering-Scale Testbed

To evaluate the performance of the PCS on longer pipelines, the previously assembled engineering scale testbed was used. The testbed consists of 24 straight sections and three 90° elbows assembled with couplings. The pipes sections used are schedule 10 carbon steel pipes and have an inner diameter of 3.26 inches. The total length of the pipeline was adjusted based on the length of tether available. The final configuration was reduced from 500 ft to 430 ft to account for losses in tether length resulting from jacketing the pneumatic, hydraulic and electric lines together. The control station, air compressor, vacuum pump, tether-reel assembly, and feed-back camera monitor were placed in a container for easy deployment. Figure 18 shows the testbed layout and system configuration.

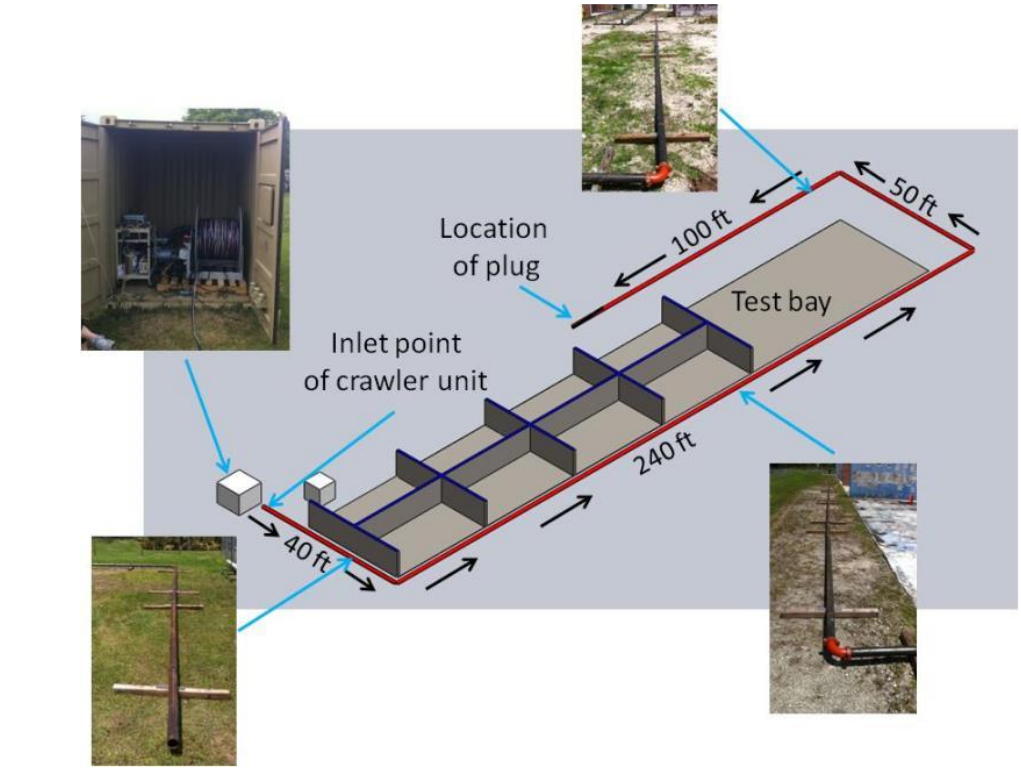

Figure 18. Engineering scale testbed configuration.

Tether Pull Force Tests

Using the engineering scale testbed, tests were conducted to determine the pulling force required to drag the tether through the pipeline. The tests consisted on manually pulling the tether and recording the pulling force using a spring scale device. The force recorded when pulling the tether on a 21-ft straight pipe section was 18 lb. The force required to pull the tether increased significantly once the tether was routed through a straight pipe coupled to a 90° elbow. This large force requirement would hinder the crawler unit from successfully navigating longer distances. In order to decrease the friction force and also reducing the contact area between the tether and the pipeline, a 0.051 in stainless steel wire was coiled onto the tether (shown in Figure 19). Pull force tests conducted using this configuration showed that the force required to pull the tether using a 21-ft section was reduced to 13 lb. The force required to pull the tether inside a pipeline of 188 ft in length having a 90° elbow located 42 ft from the inlet point was approximately 43 lb. Figure 20 shows the results for the manual pulling force tests conducted.

Figure 19. Tether with stainless steel coil.

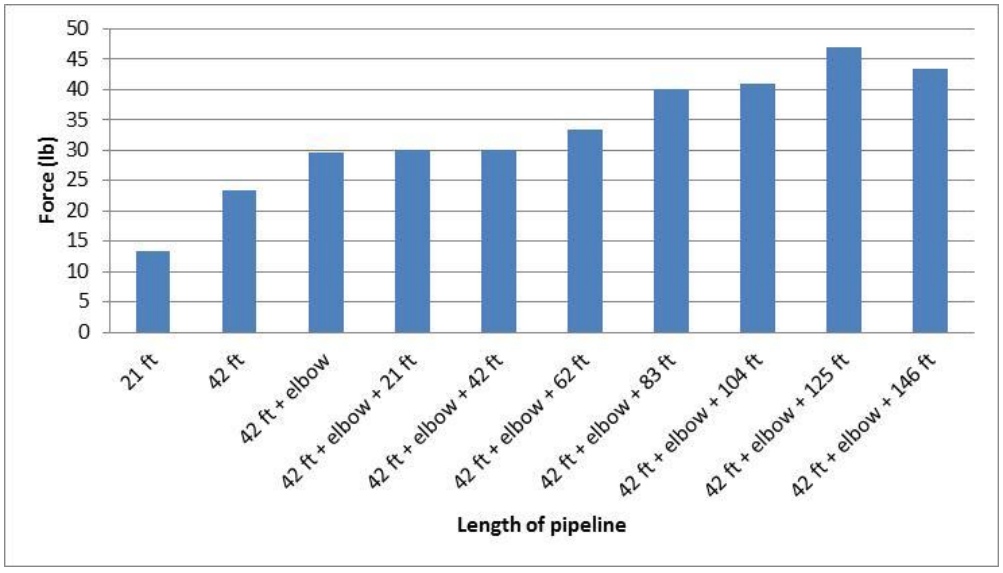

Figure 20. Manual tether pulling force for different pipeline lengths.

Additional manual pulling tests showed that the force required to drag the tether through the 2nd elbow required a force of over 100 lb. This large force requirement would prevent the crawler from navigating through the 2nd elbow. In order to reduce the friction coefficient between the tether and the inner pipe walls, thus reducing the pulling force requirements, the pipeline was

flooded with water. After flooding the pipeline, the maximum pulling force requirement after the second elbow was reduced to approximately 45 lb.

Crawler Navigational/Load Tests

To evaluate the crawler response to different tether loads, a pulley-weight system was utilized. A steel cable was attached to the front of the unit, and weights were attached to the end of the cable. Figure 21 shows the test set-up used.

Figure 21. Testbed, pulley and weights set-up.

Tests were conducted for 5, 10, 15, 20 and 25 lb of resistance. The largest load recorded was 25 lb with a maximum speed of 6.05 ft/hr. Table 4 shows the experimental results from the tether pull force tests.

Table 4. Crawler Navigational Speed and Pulling Load

			1st Trial			2nd Trial			3rd Trial			
Pounds	Bellow Pressure (psi)	Rim Pressure (psi)	Time (min.sec)	Inches	Speed (ft/hr)	Time (min.sec)	Inches	Speed (ft/hr)	Time (min.sec)	Inches	Speed (ft/hr)	Average
0	20	80	5.06	10.50	10.38	5.03	11.81	11.74	4.50	11.63	12.92	11.68
5	20	80	5.16	9.75	9.45	5.20	11.38	10.94	5.21	11.44	10.98	10.45
10	20	80	4.17	7.50	8.99	4.31	9.38	10.88	4.36	9.25	10.61	10.16
15	20	80	6.10	10.69	8.76	6.25	11.25	9.00	6.41	12.06	9.41	9.06
20	20	80	7.28	13.13	9.01	6.19	11.38	9.19	7.13	10.50	7.36	8.52
25	20	80	7.44	9.00	6.05							

A similar testing procedure was used to evaluate the response of the system when turning through an elbow carrying an axial load. Initial tests showed that the crawler was not able to negotiate under these loading conditions. Several design improvements were evaluated to address this issue.

The first approach was to place a compression spring nested into a washer at the rear of the unit to promote compression of the bellow. The washer was designed to fix the spring in place while leaving sufficient area for the lines. Figure 22 shows the washer manufactured using rapid prototyping, and the washer-spring system assembled to the crawler. Preliminary tests showed that the compression spring improves the crawler's speed on straight section but it does not aid turning through an elbow.

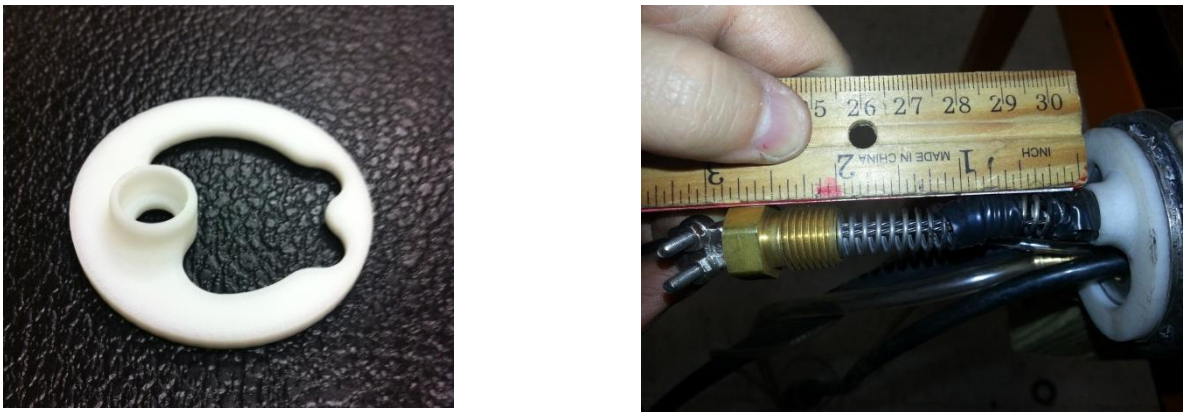

Figure 22. Rear washer and rear washer assembled to the crawler.

The second approach to promote turning of the rear rim through an elbow was to place a rear assembly with rollers to prevent the rear edge of the crawler from wedging against the pipeline wall. Figure 23 shows a rendering of the roller and the prototype mounted to the rear of the crawler. Tests indicated no improvement in navigation using this assembly.

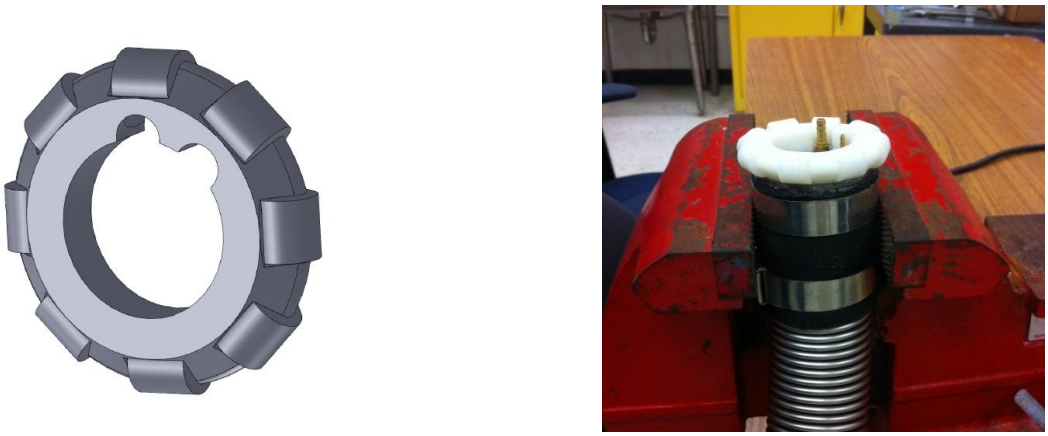

Figure 23. Rendering of rear roller, and rear roller prototype assembled to the crawler.

After analyzing the geometry changes of the bellow when navigating inside an elbow, the centerline of the bellow should stay close to that of the elbow in order for the crawler to clear the elbow. A new approach using a ring nested in one of the convolutions of the bellow and protruding 0.25 in from the bellow's diameter causes the elbow and bellow centerlines to remain in close proximity throughout the turn of the crawler. Figure 24 shows the ring manufactured using a rapid prototyping printer and the ring assembled on the crawler 2 in from the rear rim.

Figure 24. Ring prototyped, ring assembled on the crawler.

Tests conducted with the ring assembled on the crawler allowed the unit to clear the elbow with and without an axial pulling load. The time recorded for the crawler to clear the elbow was 4 minutes with no load and 8 minutes with a 15 lb axial load.

Navigational Tests

After the changes to the crawler were implemented, navigational tests using the engineering-scale testbed were conducted. Prior to introducing the crawler at the inlet point (Figure 25 a), the pipeline was flooded and the ends were elevated to keep the water inside the pipeline. The crawler navigated 41 ft before reaching the first elbow in 2 hours and 17 minutes (a speed of approximately 24 ft/hr). The time recorded to clear the first elbow was 16 min. After clearing the elbow, the crawler stopped navigating and the test was halted.

a)  b) 

Figure 25. a) DOE fellow introducing crawler in the pipeline, b) issues encountered after clearing first elbow.

It was determined that the cyclic pressurization and depressurization of the pneumatic lines inside the trailing capsule caused the lines to burst (shown in Figure 26 a). To resolve this issue, the lines were replaced with abrasion resistance clear polyurethane tubing having a wall thickness of 1/32 in. Navigational test were continued from the crawler's last position in the pipeline. After reaching a maximum distance of 60 ft from the inlet point, the front cavity ruptured (Figure 26 b). Several attempts of replacing the cavity and restarting the test were conducted. It was concluded that the axial force required to drag the tether caused a deflection on the cavities increasing the stress riser at the clamp locations.

a)  b) 

Figure 26. a) Failure of the pneumatic lines, b) largest distance achieved after fist elbow.

CONCLUSIONS AND FUTURE WORK

Two technologies, APS and a peristaltic crawler, have continued to be developed and evaluated during FIU Year 4 (FY13).

After analyzing the data of the APS on a large scale loop, several observations were made. As in the previous testing done on smaller loops, air in the system has a major effect on the system's performance. As with the smaller loops, entrained air can be mitigated by either applying a vacuum to the pipeline or increasing the system's static pressure. The data obtained from this testing indicates that increasing the static pressure is a more effective method. Figure 27 shows how increasing the static pressure will mitigate the effects of air in the system. During both pulses, there was 8.835 in^3 of air in the pipeline. At atmospheric static pressure, only a 75 psi pulse amplitude is achieved. However, when the static pressure is increased to 75 psi, the pulse amplitude increases to 375 psi.

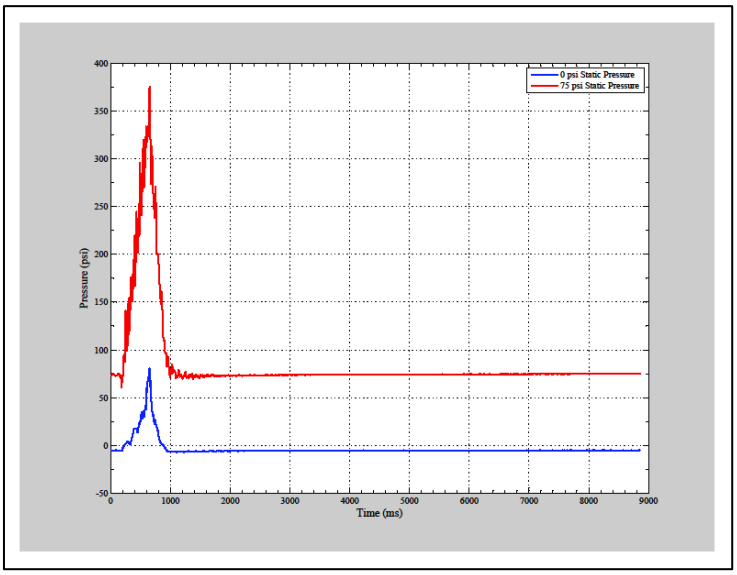

Figure 27. Single Pulse Test at 0 psi and 75 psi with 8.835 in3 of air in pipeline.

During the next phase of testing, experiments will be conducted on the engineering scale loop to determine the maximum percentage of air in the pipeline where the APS can operate effectively.

The tests conducted using the engineering-scale testbed provided information on potential issues that the system will have to endure on longer pipelines. Future efforts will include replacing the pipelines of the engineering scale testbed with schedule 40 pipelines. This change will provide a smaller pipe inside diameter (from 3.26 to 3.07 inches) thus, significantly reducing the expansion requirements of the cavities. Additionally, a testbed with this inner pipe diameter will provide dimensions similar to those found at DOE transfer sites.

Prior to testing the crawler in the 460-ft pipeline, tests will be conducted in a 60-ft pipeline consisting of three straight sections coupled with two 90° elbows. Using this configuration, several navigational tests will be conducted to evaluate the durability of the cavities and pneumatic systems when subjected to an increasing tether pulling force requirement. Additionally, pipeline unplugging operations will be conducted to evaluate the video feedback system in a flooded murky environment.

REFERENCES

1. Roelant, D., (2012). FY2012 Year End Technical Report. Chemical Process Alternatives for Radioactive Waste. U.S. Department of Energy, Office of Environmental Management.
2. Zollinger, W., & Carney, F. (2004). Pipeline blockage unplugging and locating equipment. Conference on Robotics and Remote Systems- Proceedings, (pp. 80 - 85). Gainesville.
3. Pribanic, T., Awwad, A., Varona, J., McDaniel, D., Gokaltun, S., Crespo, J. (2013). Design Optimization of Innovative High-Level Waste Pipeline Unplugging Technologies. In Proceedings of Waste Management Symposia, Phoenix AZ.
4. Committee on Long-Term Research Needs for Radioactive High-Level Waste at Department of Energy Sites, Board on Radioactive Waste Management, National Research Council, (2001), "Research Needs for High-Level Waste Stored in Tanks and Bins at the U.S. Department of Energy Sites: Environmental Management Science Program". National Academy Press Washington D.C.
5. Gokaltun, S., Pribanic T., Varona, J., McDaniel, D., Awwad, A., Roelant, D. (2010). Evaluation and Development of Innovative High-Level Waste Pipeline Unplugging Technologies. In Proceedings of Waste Management Symposia, Phoenix AZ.
6. D. Roelant et al., "Chemical Process Alternatives for Radioactive Waste, FY09 Year End Technical Report, 2010.
7. D. Roelant et al., "Chemical Process Alternatives for Radioactive Waste, FY10 Year End Technical Report, 2011.

TASK 2.2 FY13 YEAR END TECHNICAL REPORT Computational Simulation and Evolution of HLW Pipeline Plugs

EXECUTIVE SUMMARY

At Hanford, an extensive network of pipelines traversing several miles is used to transfer the high level radioactive nuclear waste from tanks to the treatment facilities. During transfer operations, however, the potential for solids to settle along the pipeline frequently exists resulting in partial or sometime full plugging of the pipelines. Pipeline plug formation is caused by changes in the chemistry and flow patterns within the pipe transfer system at Hanford. A better understating of the interactions between the chemical species leading to precipitate formation is required to reduce the risk of pipe plugging. A need exists for a computational tool that can predict plug formation by considering the chemistry dynamics coupled with fluid particle interactions. The use of CFD software has been explored in the past to predict plug formation [1, 2]. The plugging mechanism simulated was settling of solids. Even though the efforts were promising, the models lacked incorporation of chemical reaction kinetics. Hence, a new task was initiated as part of Florida International University's (FIU's) research efforts to develop a multi-physics model using computational fluid dynamics (CFD) software that could simulate the coupled flow and chemistry kinetics and aid in understanding the plug formation process.

The simulation of the plug formation process required solving the coupled equations of flow and transport. Three interfaces were used to facilitate this: 1) flow interface, 2) chemical reaction interface and 3) mixture interface. The flow interface was used to simulate flow fields along the pipe length. The transport of chemical reactions interface was used to model multicomponent transport and evolution of chemical reaction between multiple species ($A+B \rightarrow C$). The mixture interface was used to investigate multiphase interactions and solids growth in a pipeline was modeled.

During this reporting period, several virtual scenarios representing multi-phase flow conditions in a pipe were simulated to study the settling dynamics in a pipeline. The CFD software used to facilitate the model development and analysis was Comsol Multiphysics. A parametric analysis was carried out, simulating settling of solids as a function of flow velocity, particle size, solids density and volume fraction of solids. The results were validated by experimental results and critical velocity correlations. The modeling efforts within the multi-phase domain were also directed towards the simulation of precipitation kinetics such as solids growth in the plug formation process. A conceptual model was proposed and efforts are underway to investigate the ability of Comsol to model the precipitation events.

Future work will include evaluating the influence of pipeline geometry on the build-up and plugging process in pipelines.

INTRODUCTION

A vast amount of radioactive waste has been stored at Hanford spanning several decades. A majority of this waste is stored in tanks and is transferred in the slurry form between tanks and from tanks to processing facilities. A waste transfer system consisting of an extensive network of pipelines is used to facilitate the transfer operations. The main goal of the waste transfer system is to transfer the nuclear waste without plugging the transfer pipelines. Currently, two tools have been used to support this objective and include the Environmental Simulation Program (ESP) and empirical based critical velocity correlations. First, ESP is used to estimate the initial waste compositions and solids volume fraction. Then critical velocity correlations are used to estimate the minimum velocity to prevent settling of solids during waste transfers.

Despite such efforts, several lines have plugged during the waste transfer process at Hanford. The plugging has been attributed to two main factors: chemical instability and settling of solids. Chemical instability during waste transfers results is a phase change (from liquid to solid) initiated due to drops in temperature, changes in local concentration or mixing and pumping of wastes that are not in equilibrium. The solid phase precipitates or crystallizes depending on the solubility characteristics of the dissolved multiple species of the waste, their chemical interaction, and temperature. The solids may precipitate out of the solution and accumulate along the pipe walls. The pipe walls then serve as a nucleation site where the solids nucleate and grow rapidly and eventually form an interlocking needle-like crystal network. The needle-like crystal network impedes the flow within the pipe and commences the formation of the plug [3]. The presence of precipitates and/or agglomerates increases the solids concentration and increases viscosity of the slurry. The flow transitions from turbulent to laminar as a result of such changes during transit and the undissolved solids may settle when the flow velocity is not sufficient to keep them suspended. A moving bed of particles then begins to accumulate during slurry transport operation. Settling solids in a moving bed of particles form a stationary bed that eventually fills the pipe and blocks flow.

The blocked pipelines pose several problems at Hanford. The plugged pipelines are considered hazardous, hard and expensive to repair and cause significant time delays in the clean-up process. Consequently, most plugged transfer pipelines are abandoned. The phenomenon of settling of solids has been the subject of numerous theoretical and experimental studies [4, 5]; however, these require extensive experimental set-ups, procuring varied slurries, and carrying out lengthy experimental trials. The theoretical studies rely heavily on empirical formulae which do not take full account of the settling physics. A need exists for a computational tool that can investigate the influence of various parameters that affect the settling of solids and better aid in understanding the settling dynamics at a click of a button.

A two dimensional (2D) computational analysis has been carried out at FIU simulating settling of solids in a horizontal pipeline as a function of flow velocity, particle size and volume percent solids using the CFD software Comsol Multiphysics 4.3b. The numerical results are validated with empirical correlations and experimental results. The outline of the paper is given as follows: First, the governing equations for the mixture model simulations are introduced. Second, simulations modeling settling of solids are presented. Finally, conclusions are drawn and discussions for future work are presented.

NUMERICAL APPROACH

The multi-phase simulations focused on modeling the two-phase flow of mixtures in a pipe. The main goal behind multi-phase simulations was to understand the multi-physical factors that lead to solids settling in a pipeline. The mixture model is a macroscopic two phase model that is able to compute the flow for a mixture of a solid and liquid. It tracks the average phase concentration, or volume fraction and solves for one velocity field for each phase. The two phases consisted of one dispersed phase (solid particles) and one continuous phase (liquid). A brief overview of the cases simulated in the multi-phase environment is shown in Figure 28. The main aim behind the modeling efforts was to understand plug formation via two mechanisms: (1) settling of solids and (2) precipitation kinetics such as solids growth in a pipeline. The models were created in 2D and consisted of a horizontal pipe.

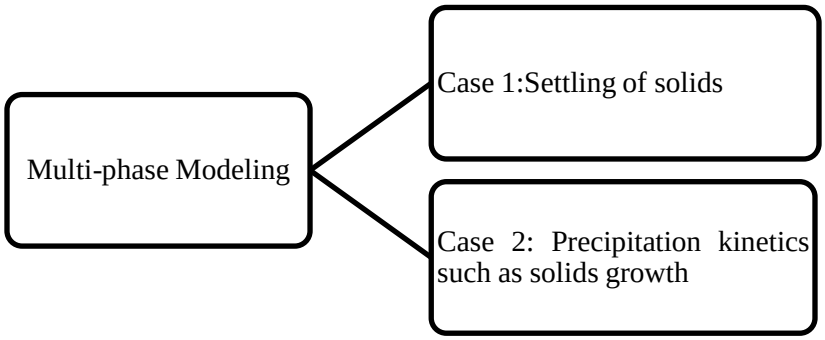

Figure 28. Cases simulated in the multi-phase modeling environment.

Governing Equations

The equations governing the mixture model were the momentum and continuity equations and a volume fraction solution for each phase was analyzed. Some of the assumptions made while using the model were that the density of each phase was constant; that the pressure field was same and that the velocity between the two phases could be ascertained from a balance of pressure, gravity, and viscous drag [6].

Momentum Equation

The momentum equation for the mixture was given by:

$$\rho u_t + \rho(u \cdot \nabla)u = -\nabla p - \nabla \cdot \tau_{Gm} + \rho g + F$$

$$-\nabla \cdot \left[\rho c_d (1 - c_d)\left(u_{slip} - \frac{D_{md}}{(1-c_d)\Phi_d}\nabla\Phi_d\right)\left(u_{slip} - \frac{D_{md}}{(1-c_d)\Phi_d}\nabla\Phi_d\right)\right] \quad (1)$$

where, u denotes mixture velocity (m/s), ρ is the mixture density (kg/m3), p is the pressure (Pa), c_d is the mass fraction of the dispersed phase (kg/kg), u_{slip} is the relative velocity between the two phases (m/s), τ_{Gm} is the sum of viscous and turbulent stress (kg/(m·s^2)), g is the gravity vector (m/s^2), and F is the additional volume forces (N/m^3).

The mixture velocity u was defined as:

$$u = \frac{\Phi_c \rho_c u_c + \Phi_d \rho_d u_d}{\rho} \quad (2)$$

Here, c and d denote the volume fractions of the continuous phase and the dispersed phase (m^3/m^3), respectively, u_c the continuous phase velocity (m/s), u_d the dispersed phase velocity (m/s), ρ_c the continuous phase density (kg/m^3), ρ_d the dispersed phase density (kg/m^3), and ρ the mixture density (kg/m^3).

The mixture density ρ was given by:

$$\rho = \Phi_c \rho_c + \Phi_d d \quad (3)$$

where ρ_c and ρ_d (kg/m^3) are the densities of each of the two phases.

The mass fraction of the dispersed phase c_d was given by:

$$c_d = \frac{\Phi_d \rho_d}{\rho} \quad (4)$$

The relative velocity between two phases was defined by:

$$u_d - u_c = u_{cd} = u_{slip} - \frac{D_{md}}{(1-c_d)\Phi_d} \nabla \Phi_d \quad (5)$$

Here, u_{slip} (m/s) denotes the relative velocity between the two phases and D_{md} is a turbulent dispersion coefficient (m^2/s) accounting for extra diffusion due to turbulent eddies.
The transport equation for Φ_d, the dispersed phase volume fraction, was:

$$\frac{\partial}{\partial t}(\Phi_d \rho_d) + \nabla \cdot (\Phi_d \rho_d u_d) = -m_{dc} \quad (6)$$

where, m_{dc} ($kg/(m^3 \cdot s)$) is the mass transfer rate from dispersed to continuous phase and u_d (m/s) is the dispersed phase velocity.

Assuming constant density for the dispersed phase:

$$\frac{\partial}{\partial t}(\Phi_d) + \nabla \cdot (\Phi_d u_d) = -\frac{m_{dc}}{\rho_d} \quad (7)$$

The continuous phase volume fraction Φ_c was:

$$\Phi_c = 1 - \Phi_d \quad (8)$$

Continuity Equation
The continuity equation for the mixture was:

$$\rho_t + \nabla \cdot (\rho u) = 0 \quad (9)$$

The Mixture Model interfaces assumed that the densities of each phase, ρ_c and ρ_d,were constant, and therefore used the following alternative form of the continuity equation of the mixture:

$$(\rho_c - \rho_d)\left[\nabla \cdot (1 - c_d)\mathbf{u}_{slip} - D_{md}\nabla\phi_d) + \frac{m_{dc}}{\rho_d}\right] + \rho_c(\nabla \cdot \mathbf{u}) = 0 \quad (10)$$

RESULTS & DISCUSSION

Settling of Solids

Several multiphase scenarios representing settling of solids conditions in a pipe were simulated using Comsol to study settling dynamics in a horizontal pipeline as a function of flow velocity, particle size and volume percent. The numerical results were validated with empirical correlations and experimental results.

Model Geometry and Boundary Conditions

The model geometry for the simulations consisted of a two dimensional (2D) horizontal pipe with a diameter of 0.078 meters and a length of 5.2 meters. The slurry was modeled as a Newtonian suspension consisting of solids particles dispersed in liquid. The mixture entered through the inlet at velocities characterizing turbulent flow regimes. The turbulence intensity and length scale were set to 5% and $0.07*r_{in}$ where r_{in} = 0.039 is the radius of the inlet. The solids were modeled as spherical solid particles of equal size with the particle size ranging from 14.4 to 220 μm. The solid volume fraction ranged from 2.9 to 9.8%. The solid densities ranged from 1000 to 8000 kg/m^3 and the liquid densities ranged from 999 to 1647 kg/m^3. The outlet was set to zero pressure, no viscous stress and the dispersed phase flow exited the pipe at mixture velocity. The walls had a no-slip boundary condition. A gravity node was added to account for gravity force in the negative y-direction over the entire domain. Initially, the velocity as well as the solids phase volume fraction was zero in the entire model domain. The mesh used to partition the model domain into sub-domains consisted of triangular elements. A finer mesh size was used at the walls compared to the rest of the model domain.

Numerical Simulations

The mixture model to simulate settling of solids was solved via a transient simulation. The behavior of settling was investigated as a function of flow velocity, particle size, solids density and solids volume fraction. Table 5 lists the material properties used for the numerical simulations.

Table 5. Model Inputs for Numerical Simulations

	Model Verification Study				
Test Configuration	**1**	**2**	**3**	**4**	**5**
Particle diameter (μm)	14.4	37.7	129.5	182.3	203.9
Solids Density (kg/m^3)	2500	7950	3770	2500	7950
Solids volume fraction (%)	9.8	9.3	8.7	7.4	3.0
Liquid density (kg/m^3)	1146	1647	1151	999	1026
Liquid viscosity (cP)	10.2	9.3	4.5	1.5	1.6

The material properties were obtained from the experimental tests done by Pacific Northwest National Laboratory (PNNL) to determine the critical velocity for Newtonian slurries [5]. The critical velocity obtained by the numerical simulations was compared with the experimental results of PNNL and with the empirical based critical velocity correlations. The numerical results were a good match with the experimental results and demonstrated the use of COMSOL Multiphysics 4.3b to accurately simulate the settling physics as shown in Figure 29.

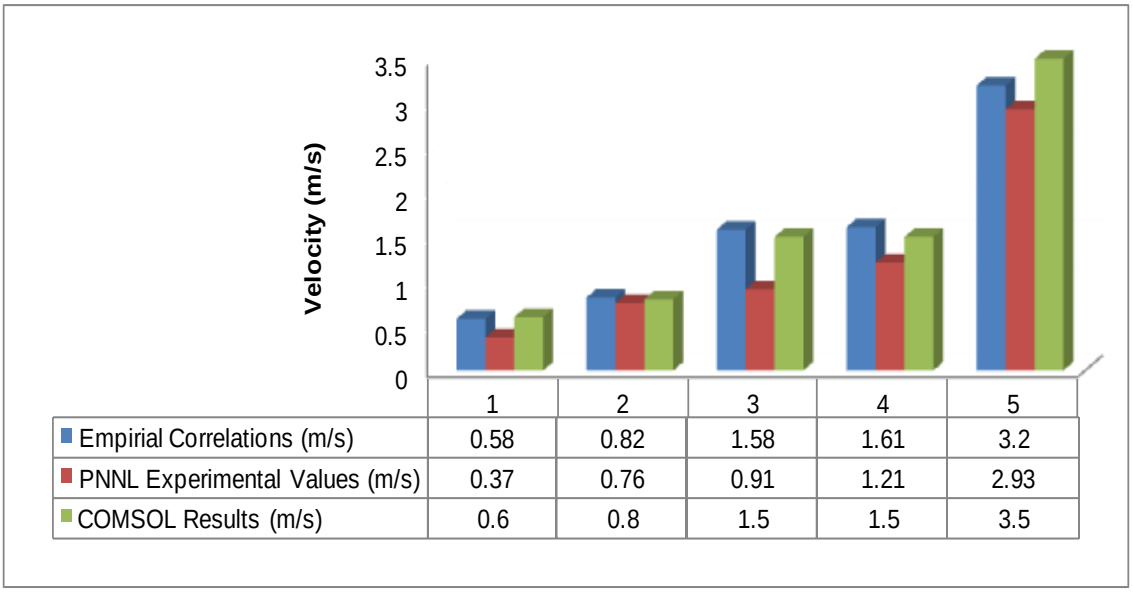

Figure 29. Comparison of numerical results to experimental and empirical results.

The main problem with using the critical velocity correlations to determine the velocity of the transfer operations is that the equation is based on single component density particles forming narrowband PSD. The use of the equation for multi-component density particles, broadband PSDs, and/or median particle sizes less than 100 μm (typical Hanford waste) requires extrapolation beyond the database used in the development of the equation. Hence, the equation should be used with caution when applied for any of these conditions. Moreover, the PSD is assumed to be static while deriving these correlations. But in actual waste transfers, the PSD is dynamic due to precipitation, particle agglomeration, and particle-surface interactions. The correlations do not provide information about the solids volume fraction, temperature, local

velocity profile, PSD, etc. along the length of the pipe nor any information on how these quantities change with time. The correlation is applicable for calculating the critical velocity of Newtonian fluids in straight, horizontal piping. When applied to non-Newtonian fluids in horizontal piping, these correlations under-predict the critical velocities [5]. Moreover, the transfer lines consists of vertical segments, pipe bends, tee's, reducers, jumpers, connectors and various other pipe components which can affect the critical velocity and plug formation process and the empirical formulae does not consider such complex piping components.

Influence of Particle Size

The effect of particle size on the settling dynamics was investigated using 45 µm and 200 µm size solids particles dispersed in water. The solids density was kept constant at 3147 kg/m^3 and the liquid density used was 1000 kg/m^3. The solids volume fraction was 2.9%. The simulations were carried out with entrance velocities ranging from 0.5 m/s to 2 m/s. The 45 µm and 200 µm particle concentrations at different velocities are shown in Figure 30 and Figure 31. The color legend represents the different solids concentration in the pipe.

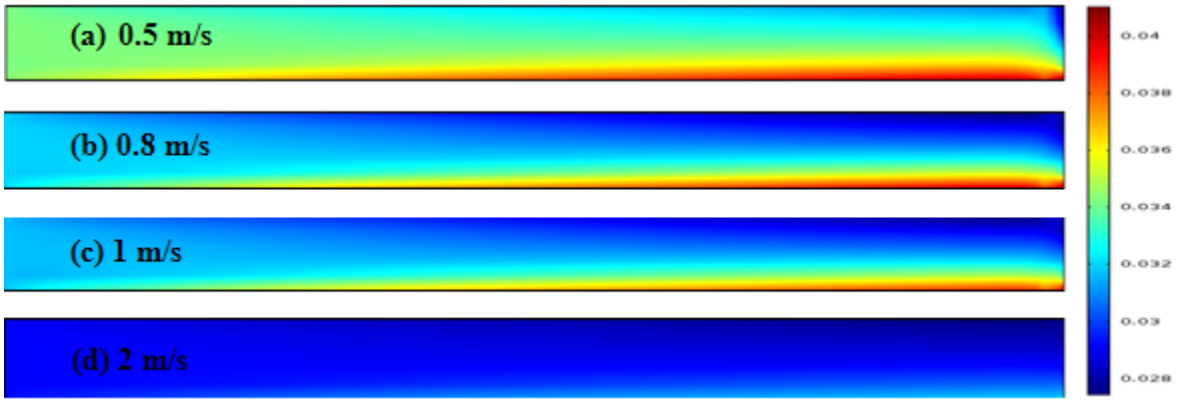

Figure 30. A 45 µm particle concentration along the pipe as a function of flow velocity ranging from 0.5 to 2 m/s.

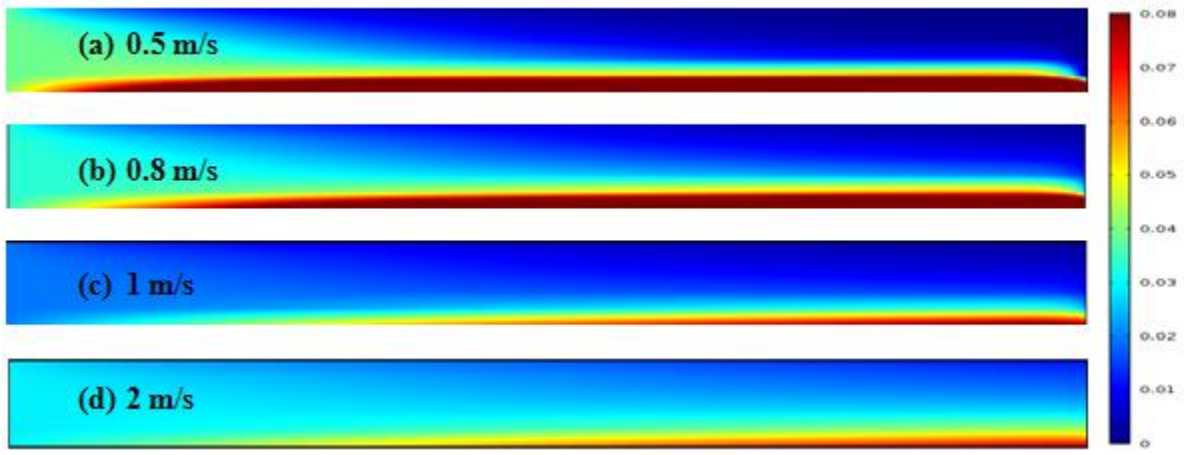

Figure 31. A 200 µm particle concentration along the pipe as a function of flow velocity ranging from 0.5 to 2 m/s.

The concentrations figures show that the 220 µm larger and heavier particles tend to settle fast on the bottom of the pipe, especially at low flow velocities. The simulations showed that flow velocities of lower than 1.0 m/s will create a stationary bed flow that eventually causes a plug to

form. For velocities of greater than 1.0 m/s, the fluid establishes a moving bed regime where the particles move along the bottom of the transfer pipe.

Influence of Solids Density

The effect of solids density on the settling dynamics was investigated by running simulations for the 45 µm particle size and 2.9% solids volume fraction at solids densities of 3147 kg/m^3 and 6300 kg/m^3. The entrance velocities used were 0.5 m/s, 1 m/s and 2 m/s. The results of the simulations are shown in Figure 32.

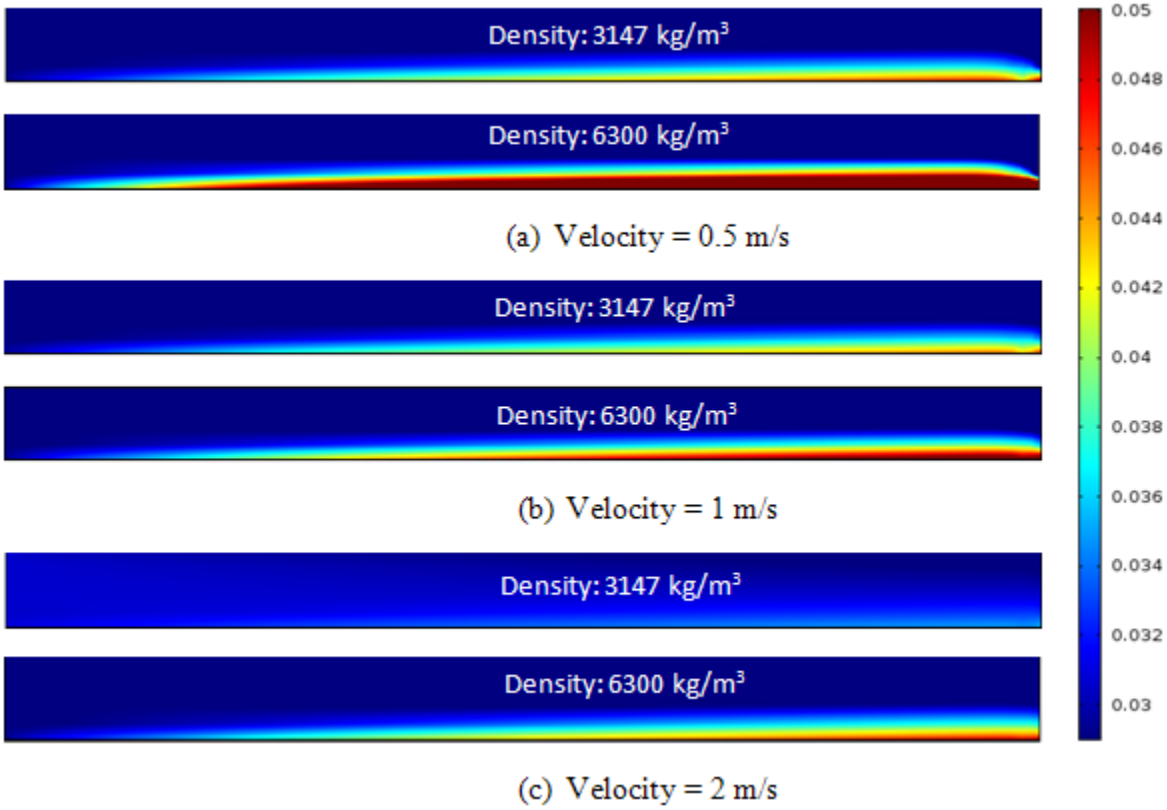

Figure 32. Settling of solids as a function of solids density for 45 µm particles at (a) 0.5 m/s, (b) 1 m/s and (c) 2 m/s.

The higher density slurries require a higher velocity to keep them suspended and prevent them from settling at the bottom compared to the lower density slurries. The critical velocity for the slurries with density of 3147 kg/m^3 was 0.7 m/s compared to the 4 m/s velocity obtained for the heavier slurries with density of 6300 kg/m^3.

Influence of Solids Volume Fraction

The effect of solids volume fraction on the critical velocity was investigated by running simulations for 45 µm particles with a solids density of 3147 kg/m^3. The solids volume fraction values were 2.9%, 5.8% and 10%, respectively. The critical velocities were calculated for each case and were numerically assessed as the velocity at which the solids were fully suspended in liquid and hence no settling was observed at the bottom of the pipe. For example, for the slurry consisting of 2.9% volume fraction of solids, the solids were observed to settle at 0.5 m/s and at 0.8 m/s. This can be seen as an increase in the solids volume fraction from the initial 2.9% to 4.19% and 3.68% at the respective velocities. As the velocity was further increased to 1 m/s, the

solids do not settle. They remain fully dispersed across the pipe length as the solids volume fraction stays the same as the initial volume fraction value (i.e., 2.9%). Any increase in the velocity thereafter shows that the solids remain fully suspended. Hence, the critical velocity calculated for the case with solids volume fraction of 2.9% is 1 m/s. Table 6 below shows the solids volume fraction values highlighted in red for the cases simulated and their corresponding measured critical velocities.

Table 6. Solids Volume Fraction Vs. Flow Velocity

Flow Velocity (m/s)	Solids volume fraction (2.9%)	Solids volume fraction (5.8%)	Solids volume fraction (10%)
0.5	4.19%	7.96%	12.84%
0.8	3.68%	7.09%	11.70%
1	2.90%	6.80%	11.36%
2	2.90%	6.29%	11.21%
4	2.90%	5.96%	11.01%
6	2.90%	5.96%	10.31%

As the solids volume fraction increases, the critical velocity increases, as expected. For instance, for the slurry with solids volume fraction of 2.9%, the critical velocity obtained is 1 m/s compared to the 4 m/s obtained for solids volume fraction of 5.8% and 6 m/s for the slurry with solids volume fraction of 10%.

Precipitation Kinetics

The modeling of precipitate kinetics such as solids growth required solving the coupled equations of flow and transport. Three physics interfaces were used to facilitate this as shown in Figure 33.

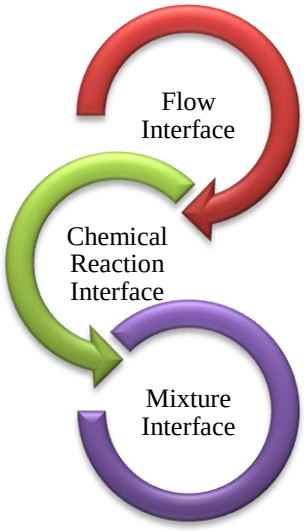

Figure 33. Multi-physics coupling for the conceptual model of simulating precipitate formation.

A brief description of the output for each interface is described below.

- ✓ Flow Interface was used to simulate flow fields along the pipe length.
- ✓ Transport of Chemical Reactions Interface was used to model multicomponent transport and evolution of chemical reaction between multiple species (A+B→C).
- ✓ Mixture interface was used to investigate multiphase interactions and solids growth in a pipeline was modeled.

First, the flow was solved using the Navier-Stokes equations of mass conservation and momentum balance. Next, the calculated velocity field was used as a model input for the transport of chemical reactions interface to study the progress of chemical species transported by diffusion and convection mechanisms. Finally, the mixture interface was used to simulate solids growth by combining the transport equation of chemical reaction interface with the transport equations of mixture interface. Since the output of chemical reaction interface was mass concentration, calculations were done to convert them to volume concentration and the conversion factor was used as an input condition to the mixture interface. The interactions between the multi-physics equations are shown below:

Flow Equations: $$\frac{\partial u}{\partial x}+\frac{\partial v}{\partial y}=0 \text{ and } \rho_c\left(u\frac{\partial u}{\partial x}+v\frac{\partial u}{\partial y}\right)=\frac{\partial p}{\partial x}+\mu\nabla^2 u+F_x \quad (11)$$

Chemical Reaction Equation: $$\frac{\partial c}{\partial t}+u\cdot\nabla c=\nabla\cdot(D\nabla c)+R \quad (12)$$

Mixture Equations: $$(\rho_c-\rho_d)\left[\nabla\cdot(1-c_d)u_{slip}-D_{md}\nabla\Phi_d)+\frac{m_{dc}}{\rho_d}\right]+\rho_c(\nabla\cdot u)=0 \quad (13)$$

$$\rho u_t+\rho(u\cdot\nabla)u=-\nabla p-\nabla\cdot\tau_{Gm}+\rho g+F-\nabla\cdot\left[\rho c_d(1-c_d)\left(u_{slip}-\frac{D_{md}}{(1-c_d)\Phi_d}\nabla\Phi_d\right)\right] \quad (14)$$

where,

ρ_c	fluid density (kg/m^3)
p	fluid pressure (Pa)
F_x	force term accounting for gravity or other body forces
u and v	velocity components in the x and y directions
c	concentration of the species (mol/m^3)
D	diffusion coefficient (m^2/s)
R	reaction rate expression for the species (mol/(m^3·s))
ρ_d	solids density (kg/m^3)
c_d	mass fraction of the dispersed phase (kg/kg)
u_{slip}	relative velocity between the two phases (m/s)
τ_{Gm}	sum of viscous and turbulent stress (kg/(m·s^2))
g	gravity vector (m/s^2)
m_{dc}	mass transfer rate from solids to liquid phase (kg/(m^3·s))

Model Geometry and Boundary Conditions

The model geometry for the simulations consisted of a two-dimensional (2D) horizontal pipe with a diameter of 0.078 meters and a length of 1.84 meters. The reacting flow entered at the inlet and exited at the outlet. The suspension consisted of solids dispersed in water. A gravity node was added to account for gravity force in the negative y-direction over the entire domain. Initially, the velocity, chemical concentrations of reacting species and solids phase volume

fraction was zero in the entire model domain. The mesh used to partition the model domain into sub-domains consisted of triangular elements. A finer mesh size was used at the walls compared to the rest of the model domain to obtain better convergence of the model as shown in Figure 34.

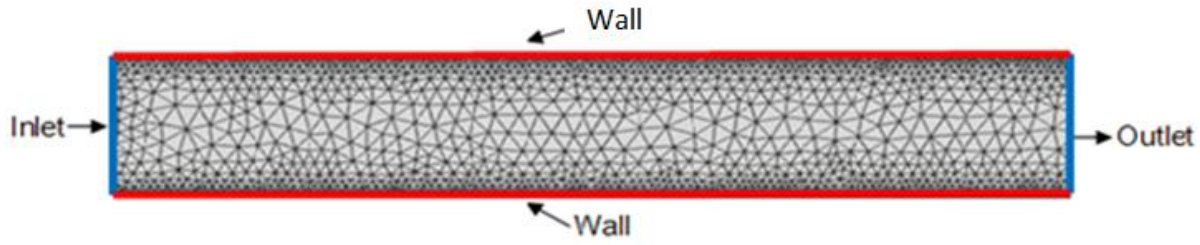

Figure 34. Model geometry and mesh.

Model Inputs

The model inputs used for the three interfaces are shown in Figure 35. The flow output was used as input to the chemical interface to simulate an irreversible chemical reaction involving three species. The chemical reaction resulted in the formation of product species whose units were in terms of molar concentration. Since the mixture interface uses volume fraction as an input, the data output of chemical interface was exported to a text file wherein the data was converted from molar concentration to volume fraction. Then, the text file with the conversion factor was imported back and used as an input condition to the mixture interface to simulate solids growth in a pipeline.

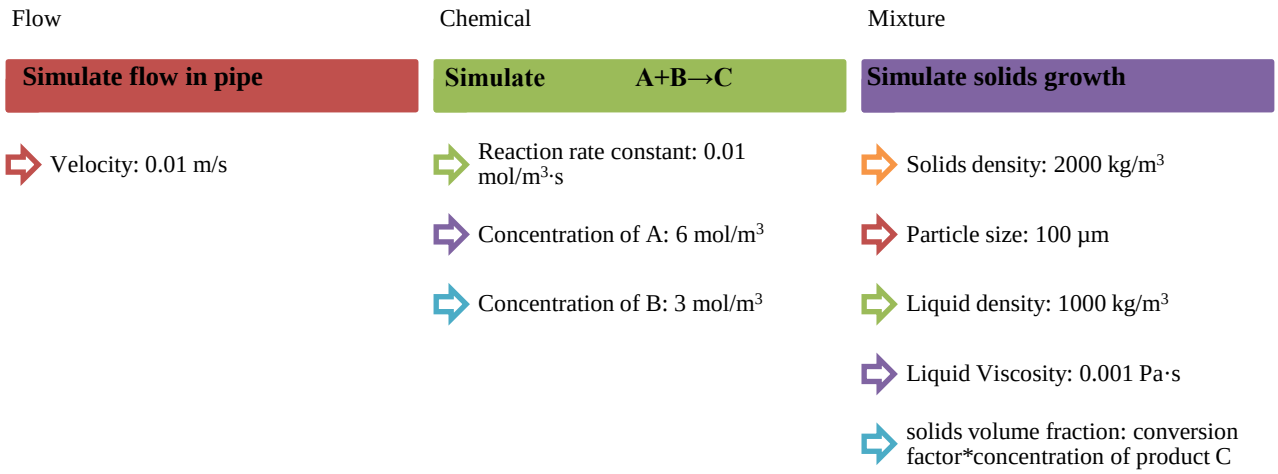

Figure 35. Model inputs used for the numerical simulations.

Velocity Profile

The flow interface was solved first to compute the velocity fields within the model domain. The flow became fully developed once it passed the entrance region. The slice plot of flow velocity along the cross sections of the pipe is shown in Figure 36. The maximum velocity is shown by the red color whereas lower velocity is characterized by the blue color.

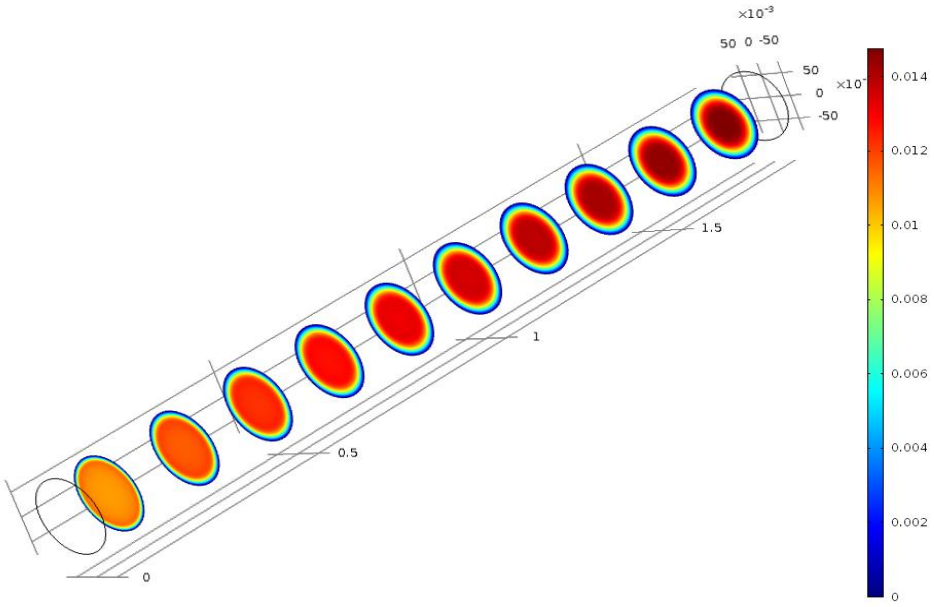

Figure 36. Velocity profile along the cross-sections of the pipe.

Concentration Profile

The calculated velocity field from the flow interface was next used as an input to the chemical reaction interface to study the evolution of chemical species transported by diffusion and convection mechanism. An irreversible, isothermal chemical reaction with three species (A+B→C) was simulated within the pipe. Here, species A and B were the reactants and species C was the product that was formed. A reaction rate constant was applied that governed the reaction kinetics between the species. The concentration of species A decreased from 6 mol/m^3 to about 4.5 mol/m^3 as it underwent the chemical reaction and got consumed (Figure 37).

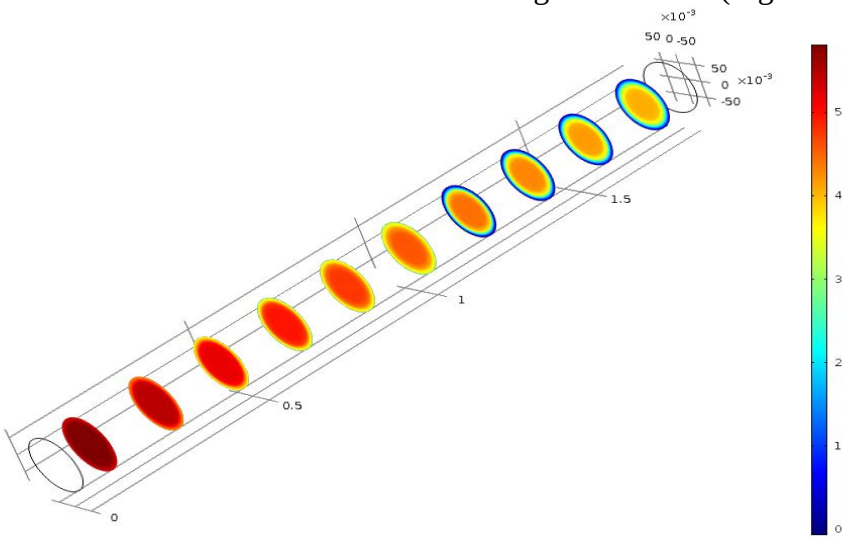

Figure 37. Concentration snapshot of species A as it undergoes a chemical reaction.

At the same time, the concentration of species C increased from 0 mol/m^3 to 1.8 mol/m^3 as it got produced in the pipeline as shown in Figure 38.

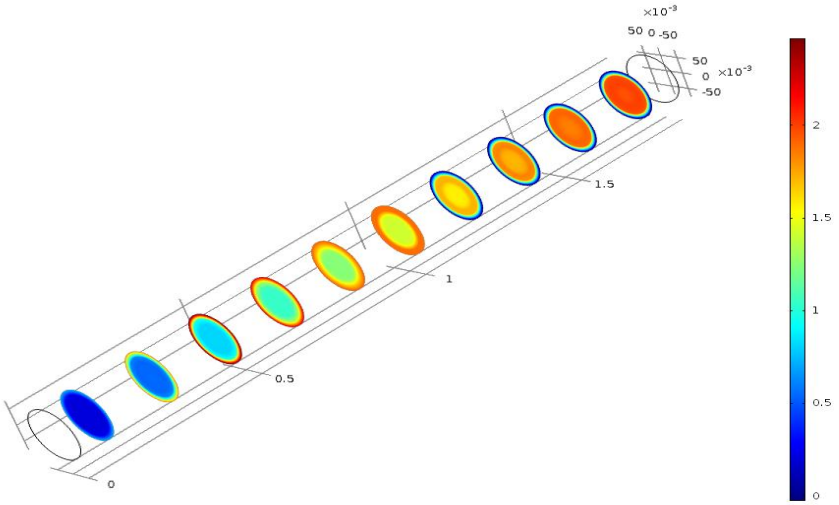

Figure 38. Concentration snapshot of species C as it undergoes a chemical reaction.

The growth profile of product species C obtained from solving the coupled chemical reaction-flow interfaces was next used to simulate solids growth in a pipeline. The idea was to model the precipitation kinetics which involves a gradual increase in solids concentration as they react. This translates in an increase in the volume fraction of solids in a pipeline. Since the concentration output of the chemical reaction interface is in molar concentration, the data was exported into a text file and converted to the volume fraction units. This required taking into consideration the molarity and solids density values. After the data conversion was completed, the data file was imported back into the model to simulate the growth of solids in a pipeline. The mixture interface consisted of two phases: continuous phase (water) and a dispersed phase (solids). The solids were assumed to be of spherical shape with particle size of 100 µm. The sum of the two phases was equal to 1. Initially, the pipe had zero volume fractions of the solids (i.e., it was 100% filled with water). Hence, the volume fraction of the continuous phase was 1 at the start of the simulation. The volume fraction of the continuous phase decreased from 1 to 0.983 as the solids gradually grew in the pipeline and displaced the water as shown in Figure 39.

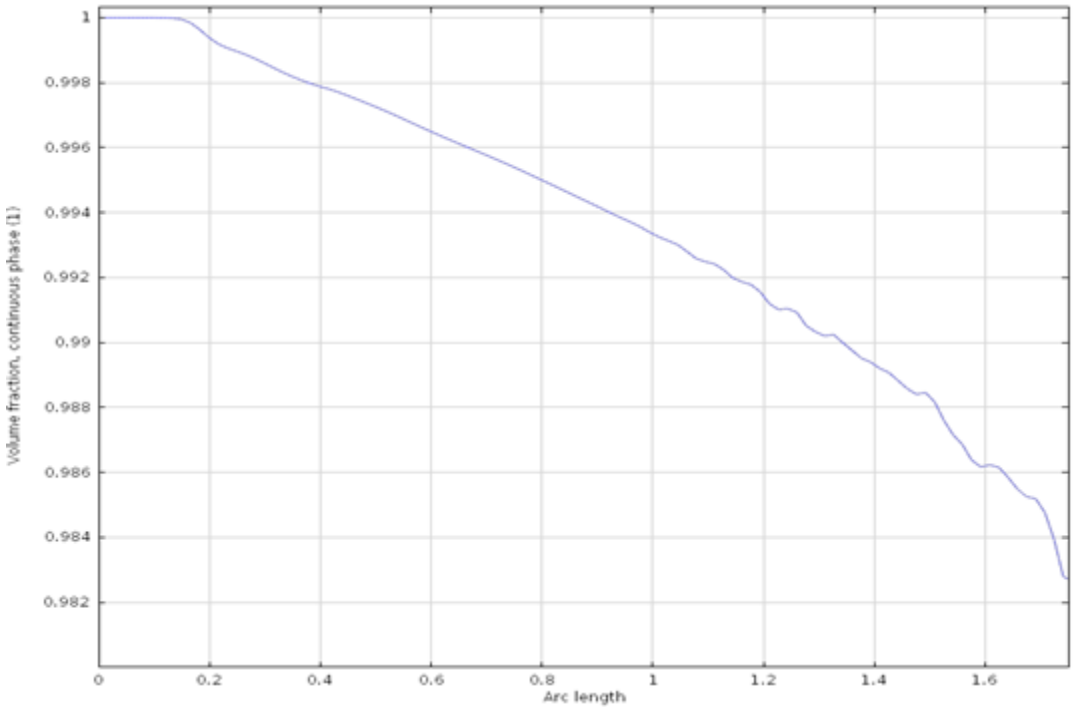

Figure 39. Line graph showing volume fraction continuous phase along the pipe length.

At the same time, the volume fraction of the solids increased from 0 to about 0.0177 as they gradually formed along the pipe length (Figure 40).

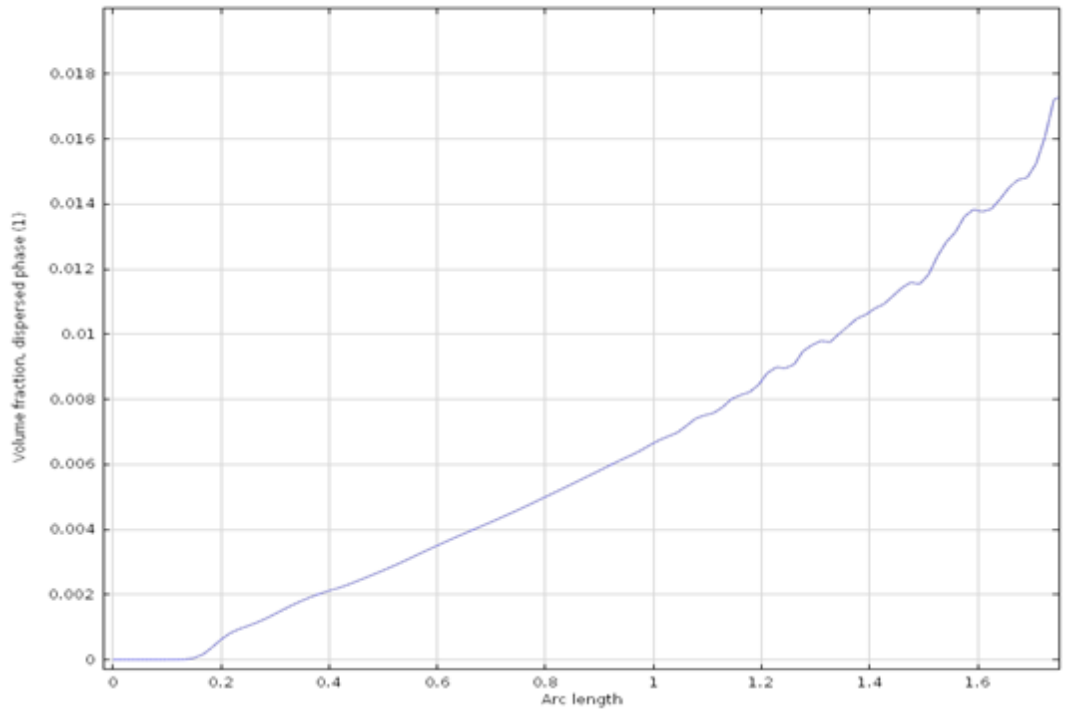

Figure 40. Line graph showing volume fraction of dispersed phase along the pipe length.

CONCLUSIONS AND FUTURE WORK

Baseline models integrating flow, chemical and mixture interfaces were used to study pipeline plug formation via settlings of solids and precipitation kinetics using Comsol Multiphysics 4.3b. The influence of temperature on the chemical flow interactions was neglected. The numerical results showed promising progress towards simulating the different mechanisms that leads to the onset of plug formation. The numerical results simulating settling of solids compared very well with the experimental results and empirical correlations. The influence of particle size, solids volume fraction and flow velocity on the solids deposition process was better understood. A manual coupling was used to study the chemical and mixture interactions that lead to the solids growth in a pipeline (precipitation kinetics). An automated system that could easily couple the three interfaces needs to be further investigated. Future work will also include incorporating highly concentrated slurries to visualize higher volume fractions of solids formed in a pipeline that eventually leads to the onset of plug formation. The influence of pipeline geometry on settling dynamics will also be studied to better understand the plugging process. Simulations will also be performed to investigate the plug formation as a function of rate kinetics and temperature.

REFERENCES

1. Lindner, J. S. et al., (2002), Dial/MSU Prevention of Solids Formation FY 2000 Status Report Part II: Modeling of Slurry Transport and Saltwell Pumping, reported in ORNL/TM-2000/302, Mississippi State University, Starkville, Mississippi.
2. Rector, D. R., Stewart, M. L., Poloski, A. P., (2009), Modeling of Sediment Bed Behavior for Critical Velocity in Horizontal Piping, Pacific Northwest National Laboratory, and Richland, Washington.
3. Servin, M.A. et al., (2012) "Feasibility Study of Pressure Pulsing Pipeline Unplugging Technologies for Hanford", Washington River Protection Solution, LLC, Richland, Washington.
4. Bae K.S. et al., (1991), "Empirical Correlation for the Minimum Transport Velocity of Multidisperse Slurries in Horizontal Pipes", Korean Journal of Chemical Engineering 8(2):120–124.
5. Poloski, A. P. et al., (2009), "Deposition Velocities of Newtonian and Non-Newtonian Slurries in Pipelines", PNNL-17639, WTP-RPT-175, Rev-0, Pacific Northwest National Laboratory, Richland, Washington.
6. www.comsol.com

TASK 17.1 FY13 YEAR END TECHNICAL REPORT Multiple-Relaxation-Time Lattice Boltzmann Model for Multiphase Flows

EXECUTIVE SUMMARY

Many engineering processes at various U.S. Department of Energy sites include the fluid flow of more than one phase such as air and water. Slurry mixing methods such as pulsed-air mixers, air sparging, and pulsed-jet mixing are a few examples where more than one fluid phase can exist in contact with another phase. Lattice Boltzmann method (LBM) is a computational fluid dynamics (CFD) method that can provide insight into the behavior of multiphase flows by capturing the interface dynamics accurately during the process and the effects of structures on multiple fluid phases.

Florida International University (FIU) aims to develop LBM-based computer codes that can be used by the U.S. DOE scientists and engineers as a prediction tool for understanding the physics of fluid flow in nuclear waste tanks during regular operations and retrieval tasks. In FY2009, a new task was initiated within FIU's research project on high-level-waste (HLW) in order to develop a computational code, which is based on the LBM in order to simulate multiphase flow problems related to HLW operations. A thorough literature review was conducted to identify the most suitable multiphase fluid modeling technique in LBM and a single-phase multi-relaxation-time (MRT) code was developed. In FY2010, FIU identified and evaluated a multiphase LBM using a single-relaxation-time (SRT) collision operator and updated the collision process in the computer code with an MRT collision model. In FY2011, the MRT LBM code was extended into three dimensions and the serial computer code was converted into a parallel code. In FY2012, a contact angle method was implemented and a feature was developed to import complex geometries into LBM.

This report presents the theoretical and numerical aspects of the multiphase flow simulations conducted within this task. The results have shown that the LBM has the capability to model the behavior of multiphase, stress-dependent flow of viscoplastic materials. The software package with all of its existing features needs additional development to be ready for deployment at DOE sites mostly in the simulation of turbulent, high velocity jet penetration flows to replicate the pulsed-jet mixer (PJM) behavior in waste tanks. In addition, validation and verification studies would be helpful in understanding the accuracy and uncertainty in the simulations results.

INTRODUCTION

As a result of atomic weapons production, millions of gallons of radioactive waste were generated and stored in underground tanks at various U.S Department of Energy (DOE) sites. The DOE is currently employing a variety of methods for storing, retrieving, transferring, and processing some of these wastes. When the waste is in its stored or processed phases, certain issues arise that require attention and understanding. In its stored state, the waste is capable of producing gases that can result in a gas release event (GRE), which has the potential to be explosive and very dangerous to those working in close proximity. Further, various waste retrieval and processing methods are employed during storage and transfer of the waste. The most used methods are pulse jet mixers (PJM), which are the primary method for processing, and the complimentary method of air sparging. Both methods use vacuums and slurry injection to mix the waste.

In the tanks found at the Hanford Site, there exists a thick layer of a slurry-like fluid composed of radioactive and chemical products, which are known to generate gases that are flammable. The strength and geometry of these slurries have a direct impact on gas release, which is shown to be characterized by one single physical property, their initial shearing/yielding strength [1]. As such, mixing and storage systems were analyzed during normal operation with waste slurries exhibiting a non-Newtonian rheology to determine their ability to achieve safe and controllable release of flammable gasses [2]. There is great importance placed on understanding the nature of the waste slurry behavior using computational methods.

To combat the problem of gas formation with unintended release, a technique of mixing is employed that is able to release these bubbles in a controlled way; this same method is used for processing and transport. One practice used is known as pulsed jet mixing and is characterized by a vacuum extracting the waste and then re-introducing it back into the tank, resulting in mixing. The physical characteristics of the slurry being mixed have a direct impact on the mixing behavior as well as the zone of influence and cavern formation [3]. Bingham fluids in the tank have shear rates and viscosities that vary extensively, from extremely high near the jet pump and nozzle exit to negligibly small in regions away from the influence of the jet itself. Because of this behavior and the large variation in fluid viscosity, there will be a large variation in the mixing behavior [4]. The other technique employed is air sparging and this method is faced with the same issues that are found with pulse jet mixers when dealing with non-Newtonian slurries [5].

In this paper, a numerical method known as the lattice Boltzmann method (LBM) is presented that can model multiphase non-Newtonian flows accurately and efficiently. Special attention was given to fluid behavior characterized as Bingham plastic. This introduces another challenge in terms of instabilities to LBM simulations for multiphase flows with initial stress and strain relationships that are not linear. This is produced by the rheology of Bingham plastics which imply a certain threshold of stress must be produced in order for yielding and flow to occur. The current LBM presented in this paper is able to provide stable and accurate simulations of Bingham plastics and the interactions between the fluid and the gas phases.

An overview of various multiphase LBM approaches is presented first. Second, the governing equations for the lattice Boltzmann method used in this paper are introduced. After that, the applications to dynamic multiphase flows are shown and a procedure to extend LBM to non-Newtonian fluids is presented. Following that, we present the applications to injection type flows

and a procedure to impose inflow boundary conditions in LBM for non-Newtonian fluids is presented. Finally, conclusions are provided and future work is discussed.

LBM FOR BINGHAM CHARACTERIZED MULTI-PHASE FLOW

The simulation of power-law fluids using the LBM was shown in the work of Aharonov and Rothman for non-Newtonian flows in porous media by modifying the relaxation time parameter in order to relate the viscosity to the stress tensor [6]. Gabbanelli et al. also improved this approach to shear thickening and shear thinning fluids by proposing a truncated power-law model [7]. Boyd et al. further improved this approach by proposing a second-order accurate calculation of the shear-rate [8], which was later used by Tang et al. [9] to simulate electric field effects on non-Newtonian fluids using LBM. Power-fluid simulations were also conducted in the study of Yoshino et al. [10] with their lattice kinetics approach where the relaxation parameter is fixed to one for stability purposes and the effect of the shear-rate on the viscosity is achieved via a constant parameter added to the equilibrium distribution function.

To date, there have been a limited number of studies that correlate the use of the lattice Boltzmann method with Bingham fluids. Of these, Wang and Ho used the expression for the shear stress proposed by Papanastasiou [11] to avoid the discontinuity in the definition of the shear stress; this occurs for Bingham plastics depending on the local stress value [12]. By using a large exponential growth factor in the definition of the shear stress, Wang and Ho were able to approximate the shear stress relationship to the shear rate for Bingham plastics. They also derived a new equilibrium distribution function that incorporates the local shear-rate effect. Recently, Tang et al. applied the same theory to the pressure-based He-Luo incompressible LBM to remove the compressibility effects in the simulations [13]. A similar approach was taken by Yoshino et al. where the equilibrium function incorporates a constant non-Newtonian parameter that determines the fluids viscosity. In this method, the shear-dependent viscosity is acquired by using a variable parameter related to the local shearing rate. This method also keeps the BGK collision term at one to produce numerical stability. Leonardi et al. assumed a slightly different approach to encompass a wide range of fluid dynamic environments. The power law and Bingham model (Papanastasiou approach) were used and were hydro-dynamically coupled to the discrete element method to account for structural interactions [14]. In contrast, Vikhansky has implemented an implicit method by calculating the collision rate so that the stress and shear rate are simultaneously satisfying the constitutive equations. In addition, this approach necessitates analytically solving at each time step and at each node a one-dimensional non-linear equation [15]. Chai et al. has also developed the application of LBM for modeling generalized Newtonian fluid flows including the Bingham plastics, using the multiple-relaxation-time (MRT) collision model to improve the stability of the method for low viscosities [16]. Finally, a promising method has been presented by Frank and Li, where they were able to produce a two-phase bubble rising model by coupling the free energy method with a sixth-order Maxwell model that incorporates shear thinning effects [17].

Numerical Method

The lattice Boltzmann method developed for this task is based on the continuous Boltzmann equation given by

$$\frac{\partial f}{\partial t} + \boldsymbol{\xi} \cdot \nabla f + \boldsymbol{F} \cdot \nabla_{\xi} f = \Omega. \tag{15}$$

Here f is the single particle density distribution function, $\boldsymbol{\xi}$ is the particle velocity, $\boldsymbol{F}$ is the combination of interfacial force and external body forces such as gravity and wall adhesion force and Ω is the collision term. The term $\nabla_{\xi} f$ can be approximated as,

$$\nabla_{\xi} f \approx \nabla_{\xi} f^{eq} = -\frac{\xi - \mathbf{u}}{\rho c_s^2} f^{eq}\,, \tag{16}$$

where f^{eq} is the equilibrium density distribution function, $\mathbf{u}$ is the macroscopic velocity, ρ is the density and c_s is the speed of sound. The continuous Boltzmann equation given in Eq. (1) can be discretized in the velocity space by expressing as

$$\frac{\partial f_\alpha}{\partial t} + \boldsymbol{\xi_\alpha} \cdot \nabla f_\alpha = \Omega + S_{f\alpha}, \tag{17}$$

where

$$e_\alpha \equiv \xi_\alpha = \begin{cases} (0,0,0) & , \quad \alpha = 0, \\ (\pm 1,0,0), (0,\pm 1,0), (0,0,\pm 1), & , \quad \alpha = 1,2,\cdots,6 \\ (\pm 1,\pm 1,0), (\pm 1,0,\pm 1), (0,\pm 1,\pm 1) & , \quad \alpha = 7,8,\cdots,18 \end{cases} \tag{18}$$

and

$$S_{f\alpha} = \frac{(e_{\alpha i} - u_i)(F_i + F_i^w + G_i)}{\rho c_s^2} f_\alpha^{eq}\,. \tag{19}$$

In Eq. (4) α is the discrete particle velocity distribution using the D3Q19 lattice structure shown in Figure 41, e is the particle velocity between lattice points.

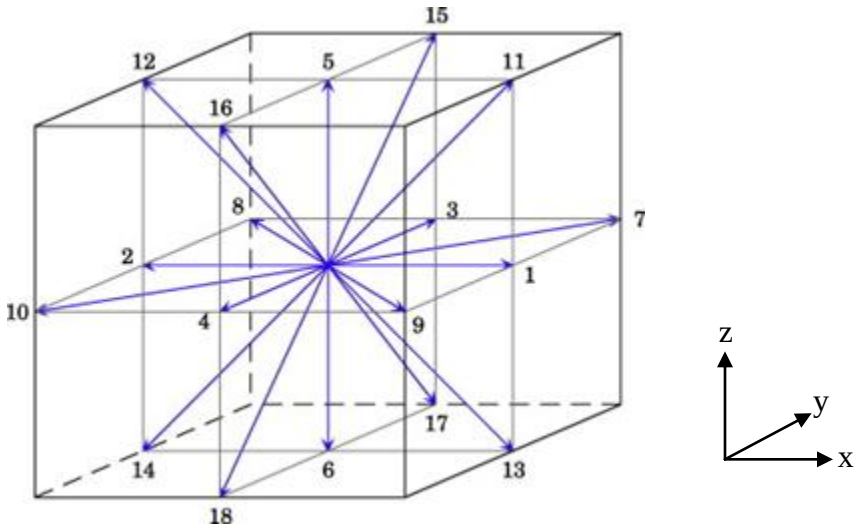

Figure 41. D3Q19 lattice structure.

In the single-relaxation-time LBM, the collision term Ω is represented using the BGK model that uses a single relaxation time parameter (λ), $\Omega_c = -\left(\frac{f_\alpha - f_\alpha^{eq}}{\lambda}\right)$. In the MRT LBM, using a collision matrix Λ, the collision term on the right hand side of Eq. (3) is represented by

$$\Omega = -\Lambda_{\alpha\beta}\left(f_\beta - f_\beta^{eq}\right). \tag{20}$$

The equilibrium distribution function, f_α^{eq}, is written as

$$f_\beta^{eq} = w_\alpha \rho \left[1 + \frac{e_{\alpha i} u_i}{c_s^2} + \frac{(e_{\alpha i} e_{\alpha j} - c_s^2 \delta_{ij}) u_i u_j}{2 c_s^4}\right], \tag{21}$$

where w_α is the weight function given by

$$w_\alpha = \begin{cases} 1/3, & \alpha = 0, \\ 1/18, & \alpha = 1,2,\cdots 6, \\ 1/36, & \alpha = 7,8,\cdots 18. \end{cases} \tag{22}$$

The force F_i in Eq. (5) is responsible for phase separation and is given by

$$F_i = \frac{\partial}{\partial x_j}(\rho c_s^2 - P)\delta_{ij} + \kappa\rho \frac{\partial}{\partial x_i}\frac{\partial^2 \rho}{\partial x_j \partial x_j}. \tag{23}$$

Here, P is the pressure and κ is the surface tension parameter which is related to the surface tension σ through the relation

$$\sigma = \kappa \int \left(\frac{\partial \rho}{\partial r}\right)^2 dr\,, \tag{24}$$

where r is the direction of integration normal to the interface. The force F_i is expressed by Lee and Lin [36] as

$$F_i = \frac{\partial \rho c_s^2}{\partial x_j}\delta_{ij} - \rho \frac{\partial}{\partial x_i}\left(\frac{\partial E_f}{\partial \rho} - \kappa \frac{\partial^2 \rho}{\partial x_j \partial x_j}\right). \tag{25}$$

E_f is the excess free energy at the interface over the bulk free energies and is obtained from an equation of state (EOS) expressed as follows:

$$E_f(\rho) \approx \beta\left(\rho - \rho_g^{sat}\right)^2 (\rho - \rho_l^{sat})^2\,, \tag{26}$$

where β is a constant and ρ_g^{sat} and ρ_l^{sat} are densities of gas and liquid phases at saturation, respectively. This EOS results in a density profile given by

$$\rho(z) = \frac{\rho_l^{sat} + \rho_g^{sat}}{2} - \frac{\rho_l^{sat} - \rho_g^{sat}}{2}\tanh\left(\frac{2z}{D}\right), \tag{27}$$

where z is the spatial location normal to the interface and D is the interface thickness.

The constant β along with κ can control D and σ through the relation

$$D = \frac{4}{\left(\rho_l^{sat} - \rho_g^{sat}\right)}\sqrt{\frac{\kappa}{2\beta}}, \tag{28}$$

and

$$\sigma = \frac{\left(\rho_l^{sat} - \rho_g^{sat}\right)^3}{6}\sqrt{2\kappa\beta}. \tag{29}$$

The forcing term $F_i^w = -\rho K_w \boldsymbol{n}$ that also appears in Eq. (5) is introduced to represent the effect of surface molecules where K_w is the parameter that determines whether the solid surfaces act

attractive or repulsive. In addition, the gravitational force is implemented in Eq. (5) via the $G_i = \rho \boldsymbol{g}$ force term where $\boldsymbol{g}$ stands for the gravitational acceleration vector.

The evolution equations given above for the particle density distribution function is mapped into the moment space by multiplying the terms in Eq. (3) with the transformation matrix $\boldsymbol{T}$

$$\boldsymbol{T}^T = \begin{bmatrix} \langle\rho|, \langle e|, \langle e^2|, \langle j_x|, \langle q_x|, \langle j_y|, \langle q_y|, \langle j_z|, \langle q_z| \\ \langle 3p_{xx}|, \langle 3\pi_{xx}|, \langle p_{ww}|, \langle \pi_{ww}|, \langle p_{xy}|, \langle p_{yz}|, \langle p_{xz}|, \langle m_x|, \langle m_y|, \langle m_z| \end{bmatrix}, \tag{30}$$

where

$$|\rho\rangle = |e_\alpha|^0, \tag{31}$$

$$|e\rangle_\alpha = 19|e_\alpha|^0 - 30, \tag{32}$$

$$|e^2\rangle_\alpha = (421|e_\alpha|^{04} - 53|e_\alpha|^2 + 24)/2 \tag{33}$$

$$|j_x\rangle_\alpha = e_{\alpha,x}, \tag{34}$$

$$|q_x\rangle_\alpha = \lfloor 5|e_\alpha|^2 - 9)\rfloor e_{\alpha,x}, \tag{35}$$

$$\left|j_y\right\rangle_\alpha = e_{\alpha,y}, \tag{36}$$

$$\left|q_y\right\rangle_\alpha = \lfloor 5|e_\alpha|^2 - 9)\rfloor e_{\alpha,y}, \tag{37}$$

$$|j_z\rangle_\alpha = e_{\alpha,z}, \tag{38}$$

$$|q_z\rangle_\alpha = \lfloor 5|e_\alpha|^2 - 9)\rfloor e_{\alpha,z}, \tag{39}$$

$$|3p_{xx}\rangle_\alpha = 3e_{\alpha,x}^2 - |e_\alpha|^2, \tag{40}$$

$$|3\pi_{xx}\rangle_\alpha = (3|e_\alpha|^2 - 5)\left(3e_{\alpha,x}^2 - |e_\alpha|^2\right), \tag{41}$$

$$|p_{ww}\rangle_\alpha = e_{\alpha,y}^2 - e_{\alpha,z}^2, \tag{42}$$

$$|\pi_{ww}\rangle_\alpha = (3|e_\alpha|^2 - 5)\left(e_{\alpha,y}^2 - e_{\alpha,z}^2\right), \tag{43}$$

$$\left|p_{xy}\right\rangle_\alpha = e_{\alpha,x}e_{\alpha,y}, \tag{44}$$

$$\left|p_{yz}\right\rangle_\alpha = e_{\alpha,y}e_{\alpha,z}, \tag{45}$$

$$|p_{xz}\rangle_\alpha = e_{\alpha,x}e_{\alpha,z}, \tag{46}$$

$$|m_x\rangle_\alpha = \left(e_{\alpha,y}^2 - e_{\alpha,z}^2\right)e_{\alpha,x}, \tag{47}$$

$$\left|m_y\right\rangle_\alpha = \left(e_{\alpha,z}^2 - e_{\alpha,x}^2\right)e_{\alpha,y}, \tag{48}$$

$$|m_z\rangle_\alpha = \left(e_{\alpha,x}^2 - e_{\alpha,y}^2\right)e_{\alpha,z}. \tag{49}$$

The resulting evolution equation in moment space takes the form

$$\frac{\partial \hat{f}_\alpha}{\partial t} + \hat{\boldsymbol{\xi}}_{\boldsymbol{\alpha}} \cdot \nabla \hat{f}_\alpha = -\hat{\Lambda}_{\alpha\beta}\left(\hat{f}_\beta - \hat{f}_\beta^{eq}\right) + \hat{S}_{f\alpha}, \tag{50}$$

where

$$\hat{f}_\alpha = \boldsymbol{T} f_\alpha, \tag{51}$$

$$\hat{f}_\alpha^{eq} = \boldsymbol{T} f_\alpha^{eq}, \tag{52}$$

$$\hat{S}_{f\alpha} = \mathbf{T} S_{f\alpha}\,, \tag{53}$$

and

$$\hat{\Lambda} = \boldsymbol{T}\Lambda\boldsymbol{T}^{-1}. \tag{54}$$

The equilibrium distribution function in moment space is written as

$$(\hat{f}^{eq})^T = \begin{bmatrix} \rho, e^{eq}, (e^2)^{eq}, j_x, q_x^{eq}, j_y, q_y^{eq}, j_z, q_z^{eq} \\ 3p_{xx}^{eq}, 3\pi_{xx}^{eq}, p_{ww}^{eq}, \pi_{ww}^{eq}, p_{xy}^{eq}, p_{yz}^{eq}, p_{xz}^{eq}, m_x^{eq}, m_y^{eq}, m_z^{eq} \end{bmatrix}, \tag{55}$$

where the equilibrium distributions of the moments are given by

$$e^{eq} = -11\rho + 19(j_x^2 + j_y^2 + j_z^2)/\rho, \tag{56}$$

$$(e^2)^{eq} = w_\varepsilon \rho + w_{\varepsilon j}(j_x^2 + j_y^2 + j_z^2)/\rho, \tag{57}$$

$$q_x^{eq} = -\frac{2}{3} j_x, \tag{58}$$

$$q_y^{eq} = -\frac{2}{3} j_y, \tag{59}$$

$$q_z^{eq} = -\frac{2}{3} j_z, \tag{60}$$

$$p_{xx}^{eq} = \frac{1}{3}\left(2j_x^2 - \left(j_y^2 + j_z^2\right)\right)/\rho, \tag{61}$$

$$\pi_{xx}^{eq} = w_{xx} p_{xx}^{eq}, \tag{62}$$

$$p_{ww}^{eq} = \left(j_y^2 - j_z^2\right)/\rho, \tag{63}$$

$$p_{xy}^{eq} = \left(j_x j_y\right)/\rho. \tag{64}$$

$$p_{yz}^{eq} = \left(j_y j_z\right)/\rho. \tag{65}$$

$$p_{xz}^{eq} = (j_x j_z)/\rho. \tag{66}$$

$$\pi_{ww}^{eq} = w_{xx} p_{ww}^{eq}, \tag{67}$$

$$m_x^{eq} = 0, \tag{68}$$

$$m_y^{eq} = 0, \tag{69}$$

$$m_z^{eq} = 0. \tag{70}$$

In the works of d'Humieres et al. [37], the constants in Eqs. (42-56) are selected as $w_\varepsilon = 0$, $w_{\varepsilon j} = -475/63$ and $w_{xx} = 0$ for single-phase flows; however, in this work we follow the selection of Premnath and Abraham [38] used in their MRT LBM for multiphase flows where $w_\varepsilon = 3$, $w_{\varepsilon j} = -11/2$ and $w_{xx} = -1/2$.

The collision matrix in the moment space, $\hat{\Lambda}$, is given as

$$\widehat{\boldsymbol{\Lambda}} = diag[s_1, s_2, s_3, s_4, s_5, s_6, s_7, s_8, s_9, s_{10}, s_{11}, s_{12}, s_{13}, s_{14}, s_{15}, s_{16}, s_{17}, s_{18}]. \tag{71}$$

The diagonal elements are inverses of relaxation times for the distribution functions in the moment space, $\hat{f}_\alpha$, and they are used to relax the equilibrium distribution functions in the

moment space, $\hat{f}_\alpha^{eq}$. In this work, the diagonal elements are selected as a combination of the values reported by d'Humieres [37] and Premnath and Abraham [38] as

$$\widehat{\boldsymbol{\Lambda}} = diag\left[1, 1.19, 1.4, 0, 1.2, 0, 1.2, 0, 1.2, \frac{1}{\tau}, 1.4, \frac{1}{\tau}, 1.4, \frac{1}{\tau}, \frac{1}{\tau}, \frac{1}{\tau}, 1.98, 1.98, 1.98\right]. \quad (72)$$

The parameters s_{10}, s_{12} and $s_{14\text{-}16}$ are related to the single relaxation time, τ, in the single-relaxation-time LBM and are used to determine the viscosity, $\nu = \frac{1}{3}\left(\frac{1}{s_{10}}\right)$ and the Reynolds number, $Re = UD/\nu$.

As discussed in Lee and Lin [36], it is possible to compute the hydrodynamic variables of interest such as local density ρ, velocity $\boldsymbol{u}$, and pressure P, from f_α. This approach, however, is prone to numerical instabilities due to the steep density gradients involved in the computation of the source term $S_{\alpha\beta}$. Therefore, a separate distribution function g is introduced to compute pressure and momentum. We denote g in the lattice velocity direction α as g_α. A pressure function p is also defined, which varies smoothly across the interface. It is related to the actual pressure P through

$$p = P - \kappa\rho\frac{\partial^2\rho}{\partial x_k \partial x_k} + \frac{\kappa}{2}\frac{\partial\rho}{\partial x_k}\frac{\partial\rho}{\partial x_k}. \quad (73)$$

In the bulk phase, $p \cong P$ as density gradients are nearly zero. Use of p in the momentum equation increases the stability of the scheme at high density ratios. This definition of P and the choice of D in Eq. (13) are critical to the capability of the model to simulate high density ratios. Based on the definition of p in Eq. (39), Eq. (9) for F_i may be re-arranged as

$$F_i = \frac{\partial}{\partial x_j}(\rho c_s^2 - p)\delta_{ij} + \kappa\frac{\partial}{\partial x_j}\left(\frac{\partial\rho}{\partial x_k}\frac{\partial\rho}{\partial x_k}\delta_{ij} - \frac{\partial\rho}{\partial x_i}\frac{\partial\rho}{\partial x_j}\right). \quad (74)$$

However, within this framework of the MRT model, the pressure evolution equation must now be formulated to have a non-diagonal collision matrix.

To develop an evolution equation for pressure in moment space that is similar to Eq. (26), Lee and Lin proposed

$$\hat{g}_\alpha = \hat{f}_\alpha + \left(\frac{p}{c_s^2} - \rho\right)\hat{\Gamma}_\alpha(0)\,, \quad (75)$$

where

$$\hat{g}_\alpha = \mathrm{T}g_\alpha\,, \quad (76)$$

$$\Gamma_\alpha(\mathrm{u}) = \frac{f_\alpha^{eq}}{\rho}, \quad (77)$$

and

$$\hat{\Gamma}_\alpha(0) = \mathrm{T}\hat{\Gamma}_\alpha(0)\,. \quad (78)$$

From Eq. (41), the total derivative of $\hat{g}_\alpha$ can be written as

$$\frac{D\hat{g}_\alpha}{Dt} = \frac{D\hat{f}_\alpha}{Dt} + \frac{1}{c_s^2}\frac{Dp}{Dt}\hat{\Gamma}(0) - \frac{D\rho}{Dt}\hat{\Gamma}(0)\,, \tag{79}$$

which can be simplified to

$$\frac{D\hat{g}_\alpha}{Dt} = \hat{\Omega}_c + \hat{S}_{g\alpha} \tag{80}$$

where

$$\hat{S}_{g\alpha} = \mathrm{T}S_{g\alpha}\,, \tag{81}$$

$$\begin{aligned} &S_{g\alpha} \\ &= \frac{(e_{\alpha i} - u_i)\partial_i(\rho c_s^2 - p)}{c_s^2}(\Gamma_\alpha(u) - \Gamma_\alpha(0)) \\ &+ \frac{(e_{\alpha i} - u_i)\left[\kappa\partial_i(\partial_k\rho\partial_k\rho) - \kappa\partial_j\left(\partial_i\rho\partial_j\rho\right) + \rho\boldsymbol{g} - \rho K_w\boldsymbol{n}\right]}{c_s^2}\Gamma_\alpha(u), \end{aligned} \tag{82}$$

and

$$\hat{\Omega}_c = -\hat{\Lambda}_{\alpha\beta}\left(\hat{f}_\beta - \hat{f}_\beta^{eq}\right). \tag{83}$$

To express Eq. (49) as a function of $\hat{g}$ we define

$$\hat{g}_\alpha^{eq} = \hat{f}_\alpha^{eq} + \left(\frac{\rho}{c_s^2} - \rho\right)\hat{\Gamma}_\alpha(0)\,. \tag{84}$$

From this we get the following pressure evolution equation in moment space as

$$\frac{D\hat{g}_\alpha}{Dt} = -\hat{\Lambda}_{\alpha\beta}\left(\hat{g}_\beta - \hat{g}_\beta^{eq}\right) + \hat{S}_{g\alpha}\,, \tag{85}$$

The macroscopic properties of density, momentum and pressure are obtained from the following relations:

$$\rho = \sum_\alpha f_\alpha\,, \tag{86}$$

$$\begin{aligned} \rho u_i = \sum_\alpha e_\alpha g_\alpha + \kappa\frac{dt}{2}\left[\frac{\partial}{\partial x_i}\left(\frac{\partial\rho}{\partial x_k}\frac{\partial\rho}{\partial x_k}\right) - \frac{\partial}{\partial x_j}\left(\frac{\partial\rho}{\partial x_i}\frac{\partial\rho}{\partial x_j}\right)\right] \\ + \frac{dt}{2}\rho c_s^2(\boldsymbol{g} - K_w\boldsymbol{n}) \end{aligned} \tag{87}$$

$$p = c_s^2\sum_\alpha g_\alpha + u_i\frac{\partial\rho c_s^2}{\partial x_i}\frac{dt}{2} \tag{88}$$

Numerical Implementation

We implemented the algorithm in the 2D LBM MRT code to change the properties of the liquid phase modelled to be of non-Newtonian type in a gas-liquid multiphase system. The viscosity definition in LBM was modified to make the fluid behave in a way different than the linear Newtonian behaviour. Using the Generalized Newtonian Fluids representation [17], an effective viscosity value, μ^{Eff}, was defined to obtain shear-thinning or shear-thickening fluids represented by the Power Law ($\mu_{PL}^{Eff} = \mu_P\,|\dot{\gamma}|^{n-1}$, where μ_P is the flow consistency coefficient and n is the Power-law index) or the Bingham plastics ($\mu_{BH}^{Eff} = \mu_B + (1 - e^{-m|\dot{\gamma}|})\frac{\tau_B}{|\dot{\gamma}|}$, where μ_B is the plastic viscosity, τ_B is the Bingham yield stress and m is the stress growth exponent).

First, the viscosity definition of the LBM was changed to make the dynamic viscosity a function of the shear rate, $\gamma = \dot{2}\varepsilon$, where $\varepsilon_{\alpha\beta} = -\frac{1}{2\rho c_s^2 \delta t}\sum_{i=0}^{8} e_{i\alpha}e_{i\beta}\sum_{j=0}^{8}\widehat{\Lambda}\left[f_j - f_j^{eq}\right]$ in 2D MRT LBM. The double dot product of the strain rate tensor, ε, gives the following:

$$\varepsilon:\varepsilon = \mathrm{tr}\left\{\begin{pmatrix}\varepsilon_{11} & \varepsilon_{12}\\ \varepsilon_{21} & \varepsilon_{22}\end{pmatrix}\begin{pmatrix}\varepsilon_{11} & \varepsilon_{12}\\ \varepsilon_{21} & \varepsilon_{22}\end{pmatrix}\right\} = \mathrm{tr}\begin{Bmatrix}\varepsilon_{11}^2 + \varepsilon_{12}\varepsilon_{21} & \varepsilon_{21}\varepsilon_{11} + \varepsilon_{22}\varepsilon_{21}\\ \varepsilon_{11}\varepsilon_{12} + \varepsilon_{12}\varepsilon_{22} & \varepsilon_{22}^2 + \varepsilon_{21}\varepsilon_{12}\end{Bmatrix} \quad (89)$$

$$= \varepsilon_{11}^2 + \varepsilon_{22}^2 + 2(\varepsilon_{12}\varepsilon_{21})$$

For $\alpha = 1, \beta = 1, \varepsilon_{11}$ has:

$$\sum_{i=0}^{8} e_{i1}e_{i1} = e_{01}e_{01} + e_{11}e_{11} + e_{21}e_{21} + e_{31}e_{31} + e_{41}e_{41} + e_{51}e_{51} + e_{61}e_{61} + e_{71}e_{71} + e_{81}e_{81} =$$

$$(0)(0) + (1)(1) + (0)(0) + (-1)(-1) + (0)(0) + (1)(1) + (-1)(-1) + (-1)(-1) + (1)(1) = 6 \quad (90)$$

For $\alpha = 1, \beta = 2, \varepsilon_{12}$ has:

$$\sum_{i=0}^{8} e_{i1}e_{i2} = e_{01}e_{02} + e_{11}e_{12} + e_{21}e_{22} + e_{31}e_{32} + e_{41}e_{42} + e_{51}e_{52} + e_{61}e_{62} + e_{71}e_{72} + e_{81}e_{82} =$$

$$(0)(0) + (1)(0) + (0)(1) + (-1)(0) + (0)(-1) + (1)(1) + (-1)(1) + (-1)(-1) + (1)(-1) = 0 \quad (91)$$

For $\alpha = 2, \beta = 1, \varepsilon_{21}$ has:

$$\sum_{i=0}^{8} e_{i2}e_{i1} = e_{02}e_{01} + e_{12}e_{11} + e_{22}e_{21} + e_{32}e_{31} + e_{42}e_{41} + e_{52}e_{51} + e_{62}e_{61} + e_{72}e_{71} + e_{82}e_{81} =$$

$$(0)(0) + (0)(1) + (0)(0) + (0)(-1) + (-1)(0) + (1)(1) + (1)(-1) + (-1)(-1) + (-1)(1) = 0 \quad (92)$$

For $\alpha = 2, \beta = 2, \varepsilon_{22}$ has:

$$\sum_{i=0}^{8} e_{i2}e_{i2} = e_{02}e_{02} + e_{12}e_{12} + e_{22}e_{22} + e_{32}e_{32} + e_{42}e_{42} + e_{52}e_{52} + e_{62}e_{62} + e_{72}e_{72} + e_{82}e_{82} =$$

$$(0)(0) + (0)(0) + (1)(1) + (0)(0) + (-1)(-1) + (1)(1) + (1)(1) + (-1)(-1) + (-1)(-1) = 6 \quad (93)$$

This gives

$$|\dot{\gamma}| = \sqrt{2(\varepsilon_{11}^2 + \varepsilon_{22}^2 + 2(0))} = \sqrt{4\varepsilon_{11}^2} = 2\varepsilon_{11} = -\frac{1}{\rho c_s^2 \delta t} 6 \sum_{j=0}^{8} \widehat{\Lambda} \left[f_j - f_j^{eq} \right] \quad (94)$$

The effective viscosity for Power-law fluids using the above definition of $|\dot{\gamma}|$ for the required fluid type becomes $\mu_{eff} = \mu_P |\dot{\gamma}|^{n-1}$. When n<1, this relation results in a shear-thinning fluid, while for n>1, we obtain a shear-thickening one and n=0 corresponds to a Newtonian fluid. This effective viscosity definition gives us a shear stress definition for Power-law fluids as: $\mu = \mu_P |\dot{\gamma}|^{n-1} \dot{\gamma}$.

For the case of a Bingham plastic, the definition for effective viscosity becomes $\mu_{eff} = \mu_B + \left(1 - e^{-m|\dot{\gamma}|}\right) \frac{\tau_B}{|\dot{\gamma}|}$. When τ_B=0, the Newtonian fluid is obtained. This effective viscosity definition results in the shear stress definition for Bingham plastics given as:

$$\begin{cases} \tau = \frac{\tau_B}{|\dot{\gamma}|} + \mu_B, & |\tau| > \tau_B, \\ \dot{\gamma} = 0, & |\tau| < \tau_B, \end{cases} \quad (95)$$

where τ_B is the Bingham yield stress.

The effective viscosity was related to the relaxation parameter using the definition of viscosity in the Lee-Lin approach, $\mu_H = \rho_H \tau_H / 3$, where ρ_H is the density of the heavy fluid and τ_H is the relaxation parameter for the heavy fluid. If this is replaced in the equation for effective viscosity, we obtain:

$$\tau_{Eff} = \tau_H + \left(1 - e^{-m|\dot{\gamma}|}\right) \frac{3\tau_B}{\rho_H |\dot{\gamma}|}. \quad (96)$$

Once the relaxation parameter was calculated then the relaxation factor s7 was obtained using the relation, $\tau = \left(\frac{1}{s_7}\right)$.

Extrapolation method in LBM for inflow boundary conditions

We implemented the extrapolation algorithm in the 2D LBM MRT code to assign velocity values for an open boundary where flow is injected into a domain with fluid of non-Newtonian type in a gas-liquid multiphase system.

In the extrapolation method, the value of the distribution function on the layer outside the boundary is determined by using the values on the boundary and the first interior layer. For example, the distribution function on the layer below the bottom boundary is given by

$$f_{temp}(k, i+1, j) = 2 f_{temp}(k, i, j) - f_{temp}(k, i-1, j), \quad (97)$$

where f_{temp} is the value of the distribution function at each lattice node after the collision calculation and before streaming (Figure 42). In order to simulate open boundary conditions, no further information is needed because the macroscopic properties are determined by the moments of the distribution function. However, to enforce other boundary conditions the values of density or the velocity component(s) at the boundary node are set just prior to calculating the equilibrium distribution function.

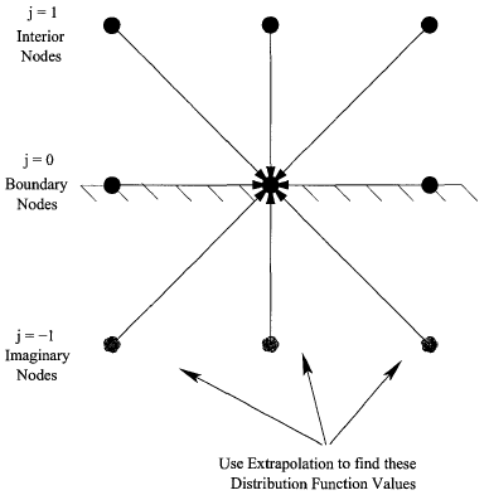

Figure 42. Schematic showing the implementation of extrapolation.

RESULTS

In the first numerical test case presented here, we compared the behavior of a single bubble rising in a vertical liquid column in a closed 2D domain where the surrounding fluid selected to be Newtonian type and as Bingham plastic. To obtain the Newtonian fluid we ignored the additional term in the definition of the τ_{Eff} and basically left it to be equal to τ_H. In the case of the Bingham plastic, the values m and τ_B are assigned to be non-zero. Figure 43 to Figure 46 shows the time evolution of the shape of a circular bubble placed in a Newtonian (left) and the non-Newtonian (right) fluid starting from rest. The bubble attains a more elongated shape in the Bingham plastic (m=0.0001 and $\tau_B = 200$) as compared to the Newtonian fluid. Figure 47 shows that the bubble in the Bingham plastic experiences a delay in acceleration as compared to the Newtonian fluid and later on the velocity values become comparable in both fluids when the velocity is plotted with respect to a non-dimensional time (t*).

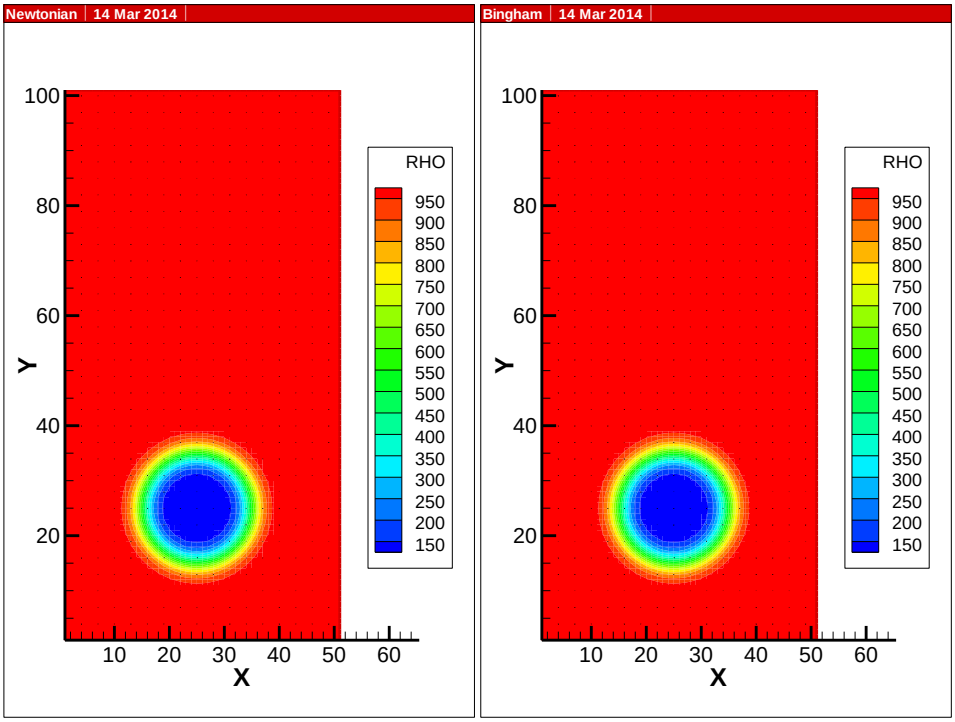

Figure 43. Bubble rising in a Newtonian and a non-Newtonian fluid at t=0.

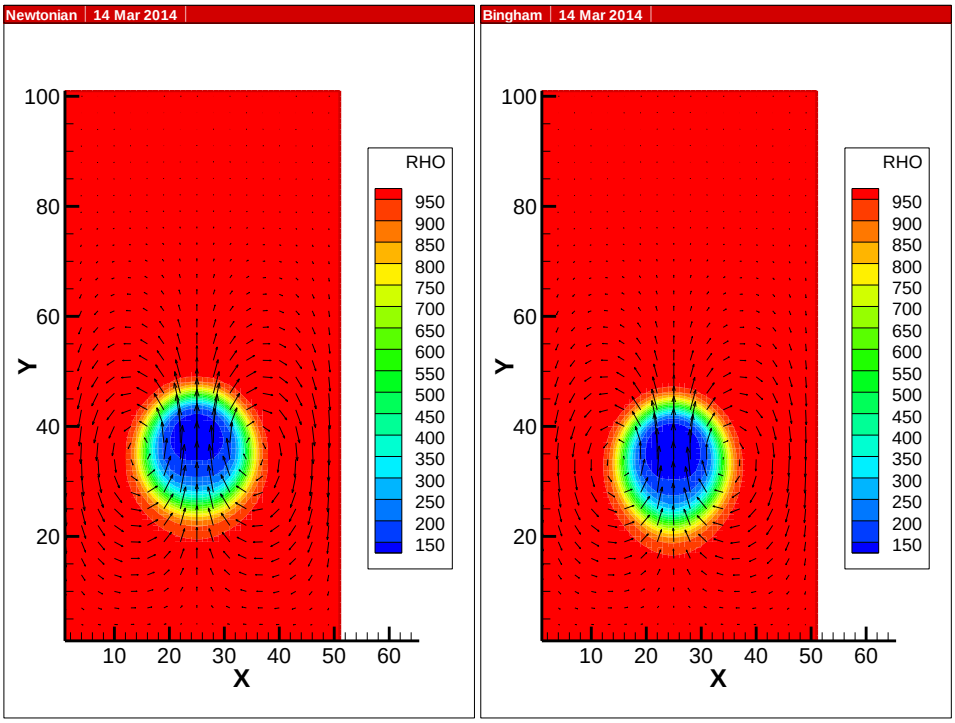

Figure 44. Bubble rising in a Newtonian and a non-Newtonian fluid at t=5,000.

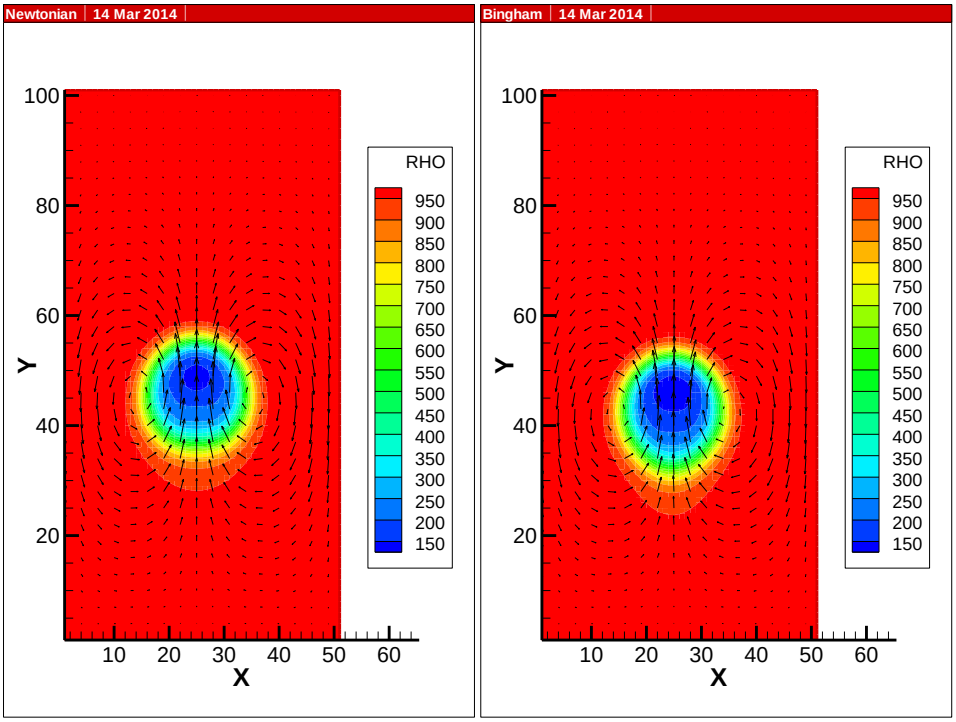

Figure 45. Bubble rising in a Newtonian and a non-Newtonian fluid at t=10,000.

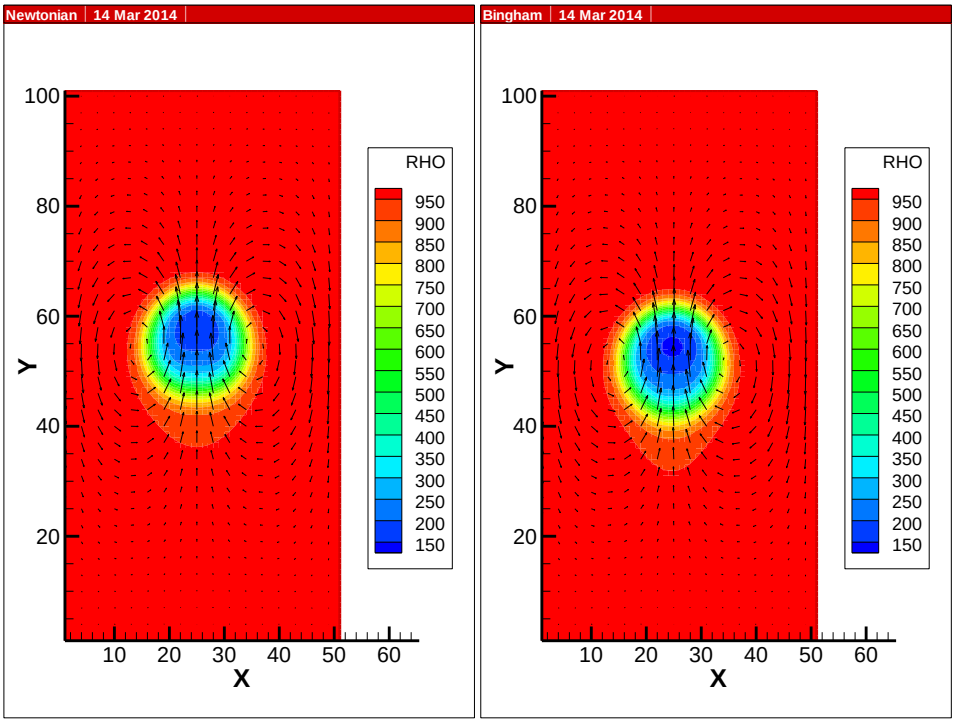

Figure 46. Bubble rising in a Newtonian and a non-Newtonian fluid at t=15,000.

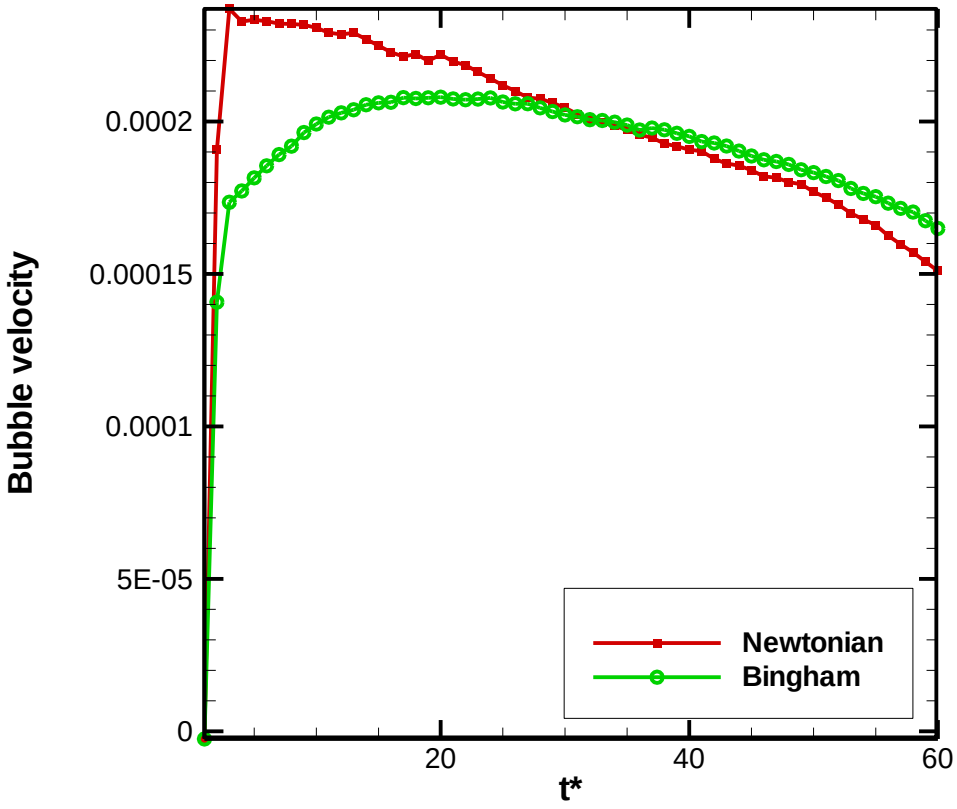

Figure 47. Comparison of bubble rise velocity in a Newtonian and a non-Newtonian fluid.

Secondly, a flow injection case was created by adjusting the values of the f and g distribution functions before the streaming step according to the inlet velocity and density values. The figure below shows such an example where a portion of the left boundary (40<y<60) has been designated as the inflow boundary where the fluid injection occurs. A velocity value of 0.001 has been assigned. The initial condition for the flow field was set for a stationary circular bubble located at the center of the domain. As a result of the injection process, the bubble is dislocated towards the right at the speed induced by the inflow boundary condition. The right side of the domain has a portion designated to be the outflow boundary condition where the injected fluids exit the domain.

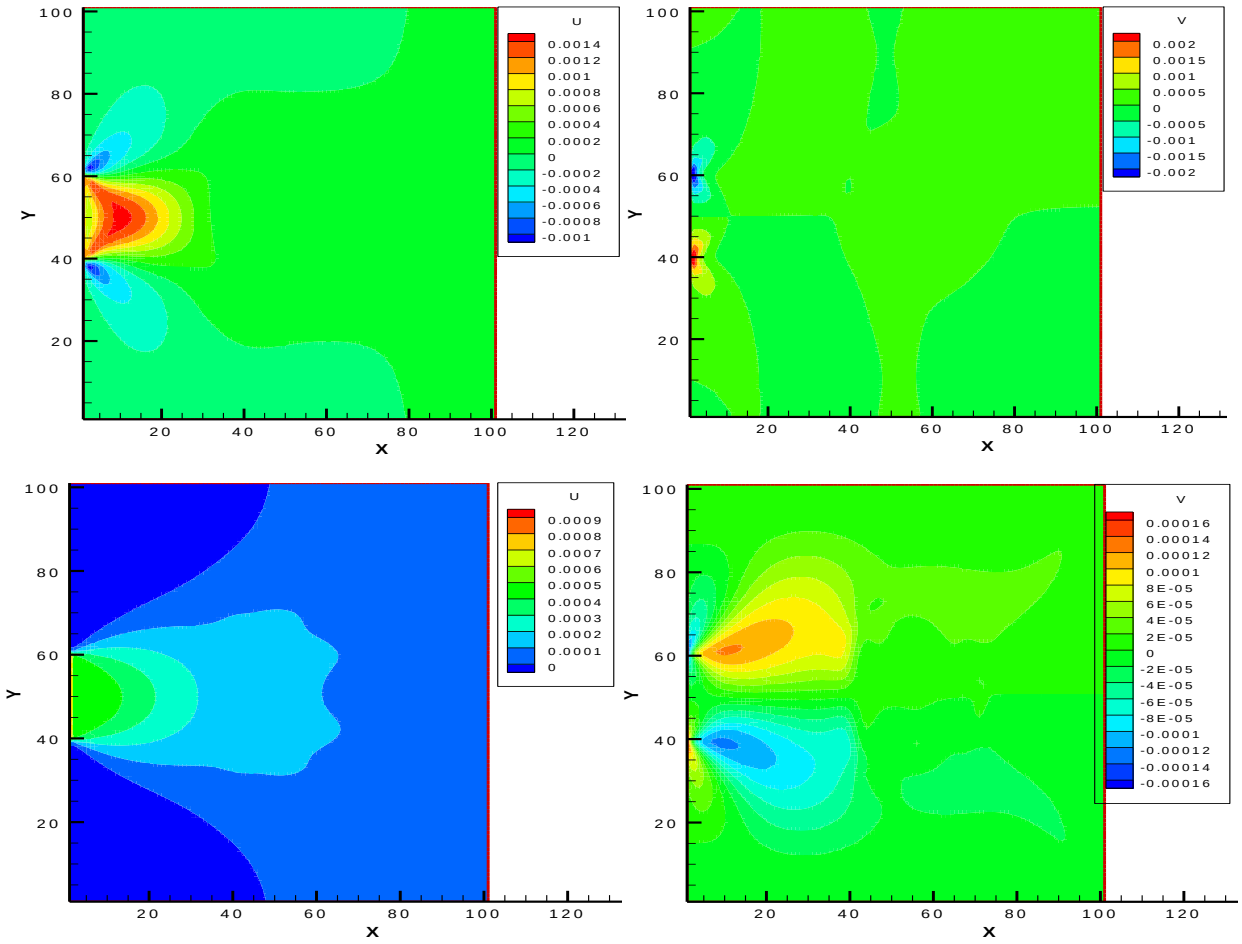

Figure 48. Contours of horizontal and vertical velocity components in a square domain caused by injection at the left boundary in a Newtonian fluid (top row) and a Bingham plastic (bottom row).

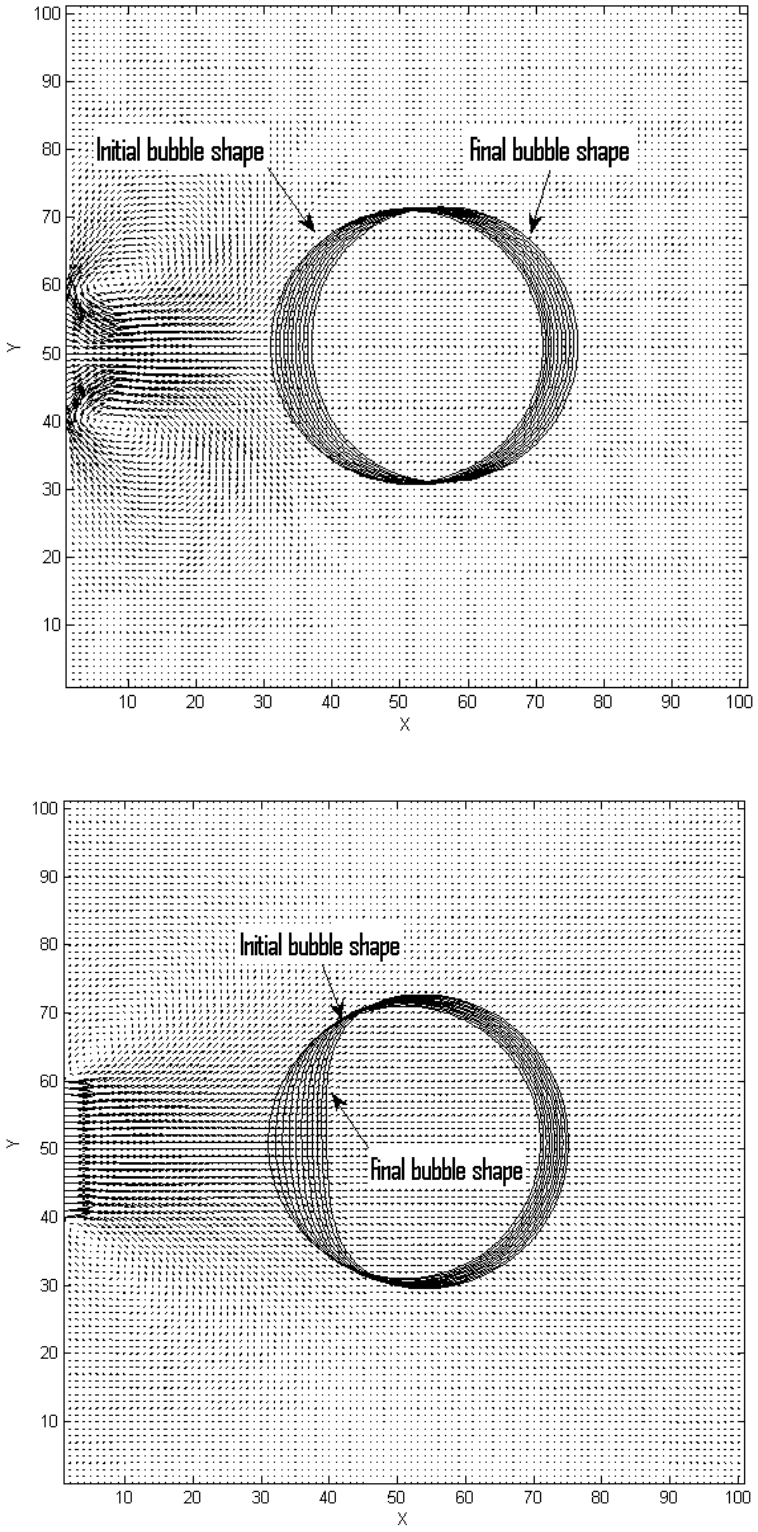

Figure 49. Bubble interface displacement from initial to final state caused by the injection at the left boundary in a Newtonian fluid (top figure) and Bingham plastic (bottom figure).

The above figures show that the circular bubble shape is maintained in the Newtonian flow case where the displacement of the interface in the high speed and low speed zones are the same due

to constant viscosity; however, in the Bingham plastic case, the deformation of the bubble in the high speed zone is larger as compared to the low speed zone since the viscosity is lower in this area caused by the increased shear stress in the area near the injection due to high velocities. This study exemplifies the challenges in mobilizing bubbles in nuclear waste sludge that exhibit Bingham plastic behavior due to the differences in the fluid characteristics.

Later, two separate simulations were created with the same geometry, flow conditions and solver settings except that the viscosity definition for the main phase was set to Newtonian fluid for case 1 and a non-Newtonian fluid in case 2 in a rectangular domain of size 51 X 101 in lu (lattice units). A portion of the left boundary (20<y<30) has been designated as the inflow boundary where the fluid injection occurs at an inlet velocity of u=3x10-3 lu/ts, which corresponds to a Reynolds number of 9 for the Newtonian case. The initial condition for the flow field was set for 6 stationary circular bubbles dispersed randomly inside the domain (Figure 50).

As a result of the injection process, the fluid inside the container starts mixing and the bubbles are dislocated at the local flow speed induced by the inflow boundary condition. The right side of the domain has a portion designated to be the outflow boundary condition where the injected fluids exit the domain. Figure 51 shows the time change of the density distribution of the container in both cases at the same time intervals. It was observed that the flow pattern induced by the incoming laminar jet has created a vastly different mixing scenario in case 2 with the Bingham plastic material. Our simulations are indicative that CFD can be utilized as a predictive tool to identify the changes in the performance of pulsed-jet mixers in nuclear waste tanks when the injections occur in the supernate layer where the fluid characteristics are similar to a Newtonian fluid as compared to the slurry layer where a Bingham plastic type of sludge material is expected to exist. Future work in this task will be to extend the simulations to 3D and investigate the capability to incorporate turbulence effects.

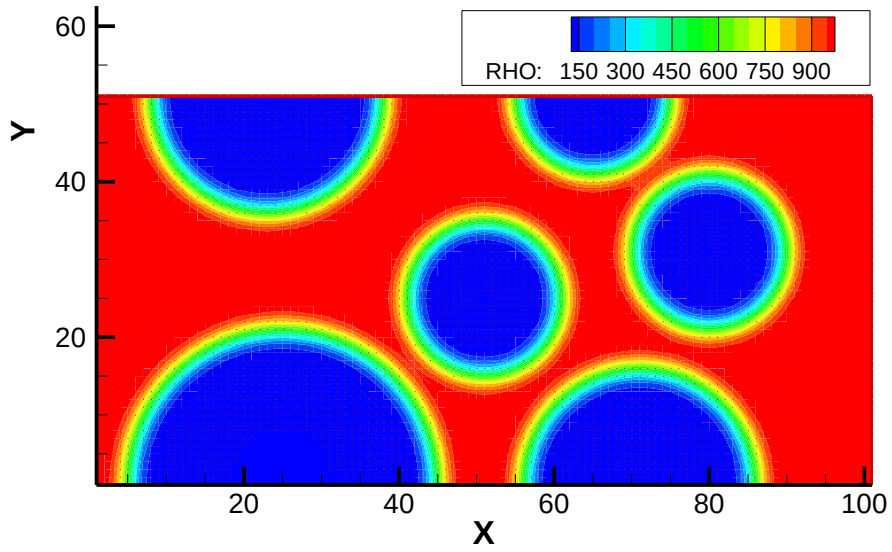

Figure 50. Initial condition in the container with a gas phase (represented in blue) dispersed in a liquid phase (represented in red) where the density ratio is 10.

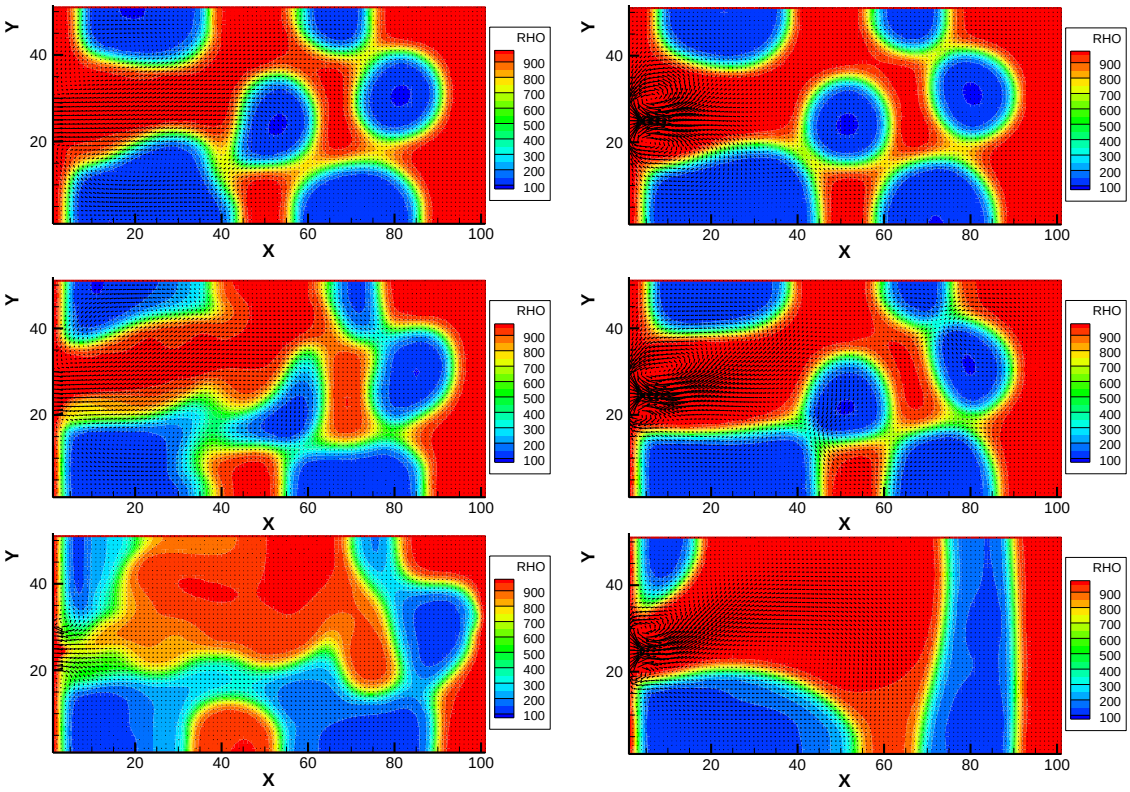

Figure 51. Bubble interface displacement at t=5000, 10,000 and 20,000 in a Newtonian fluid (right column) and Bingham plastic (left column).

CONCLUSIONS

In this work, we presented a concise literature review on modeling turbulent flows and non-Newtonian flows with LBM. Our study revealed that the extension of lattice Boltzmann method for the simulation of complex fluid flows including turbulent flows and non-Newtonian fluids is possible via various approaches, although a well-established method has not yet been achieved. In comparison to the turbulence models proposed for LBM, the incorporation of non-Newtonian fluid properties in the LBM simulations have been presented more consistently. The LES-LBE applications show more promise in terms of turbulence modeling with LBM due to its simpler implementation and higher accuracy over two-equation models. It should be noted that the authors were not able to find an application of LBM for turbulent flows in a multiphase flow configuration; therefore, the future LBM task at FIU that aims to simulate turbulent flows in nuclear tanks with multiple phases of fluids would be a challenging and a scientifically important effort, especially if both of the subgrid models and Bingham plastic effects could be incorporated simultaneously in the viscosity definition of the lattice Boltzmann equation.

The formulation of a multiple relaxation time LBM based on the Lee and Lin multiphase model was presented for dynamic bubbles and droplets in three dimensional domains with complex geometries and under the effect of wall adhesion and gravitational forces. Numerical cases of moving bubbles and droplets in confined and open computational domains have been presented and the capability of the method to simulate dynamic interface tracking of the fluid interface in contact with the solid surfaces has been shown. The numerical method based on a multiphase LBM established with this research effort was able to provide promising preliminary results for a case that represents similar piping features of a DOE nuclear waste tank. However, further improvement of the method needs to be performed with appropriate inlet and outlet boundary conditions to simulate flows with injections and mixing of fluids.

Future work will include implementation of a turbulence model for injection type flows as well as modifying the viscosity definition in LBM to simulate non-Newtonian fluids. The LES-LBM will be the approach to follow for the turbulent flow simulations with LBM; however, the cascade-LBM will also be investigated if time permits which claims to not necessitate a separate turbulence model within the LBM framework. The extension of the LBM code to non-Newtonian flow modeling will also be conducted in the next fiscal year, especially related to Bingham plastic fluids that are found in the DOE waste tanks.

FIU will continue to implement the non-Newtonian models for Bingham plastics and other fluids that can be described as Power-law fluids using the 2D and 3D LBM codes. The 2D cases will also be verified against stratified flows in channels using the analytical equations available for the velocity profile. The final task to accomplish will be to change the boundary conditions in the LBM codes to allow simulation of gas injections in liquid domains.

REFERENCES

1. Gauglitz, P A., Mechanisms of Gas Bubble Retention and Release: Results for Hanford Waste Tanks 241 S 102 and 241 SY 103 and Single Shell Tank Simulants. Richland, WA : Pacific Northwest National Laboratory, 1996. PNNL-11298.
2. Russell, R. L., Final Report: Gas Retention and Release in Hybrid Pulse Jet Mixed Tanks Containing Non-Newtonian Waste Simulants, 2005, WTP-RPT-114.
3. Meyer, P. A., Overview of the Pulse Jet Mixer Non-Newtonian Scaled Test Program, 2005, WTP-RPT-127.
4. Gauglitz, P A.,The Role of Cohesive Particle Interactions on Solids Uniformity and Mobilization During Jet Mixing: Test Recommendations. Richland, WA : Pacific Northwest National Laboratory, 2010. PNNL-19245.
5. Poloski, A. P., Technical Basis for Scaling of Air Sparging Systems for Mixing in Non-Newtonian Slurries, 2005, WTP-RPT-129.
6. Aharonov, E and Rothman, D H. Non-Newtonian Flow (Through Porous Media):A Lattice-Boltzmann Method. 1993, Geophysical Research Letters, Vol. 20, pp. 679-682.
7. Gabbanelli, S, Drazer, G and Koplik, J. Lattice Boltzmann method for non-Newtonian (power-law) fluids. 2005, Physical Rewview E, Vol. 72, pp. 046312-1.
8. Boyd, J, Buick, J and Green, S. A second-order accurate lattice Boltzmann non-Newtonian flow model. 2006, Journal of Physics A: Mathematical and General, Vol. 39, pp. 14241-14247.
9. Tang, G H, Li, X. F., He, Y.L, Tao, W. Q. Electroosmotic flow of non-Newtonian fluid in microchannels. 2009, Journal of Non-Newtonian Fluid Mechanics, Vol. 157, pp. 133-137.
10. Yoshino, M., Hotta, Y., Hirozane, T., Endo, M. A numerical method for incompressible non-Newtonian fluid flows based on the lattice Boltzmann method. 2007, J. Non-Newtonian Fluid Mechanics, Vol. 147, pp. 69-78.
11. Papanastasiou, T C. Flows of Materials with Yield. 1987, Journal of Rheology, Vol. 31, pp. 385-405.
12. Wang, C-H and Ho, J-R. Lattice Boltzmann modeling of Bingham plastics. 2008, Physica A, Vol. 387, pp. 4740-4748.
13. Tang, G H, Wang, S. B., Ye, P. X., Tao, W. Q. Bingham fluid simulation with the incompressible lattice Boltzmann model. 2011, Journal of Non-Newtonian Fluid Mechanics, Vol. 166, pp. 145-151.
14. Leonardi, C. R. Numerical Rheometry of Bulk Materials Using a Power Law Fluid and the Lattice Boltzmann Method. Journal of Non-Newtonian Fluid Mechanics, 2011, Vol. 166., 12-13, pp. 628-38.
15. Vikhansky, A. "Lattice-Boltzmann Method for Yield-stress Liquids." Journal of Non-Newtonian Fluid Mechanics 155.3 (2008): 95-100.

16. Chai, Z, Shi, B., Guo, Z., Rong, F. Multiple-relaxation-time lattice Boltzmann model for generalized Newtonian fluid flows. 2011, Journal of Non-Newtonian Fluid Mechanics, Vol. 166, pp. 332-342.
17. Frank, Xavier, and Huai Z. Li. Complex Flow around a Bubble Rising in a Non-Newtonian Fluid. Physical Review E, 2005, Vol.71, 3.

TASK 18.1 FY13 YEAR END TECHNICAL REPORT Evaluation of FIU's Solid-Liquid Interface Monitor for Rapid Measurement of HLW Solids on Tank Bottoms

EXECUTIVE SUMMARY

For this subtask, FIU's solid-liquid interface monitor (SLIM) is being evaluated for its future use in Hanford high-level radioactive waste (HLW) mixing tanks. The waste processing operations need to ensure that mixing by pulse-jet mixers (PJMs) is thorough and that solids are completely suspended and removed with each batch. Therefore, a technology that could see through the turbulent liquid and entrained solids during mixing and verify that no solids remained on the floor would allow operators to know that the waste was completely suspended and able to be transferred out of the tank for further processing.

FIU successfully demonstrated the bench-scale testing, proof of concept, for the application of SLIM in mixing tanks for short imaging periods (< 1 minute). A milestone report was submitted to DOE EM in April 2014 that contained the research and technology testing results. With proof of concept testing successful, FIU next developed a Phase II Test Plan and sent it to DOE EM and Hanford for comments. FIU continued to develop new data filters and to improve those developed earlier for SLIM. A 3-D sonar imaging software has been developed and is being refined. The built-in commercial sonar imaging software does not function with sparse sonar data sets such as those generated in times less than 1 minute.

The goal of Phase II testing of SLIM is to verify that the technology will meet all functional requirements for a technology deployment into a high-level radioactive waste mixing tank. The functional requirements will include data quality objectives for the accuracy, speed and other performance requirements for SLIM components (i.e., mechanical deployment system, sonar and software systems). The functional requirements will also include safety analyses, deployment and operating procedures, and other requirements needed for any technology deployed in HLW at Hanford. As Phase II testing progresses, it is expected that additional tests will be requested by Hanford engineers. Additional successful testing will improve SLIM's likelihood of deployment in 2016 and will address engineering safety and other concerns in the deployment and operation of the system. Phase II testing will be completed in April 2015. Phase III would follow complete analysis of all results from Phase II and after DOE Hanford Site engineers develop a complete set of functional requirements for deployment into a specific HLW mixing tank. During 2015, it is envisioned that an actual Hanford HLW mixing tank will be identified that would benefit from the deployment of the SLIM technology in 2016.

INTRODUCTION

FIU's Solid-Liquid Interface Monitor (SLIM) is being tested and developed to meet a technology need for Hanford high-level radioactive waste (HLW) mixing tanks. The waste processing operations need to ensure that mixing by pulse-jet mixers (PJMs) is thorough and that solids are completely suspended and removed with each batch. Therefore, there is a need for a technology that can image or sense through the turbulent liquid and entrained solids during mixing and verify that no solids remained on the floor. This would allow operators to know that the waste was completely suspended and able to be transferred out of the tank for further processing.

In the 2003-2008 timeframe FIU developed, tested and qualified SLIM for deployment in Hanford's 1 million gallon, HLW storage tanks (single-shell tanks (SSTs) and double-shelled tanks (DSTs)). FIU testing met all of the numerous performance requirements and the functional requirements for deploying into these tanks. Importantly, SLIM showed that it could image solids on the tank floor even while vigorous mixing entrained as much as 30% solids into the tank liquid. This is the reason for the interest in SLIM for this new HLW processing application. This entirely new application of SLIM for mixing tanks involves much smaller tanks, more vigorous mixing, and a much shorter time allotted for imaging the settled solids layer on the tank floor. New software and new strategies have been developed to quickly and effectively visualize solids on the tank floor. FIU's SLIM consists of 3 primary components: (1) a commercial, customized sonar that is radiation hardened and impervious to highly caustic (pH>14) solutions; (2) a deployment platform able to deploy into DSTs and SSTs via 8-inch risers in the tank dome top; and (3) software for filtering sonar data and displaying an image of the solids settled across the entire floor of HLW tanks.

This subtask was initiated in mid-October 2013 and so this report details progress made over 7 months. The technical approach is to focus on the sonar and image processing algorithms and software and testing at the bench-scale and then the pilot-scale this year with the goal of deploying SLIM in 2016 should all testing succeed and Hanford HLW managers agree that the system meets their needs and funds are available to deploy the technology in 2016.

Technical Approach:

1. Develop bench-scale test plan to demonstrate proof of principle for rapid sonar imaging. Set up test bed and optimize the sonar image for times less than 60 seconds with sonar settings (total view angle, angle between sonar pings along a 2-D scan, angle of rotation between each 2-D scan). Demonstrate that sonar imaging is sufficient for 15 – 60 second scan times and then optimize imaging for these short scans.
2. Develop improved software to image tank floors, walls and solids on the floor (commercial sonar imaging software does not generate images for short time scans with limited data). Develop improved image processing filters. Develop a test plan for the pilot-scale testing of the sonar with up to 30% solids entrained in the liquid to test imaging during vigorous mixing similar to PJM mixing in Hanford tanks.

RESULTS

Bench-Scale Testing: The testbed setup includes the 3-D sonar mounted inside of a tank with dimensions of 72 inches in height and 35.5 inches in diameter. A brick and other objects with specific shapes were selected for test objects to evaluate the accuracy of images with short time (15 – 60 seconds) scans by the sonar. FIU developed and applied filtering algorithms to remove points shown beyond the tank boundaries resulting from occasional sonar pings that have been scattered twice. Additional filtering algorithms smooth out the image contour of the walls and the settled solids layer surface. For later testing of the sonar during mixing, FIU developed an imaging algorithm that has an option to display the numerous sonar pings reflected off the entrained solids and back to the sonar or to eliminate all these reflections and only display the floor, wall and settled solids layer. The 3-D sonar operating software settings include: view angle (30°-180°); angle between successive sonar pings along every 2-D sonar scan (.9°-9.0°); and finally the angle between 2 successive 2-D scans can also be set at one of the same 10 options (0.9°-9.0°).

Primary sonar settings for optimizing image quality include:

- **View Angle or Swath Arc:** The arc swept by the sonar as it gathers the data can be set in 30 degree increments. The limits of the data capture area are shown in the Swath View window to aid in setting the system for optimum coverage.
- **Swath Step Size:** The Swath Step Size specifies how many discrete 0.9° tilt motor steps are performed for each "ping" of the sonar. For the finest detail, the Swath Step Size should be set to 1, but by increasing this setting the scan speed may be increased and the dataset size reduced. The swath step size can be set at 1 to 10.
- **Rotation Step Size:** The Rotation Step Size sets how many discrete 0.9° rotation motor steps are performed after each 2-D swath. For the finest detail, the Rotation Step Size is set to 1. The rotation step size can be set at 1 to 10.

Table 7 below lists the 3 angle related sonar operation settings. Settings not listed include: maximum range, stop depth, start depth, detection threshold %, filter window, transmit pulse width, velocity of sound for liquid, sample delay, sample interval, number of samples.

Table 7. Select Sonar Settings to Optimize Image Resolution

View Angle or Swath Arc Options	Swath Step Size Setting: Angle between successive pings along each 2-D Swath	Rotation Step Size Setting: Angle between successive 2-D scans
30°	1 : 0.9°	1 : 0.9°
60°	2 : 1.8°	2 : 1.8°
90°	3 : 2.7°	3 : 2.7°
120°	4 : 3.6°	4 : 3.6°
150°	5 : 4.5°	5 : 4.5°
180°	6 : 5.4°	6 : 5.4°
	7 : 6.3°	7 : 6.3°
	8 : 7.2°	8 : 7.2°

	9 : 8.1°	9 : 8.1°
	10: 9°	10: 9°

The initial optimization testing created sonar images for a range of viewing angles, 2-D swath step sizes and rotation step sizes. Image resolution was calculated from sonar data collected along with the time for each sonar scan. Based upon depth and accuracy of the depth of the settled solids layer, an estimate of the volume of the settled solids and the accuracy of that estimate was calculated.

Table 8 and Table 9 below show some of the parameters varied and their effect on the time required to complete the sonar scan. All values are settings except time to scan which is measured.

Table 8. Numerical Index of Time Trials at 180° View Angle with Sonar Settings

(Alternating Swath Motor Step Size and Rotate Motor Step Size for a 360° Scan).

Trial		**1**	**2**	**3**	**4**	**5**	**6**
Time		~12 min 26 sec	~2 min 49 sec	~1 min 31 sec	~44 sec	~2 min 37 sec	~7 min 5 sec
Swath Motor Step Size		1	3	5	10	1	5
Rotate Motor Step Size		1	3	5	10	5	1
Range Parameters	**Maximum Range (Test Tank Dia.)**	1 meter	1 meter	1 meter	1 meter	1 meter	1 meter
	Start Depth (meters)	0.4	0.4	0.4	0.4	0.4	0.4
	Stop Depth (meters)	1	1	1	1	1	1
Detection Threshold (%)		80	80	80	80	80	80
Filter Window		50	50	50	50	50	50
T_x Pulse(Transmit Pulse)(µsec)		20	20	20	20	20	20
Velocity of Sound (meters/seconds)		1500	1500	1500	1500	1500	1500
Sample Delay (µsec)		533	533	533	533	533	533
Sample Interval (µsec)		1	1	1	1	1	1
Number of Samples		800	800	800	800	800	800

Table 9. Index of Time Trials with Sonar Settings

(Alternating Swath Arc; highest resolution settings for a 360° scan).

Trial		**1**	**2**	**3**	**4**	**5**
Swath Arc		30°	60°	90°	120°	150°
Time		~1 min 55 sec	~3 min 33 sec	~5 min 48 sec	~7 min 40 sec	~9 min 4 sec
Swath Motor Step Size		1	1	1	1	1
Rotate Motor Step Size		1	1	1	1	1
Range Parameters	**Max Range (Test Tank Dia.)**	1 meter	1 meter	1 meter	1 meter	1 meter
	Start Depth (meters)	0.6	0.6	0.6	0.6	0.6
	Stop Depth (meters)	1	1	1	1	1

Detection Threshold (%)				50	50	50	50	50
Filter Window				25	25	25	25	25
T_x Pulse(Transmit Pulse)(µsec)				10	10	10	10	10
Velocity of Sound (meters/seconds)				1500	1500	1500	1500	1500
Sample Delay (µsec)				533	533	533	533	533
Sample Interval (µsec)				1	1	1	1	1
Number of Samples	800	800	800	800	800			

Results for trials 1 and 4 (highest resolution image settings, see Table 10 & Figure 52 and Table 11 & Figure 53) and trial 2 (lowest resolution, see Table 12 & Figure 54) are shown below including sonar images. It was found that decreasing the swath angle can greatly reduce the time required to acquire a single sonar scan. Also, to reduce noise, the transmit pulse duration should be shortened.

Table 10. Trial #1 Sonar Settings

INDEX OF TIME TRIALS (Alternating Swath Arc) (Highest Resolution settings for a 360° scan)		
Trial		1
Swath Arc		60°
Time		~3 min 50 sec
Swath Motor Step Size		1
Rotate Motor Step Size		1
Range Parameters	**Max Range (Test Tank Diameter)**	1 meter
	Start Depth (meters)	0.4
	Stop Depth (meters)	0.8
Detection Threshold (%)		60
Filter Window		35
T_x Pulse (Transmit Pulse) (µsec)		10
Velocity of Sound (meters/seconds)		1500
Sample Delay (µsec)		533
Sample Interval (µsec)		1
Number of Samples		800

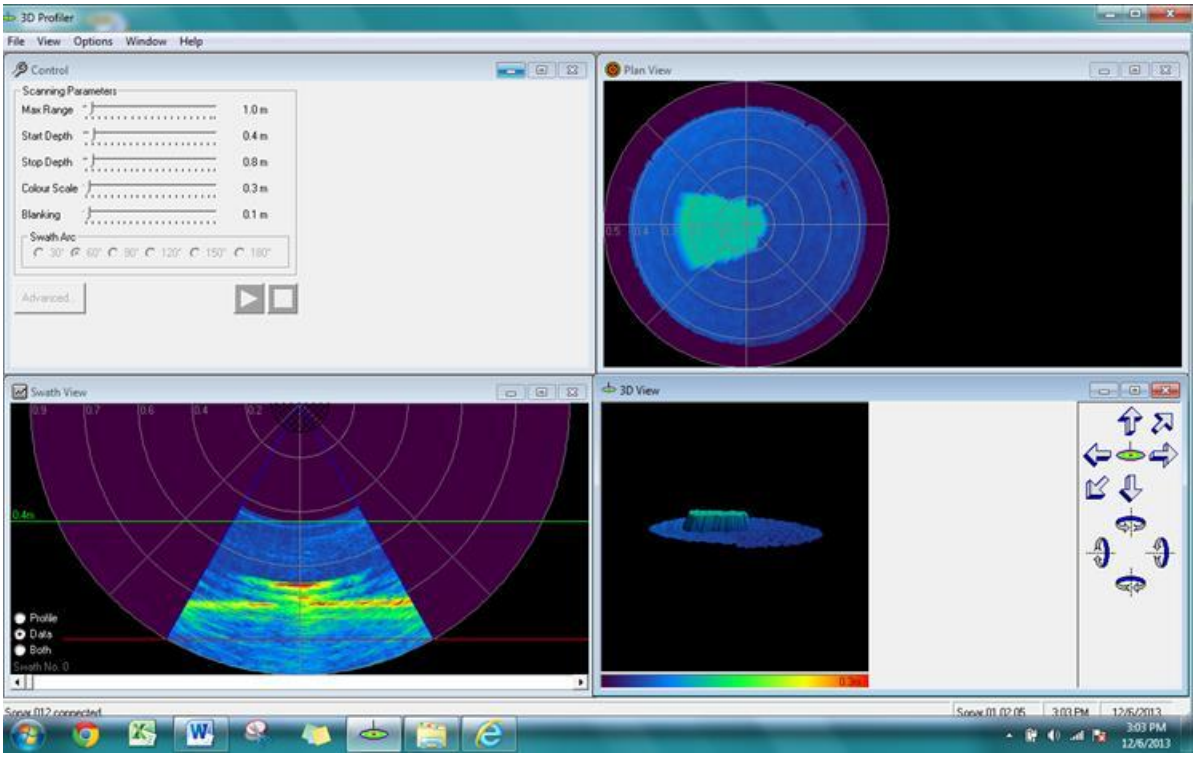

Figure 52. Image of a solid brick on the bottom of a 1-meter diameter tank in tap water.

Table 11. Trial #4 Sonar Settings

INDEX OF TIME TRIALS (Alternating Swath Arc) (Best quality settings for a 360° scan)		
Trial		**4**
Swath Arc		180°
Time		~12 min 26 sec
Swath Motor Step Size		1
Rotate Motor Step Size		1
Range Parameters	**Max Range(Test Tank Diameter)**	0.8 meter
	Start Depth(meters)	0.6
	Stop Depth(meters)	0.8
Detection Threshold (%)		50
Filter Window		35
T_x Pulse(Transmit Pulse)(µsec)		20
Velocity of Sound(meters/seconds)		1500
Sample Delay(µsec)		533
Sample Interval(µsec)		1
Number of Samples		800

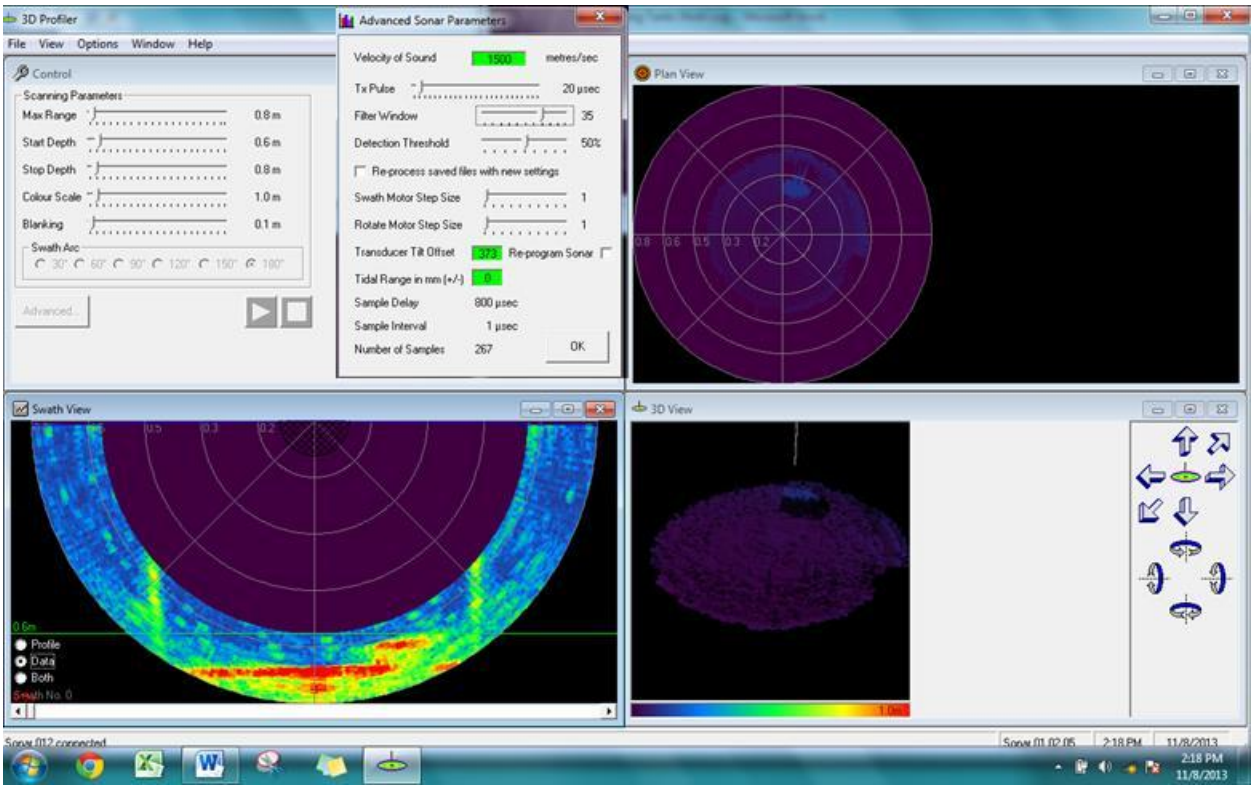

Figure 53. Test of the image resolution of 3-D sonar image from a single scan.

Trial 2, shown next, was intended to determine if the sonar built in imaging is able to image a brick at its lowest resolution settings. Indeed, as predicted, lack of sonar data collected rendered the commercial sonar image profiler unable to image with its 3D profiler. To correct this issue, one could increase the Rotate Motor Step Size to a higher resolution setting but this will increase the amount of time needed to complete the sonar scan beyond the 15-60 seconds needed. Due to this need for rapid sonar imaging, FIU has input the sonar data into open source imaging tools as well as ones developed on this subtask to generate images and ascertain their quality and utility in monitoring the presence of solids on tanks floors during mixing.

Table 12. Trial #2 Sonar Settings

INDEX OF TIME TRIALS (Alternating Swath Arc) (Best quality settings for a 360° scan)		
Trial		**2**
Swath Arc		30°
Time		~19 sec
Swath Motor Step Size		5
Rotate Motor Step Size		5
Range Parameters	**Max Range(Test Tank Diameter)**	1 meter
	Start Depth(meters)	0.4
	Stop Depth(meters)	0.8
Detection Threshold (%)		90

Filter Window	25
T_x Pulse(Transmit Pulse)(µsec)	10
Velocity of Sound(meters/seconds)	1500
Sample Delay(µsec)	533
Sample Interval(µsec)	1
Number of Samples	800

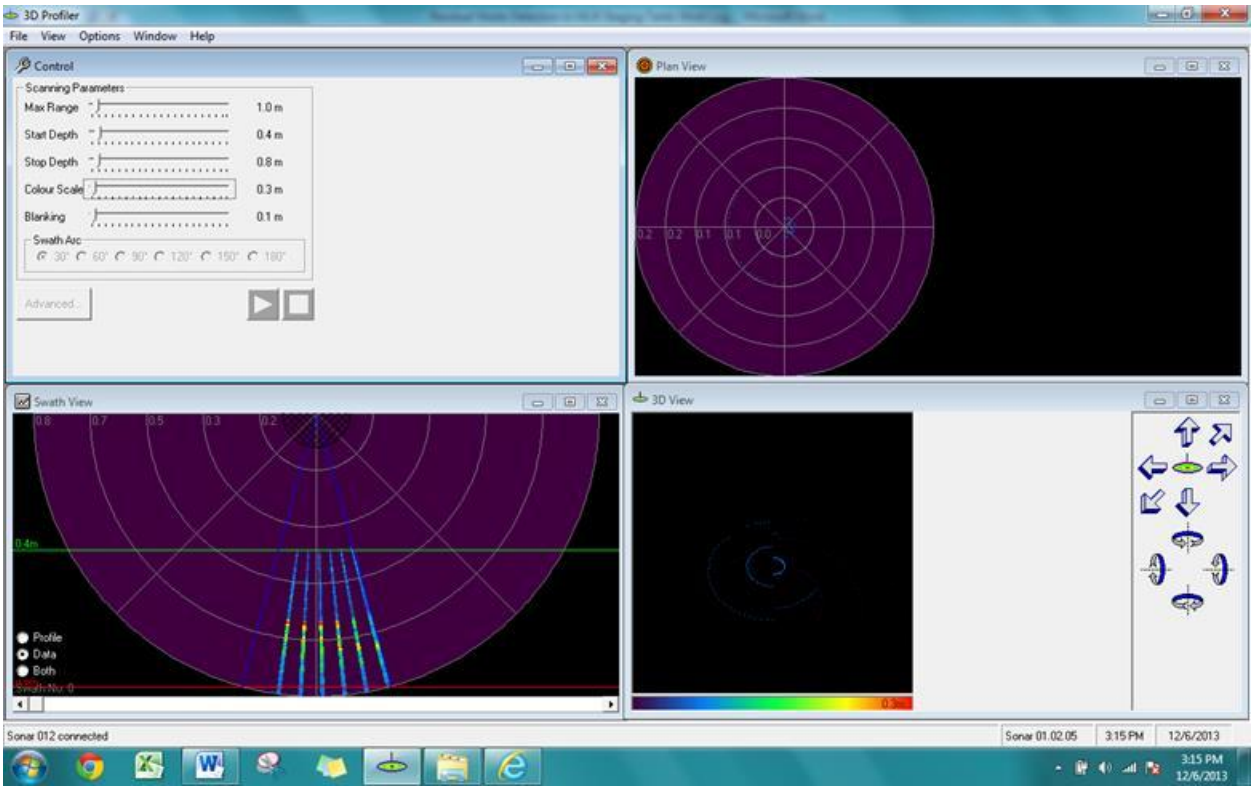

Figure 54. Scan at the lowest resolution imaging settings.

The sonar was tested at the highest and lowest resolution settings. The high resolution scan takes more time than allowed for scanning during a PJM cycle. At the lowest resolution setting, the sonar software will not interpolate the data and create a 3-D image. The software does, however, collect the data into an ASCII file which can be imported into external mapping algorithms. The first algorithm was initially tested using the sonar image in the high resolution image to validate its accuracy. The algorithm was then used to generate maps of the low resolution sonar data. Figure 55 shows the sonar graphical user interface for the high resolution image. Figure 56 shows 3 different views of the 3-D brick and tank bottom surface using the 3-D mapping algorithm. The images are the same, that is, the spatial dimensions for location and size of the brick imaged is the same for the commercial sonar imaging as the algorithm selected to manually image the object.

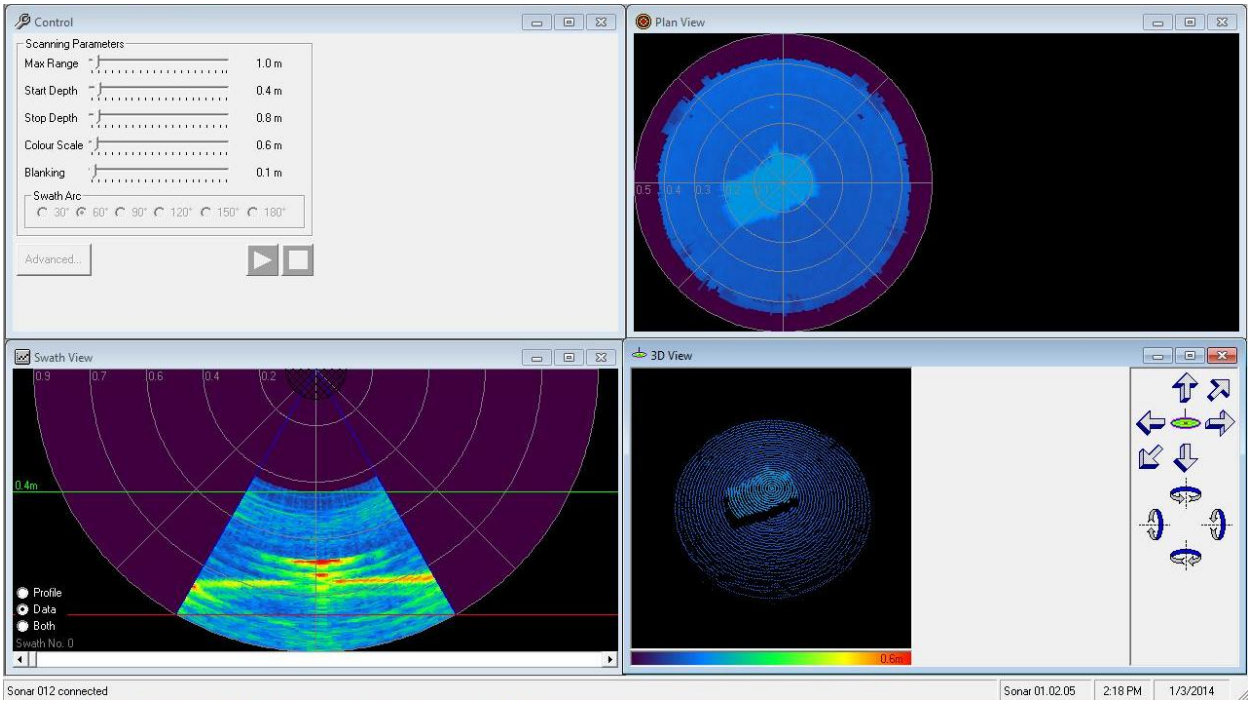

Figure 55. High resolution sonar image using software graphical user interface. The 4 views include: sonar settings, top view, side view and a 3-D map of the brick in the bottom of the test tank.

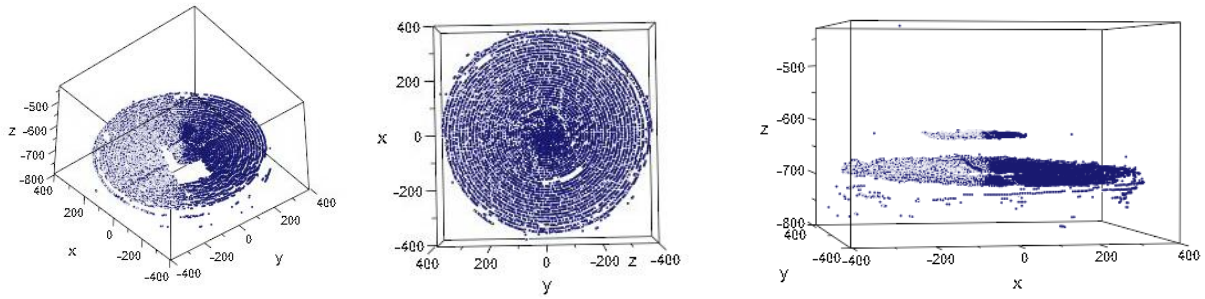

Figure 56. High resolution images from FIU's 3D mapper.

The low resolution image from the sonar's graphical user interface shows the 4 swaths the sonar obtained from the tank bottom but no images were generated (see Figure 57). Figure 58 shows the 3D plots obtained from the external mapping algorithm. To estimate the volume of those solids in certain floor areas, FIU will improve the 3-D mapping to allow for more robust interpolation of points between the individual sonar swaths.

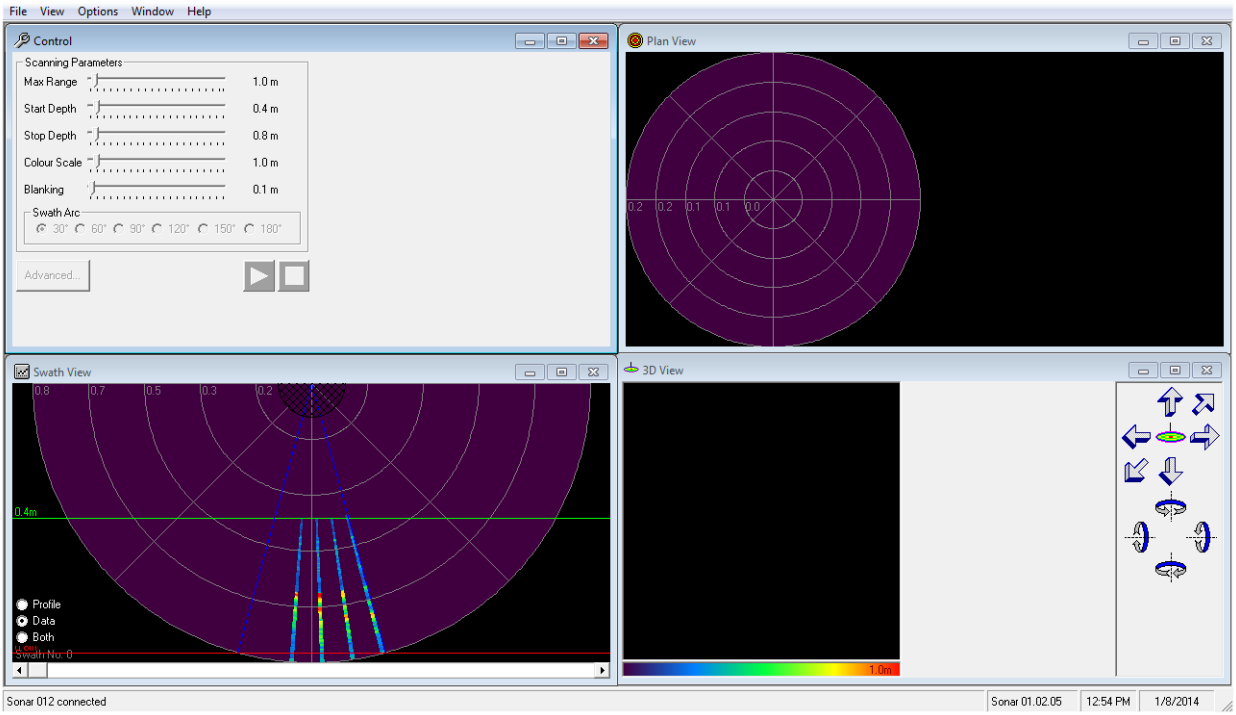

Figure 57. Low resolution image – commercial sonar cannot create an image with low density of data points.

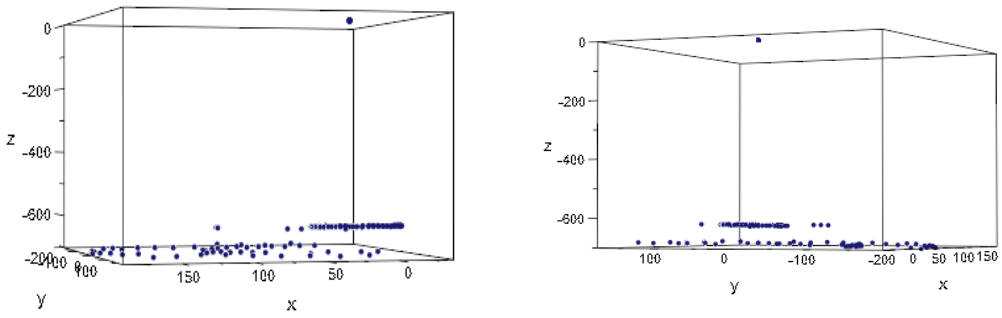

Figure 58. Low resolution plots from 3D mapper.

Bench-scale testing of the SLIM sonar has been successful and is completed. The ability to scan in 15-60 second periods does yield results that can be imaged and that allow an operator to know if any solids are on the tank floor.

Key control parameters for the short sonar scans include: swath angle, swath step size and rotation step size. For the initial lab-scale testing, the object scanned in water was a brick with known dimensions and volume. The test matrix and accuracy for this study is provided in Table

13. Note that all errors are 8.65% +/- 1.25%. Figure 59 shows a typical contour map of the brick that was used to estimate the volume.

Table 13. Test Results for 6 Optimal Sonar Settings

Trial #	Time for Scan	Swath Motor Step setting	Rotate Motor Step setting	Swath Arc	Solid Vol. Accuracy (+/-)
1	~45 Seconds	1	3	30	+9.1%
2	~24 Seconds	1	7	30	+7.9%
3	~19 Seconds	1	10	30	+9.9%
4	~32 Seconds	3	3	30	7.4%
5	~19 Seconds	3	7	30	8.1%
6	~15 Seconds	3	10	30	9.3%

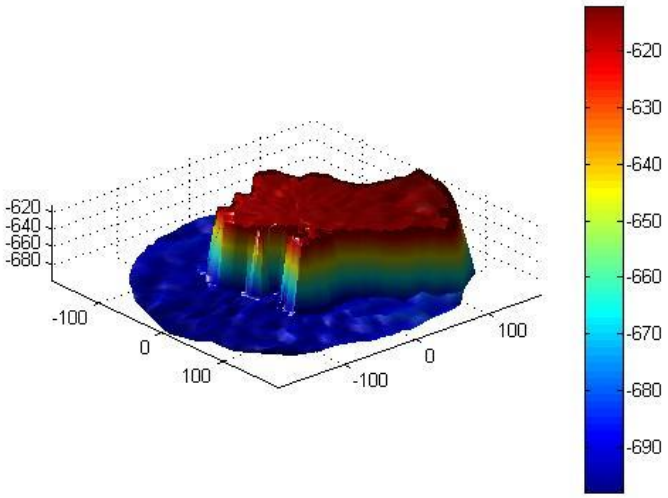

Figure 59. Trial 1 – Post-Process: 9.1% larger than original brick.

The Phase II (pilot-scale) test plan of SLIM's 3-D sonar was developed during March and April and sent to key Hanford HLW and DOE EM personnel on April 25th. Input from Hanford and DOE EM HQ personnel was incorporated into the final Phase II test plan.

The tank used in earlier bench-scale and phase I testing (described above) was not sufficient in size and accessibility for what is required in Phase II (pilot-scale) testing. A larger tank (74 in

dia. and 84 in ht.) has been placed in the FIU ARC High Bay research area. Preparation of the Phase II experimental set up or testbed has been initiated. Baseline testing without mixing suspended solids was completed. Kaolin clay, a HLW particulate simulant, will be ordered in July and additional objects shaped more like settled solids surfaces are under design. Set up for Phase II testing will continue in parallel with the development of the test plan and will be ready for testing later during FIU Year 5 (May 2014 – May 2015).

Software for automating the analysis and input of sonar data into imaging software has been developed and needs refinement. In addition, specific data filters developed and/or tested include:

1. A minimum time filter to remove scatters sometimes seen around the sonar head;
2. A maximum time filter based upon tank dimensions and angle that will eliminate most double scattered sonar pings which show as points beyond a surface;
3. A nearest neighbor analyses that eliminates most sonar pings that scatter from particulates suspended in the water tank (important when mixing adds up to 30% by volume of solids to the water in the tank); and
4. Smoothing functions for interpolation of 2-D sonar slices into quality 3-D images even in sparse datasets (i.e., less than five, 2-D sonar slices contributing to the sonar image due to short times available for imaging).

Depicted below in Figure 60 are images created by two additional processing filters for sonar data. The image is that of a standard brick. Filtering is needed to allow for automated analysis of the absence of the settled solids in the bottom of the mixing tanks at Hanford. Should there be settled solids during mixing then the mixing operations engineer would either increase the energy of the PJMs or possibly allow for more time for all solids to become mixed.

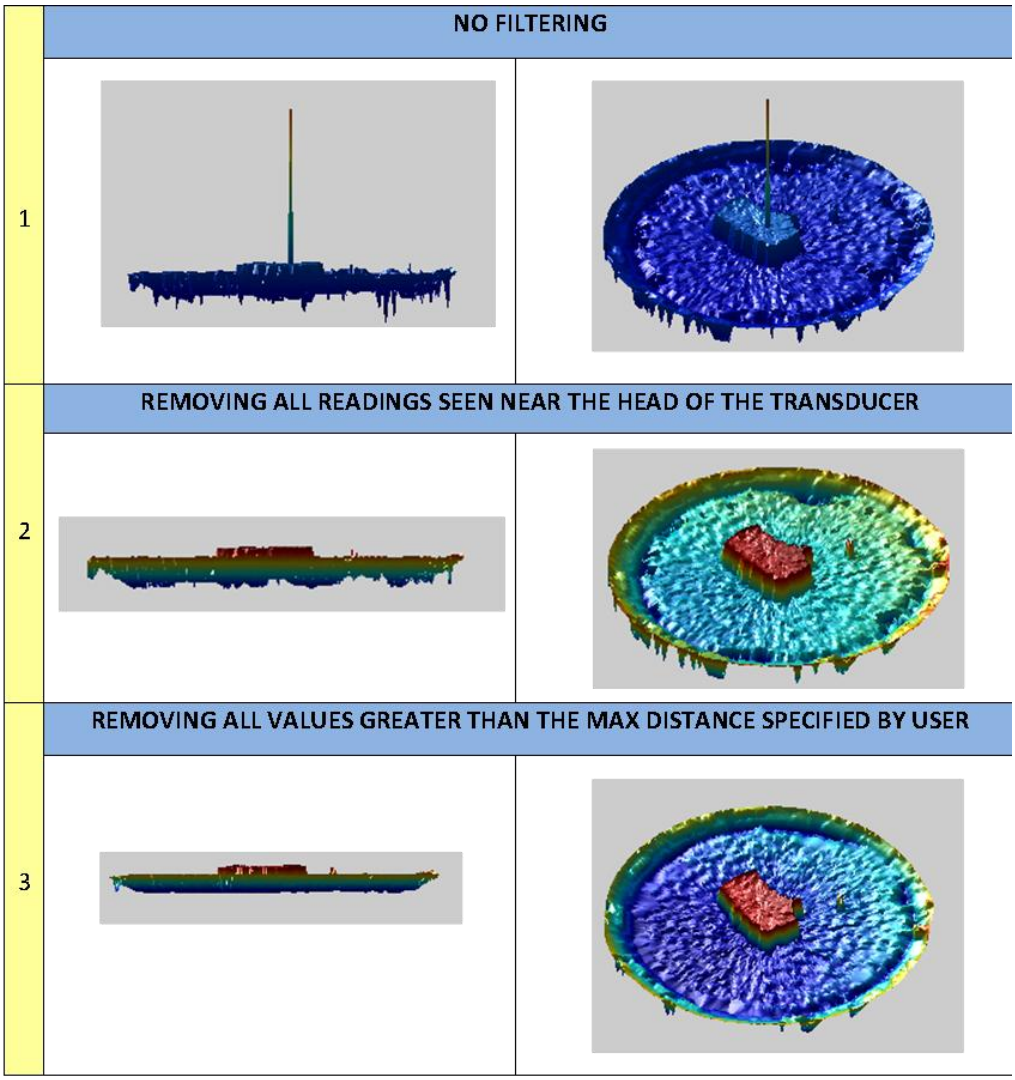

Figure 60. Results of a few sonar data filtering techniques.

CONCLUSIONS AND FUTURE WORK

FIU successfully demonstrated the proof of concept for the application of the solid-liquid interface monitor (SLIM) in mixing tanks for short imaging time periods (< 1 minute). A milestone report was submitted to DOE EM that contained the research and technology testing results. With the successful bench-scale testing of the sonar, FIU shifted focus to Phase II testing, improving data filters and improving the image resolution. The pilot-scale test plan for SLIM was completed next in consultation with DOE and Hanford Site project contacts. The goal for this final testing of SLIM is to show that the technology will meet all functional requirements for a technology deployment in a high-level radioactive waste mixing tank. The functional requirements will include data quality objectives for the accuracy, speed and other performance needed of the SLIM mechanical deployment and sonar imaging systems. The functional requirements will also include safety analyses, deployment and operating procedures, and other requirements needed for any technology deployed in high-level radioactive waste at Hanford. As the Phase II testing progresses, it is expected that additional tests will be requested by Hanford engineers either to improve its likelihood of deployment or to address engineering safety or other concerns in the deployment and operation of the system. Phase II testing will be completed in April 2015. Phase III operational testing is contingent upon successful Phase II testing and Hanford engineers' continued willingness to apply SLIM for their need to monitor PJM mixing effectiveness. Phase III would follow after of all results from Phase II are analyzed and DOE Hanford Site engineers develop a complete set of functional requirements. During 2015, it is envisioned that a Hanford HLW mixing tank will be identified that would benefit from the deployment of the SLIM technology.

TASK 18.2 FY13 YEAR END TECHNICAL REPORT
Development of Inspection Tools for DST Primary Tanks

EXECUTIVE SUMMARY

Recently, small amounts of waste have been found in the annulus of AY-102, prompting the need for developing inspection tools that can identify the cause and exact location of the leak. Three separate access paths can be used to obtain information regarding the tank bottom condition. This includes: 1) refractory air slots though the annulus, 2) 4-in. annulus air supply pipe to central air slots, and 3) 6-in. leak detection pit drain from the central sump. FIU has been requested to investigate developing a technology that will utilize the access through the annulus into the refractory air slots and provide visual feedback of the condition within the air slots. The refractory air slots range from 1 inch to 3 inches in width and provide a complex maze to navigate through, including four 90° turns to reach the center of the tank.

Based on design requirements provided by engineers at Hanford, a design was proposed that consists of a small tank type body which can house a camera and the necessary motors that propel the wheels and tank tread. To avoid existing debris in the air slots and potentially damaging the refractory pad, the proposed design has magnets placed at the base of the unit which allows it to move upside-down along the bottom of the carbon steel tank.

To demonstrate the concept, FIU has developed a 2D simulation model in Abaqus that can be used to make design modifications in a virtual environment. In order to develop the design and obtain initial specifications for the 2D simulation model, information on commercially available off-the-shelf components was compiled. The tool was modeled using four rigid bodies: two for the wheels, one for the tool body, and one representing the tank floor. Additionally, a flexible body was used to model the track that fits around the wheels. The inspection tool body encompasses the weight of all of the components except for the tether, wheels and track. To obtain an initial approximation for the weight in the simulation, the weight for two motors, magnets and a camera were used. Other system properties obtained and provided as input to the model included coefficients of friction, magnet strength and hypereleastic constants.

The length that the inspection tool can travel will be limited by the drag force created by the tether (for video feedback and control). Results from the simulation demonstrated that a maximum pulling force of 2.888 lb was achieved when applying a torque of 0.089 in-lb. Torques greater than the maximum value did not provide higher pulling forces due to slippage of the wheel and the track.

Future work will include determining estimates for the tether size and associated drag forces. These estimates will be incorporated into the simulation, allowing for optimization of motor size, tread dimensions, magnetic forces, etc. After the tether drag forces have been determined, a first prototype design will be provided for approval by the site and a first prototype will be manufactured. The prototype will demonstrate how the device will maneuver in the complex configuration within the air slots of the refractory pad.

INTRODUCTION

Recently, small amounts of waste have been found in the annulus of AY-102, prompting the need for developing inspection tools that can identify the cause and exact location of the leak. Three separate access paths can be used to obtain information regarding the tank bottom condition. This includes: 1) refractory air slots though the annulus, 2) 4-in. annulus air supply pipe to central air slots, and 3) 6-in. leak detection pit drain from the central sump. Tank operation contractors at Hanford have identified four vendors to develop or utilize off-the-shelf technologies that can maneuver through the pathways and provide visual feedback of the conditions in the DST bottoms. Vendor presentations were provided to the tank operation contractors demonstrating the approaches to be used; however, the contractor has not been able to provide continued support to this effort. This summary report provides a description of a concept developed by FIU with input from engineers at WRPS and a dynamic model/simulation to demonstrate the principles of how the inspection tool will function. The model will also provide a platform to conduct tests and make design modifications in a virtual environment.

FIU has been requested to investigate developing a technology that will utilize the access through the annulus into the refractory air slots (Figure 61) and provide visual feedback of the condition within the air slots. The refractory air slots range from 1 inch to 3 inches in width and provide a complex maze to navigate through, including four 90° turns to reach the center of the tank (Figure 62).

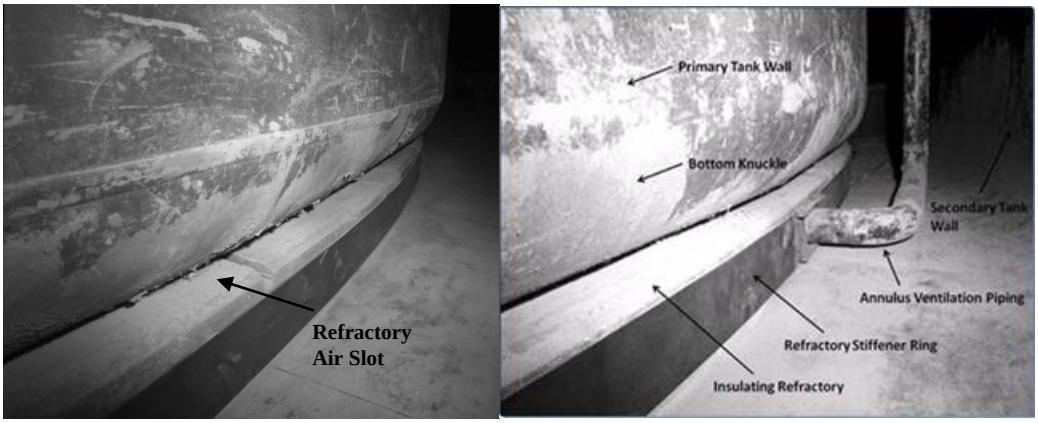

Figure 61. Side view of primary tank and refractory air slot.

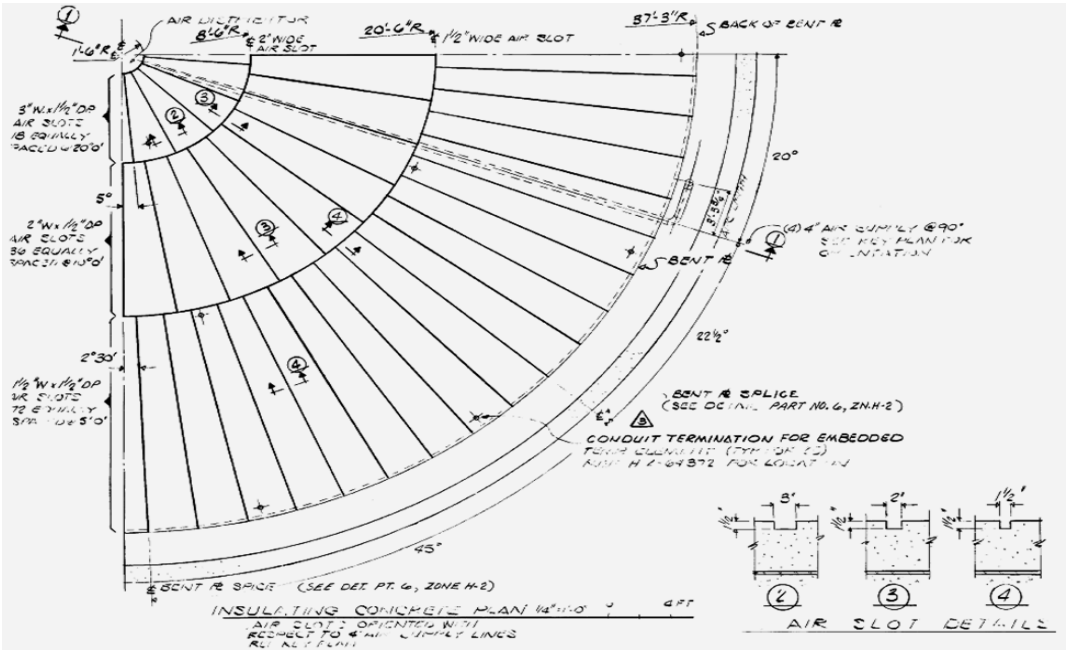

Figure 62. Refractory air slot layout and description.

In conjunction with site engineers, FIU has gathered information that has been used to establish the design specifications for the inspection tool. This includes annulus and refractory air slot geometry and maximum temperature and radiation limits for the device. Discussions with the engineers on the condition of the carbon steel along the tank bottom led to the viewing of refractory air channel video inspections for tanks AW-101, AZ-102, and SY-103 that were performed ten years ago with an articulated robot inside the annulus. The video provided FIU with a general idea of the conditions that will be encountered in the air channels, as well as the primary tank bottom surface condition. The video also provided FIU with a better understanding of the refractory pad's low shear strength and how easy it is to create debris (Figure 63).

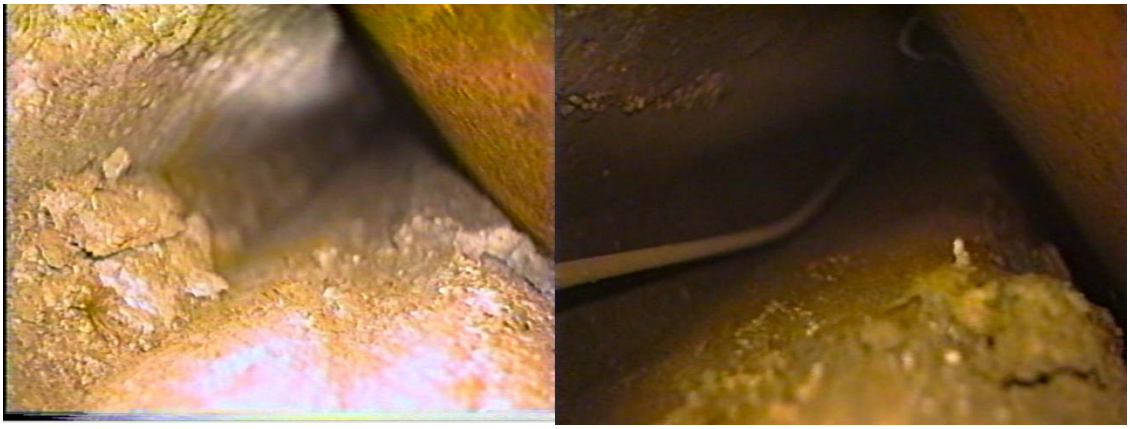

Figure 63. Debris seen in refractory air slots.

ENGINEERING APPROACH

Design Concept

The objective of the design tool is to provide a means for Hanford engineers to inspect the primary tank bottom of AY-102 by navigating the device through the air slots in the refractory pad. Specific requirements for the design include:

1) Deploy at annulus base through riser (42 inch diameter) into a refractory slot opening
2) Navigate up to 38 feet to the center of the tank through slots that have a 1-inch height and vary from 1.5, 2 and 3 inches in width
3) Navigate through four 90° turns
4) Minimize damage to the refractory pad
5) Provide visual feedback of the tank bottom and refractory slots
6) Provide a means for removal in the event of a malfunction of the inspection tool
7) Tolerate exposure to elevated temperature and radiation levels (170 F, 85 rad/hr)

The proposed design consists of a small tank type body that can house a camera and the necessary motors that propel the wheels and tank tread. To avoid existing debris in the air slots and potentially damaging the refractory pad, the proposed design has magnets placed at the base of the unit which allows it to move upside-down along the bottom of the carbon steel tank.

Through discussion with WRPS engineers, an important aspect of the inspection tool is the live video stream so that distance traveled can be easily correlated with the video, and any obstructions at those distances can be dealt with. It was also concluded that a tether was needed for the inspection tool as a full-proof method to retrieve the tool in the event of a malfunction. For this inspection tool, the tether will consist of a camera fiber optic line and a control/power feed for steering and navigation.

Figure 4 shows a 3D rendering of the proposed inspection tool as it would be oriented upside-down along the tank bottom. Figure 65 shows an additional view with the internal components exposed including the two motors and the gears. All of the components must be confined within the housing in such a way that the spacing allows for the proper operation of all components. Figure 66 shows the orientation and relative positioning of the components in the design during assembly. The housing that will be utilized consists of three sections that can be assembled together and will be used to encase the components. Initially, the gears and motors will be set into the bottom of the right and left segments of the housing and then the camera will be set into place. The right and left sections will close shut to encase all components and prevent unwanted movement. Finally, the top housing section will be placed to complete the prototype.

Figure 64. Rendering of the proposed design.

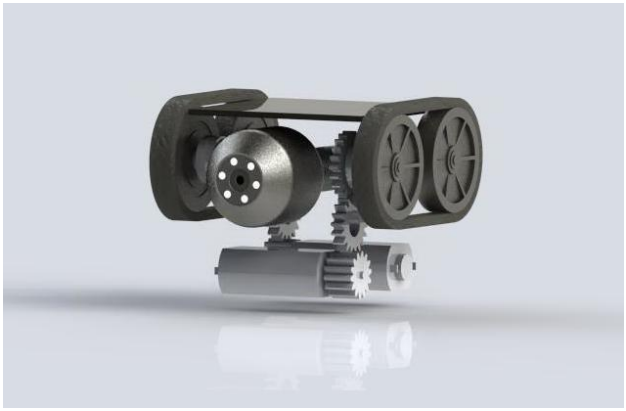

Figure 65. View of the internal components.

Figure 66. Rendering showing the assembly.

Motors contained in the body are attached to one wheel on each side and drive the opposite wheels via a rubber track. Having two motors will allow each side of the tool to operate independently and provide the means to navigate around turns in the refractory slots. A dimensional analysis has been conducted to verify that the unit can navigate through a 90-degree turn in the refractory slots. Gears have also been included to increase the torque from the motors

which will be needed to overcome the axial magnetic force and drag from the tether. The previous figures also show the camera housed in the body of the inspection tool which will include a line to provide live visual feedback. The tether will also control and provide power for the two motors. In the event that the tool malfunctions or reaches an obstruction in the air channel, the tether can be used to retrieve the device.

In order to develop the CAD drawings and obtain initial specifications for the 2D simulation model, FIU compiled information on commercially available off-the-shelf components. This information is contained within the tables below.

Table 14. Magnet

K & J Magnetics, Inc						*www.kjmagnetics.com*		
Catalog Number	**Material**	**Max Operating Temp**	**Length**	**Width**	**Thickness**	**Distance from Tank**	**Pull Force**	**Total Price**
BXOX01	Nickel Plated	176°F	1in	1in	0.0625in	0.03in	4.12 lb	$2.57

Table 15. Motor

Digi-Key Corporation						*www.digikey.com*		
Catalog Number	**Torque (mNm)**	**Outside Diameter**	**Length**	**Voltage Range**	**Weight**	**Unit Price**	**Quantity**	**Total Price**
P14350-ND	0.1	0.315	0.413in	1 ~ 3.5 VDC	0.006lb	$4.07	2	$8.14

Table 16. Camera

Advanced Inspection Technologies						*http://aitproducts.com/*			
SKU	**Diameter**	**Tether Length**	**Power**	**Material**	**Output**	**Operating Temperature**	**Bends**	**Lighting**	**Unit Price**
MINCORD	0.51in	100ft	AC/DC	Stainless Steel Housing / Sapphire Lens	USB Output / Video	69°F-140°F	Yes (90°)	12 White LED	$4,000

Table 17. Wheel and Tank Track

Precision Industrial Components						*http://www.pic-design.com/*	
Catalog Belt Series	**Pitch**	**Reinforcement Cable Diameter**	**Positional Accuracy**	**Wheel Diameter**	**Body Material**	**Reinforcement**	**Operating Temperature**
MINCORD	Single Core	.032	Excellent	.55in	Polyurethane	Stainless Steel or Aramind Fiber	-65°F to 180 °F

Table 18. Gears

Stock Drive Products/Sterline Instrument a Designatronics, Inc						*www.sdp-si.com*	
Catalog Number	**Teeth**	**Inner Diameter**	**Pitch Diameter**	**Outside Diameter**	**Bore Size**	**Face Width**	**Material**
A 1B 1-Y64014	14	0.1797	0.219	0.25in	0.0393701	0.1	303 SS
S1163Z-064S018	18	0.2397	0.2813	0.3125	0.1248	0.1	303 SS
S1163Z-064S021	21	0.2866	0.3281	0.3593	0.1248	0.1	304 SS

Table 19. Bearings

Stock Drive Products/Sterline Instrument a Designatronics, Inc					*www.sdp-si.com*		
Catalog Number	**Bore Size**	**Outside Diameter**	**Overall Width**	**Flange**	**Unit Price**	**Quantity Needed**	**Total Price**
S9912Y-UBM-1	0.1248	0.25	0.094	NO	13.05	10	$130.50

The resulting overall dimensions of the inspection tool design based on the information in the above tables are 1.295 in (width), 1.095 in (height) and 1.3 in (length) from wheel to wheel.

Model Development

In order to properly size the components, FIU has developed a 2D dynamic finite element analysis model. As mentioned previously, this model will serve as a virtual testing environment, allowing FIU engineers to optimize the design. Specifications used to develop the initial design in the dynamic model were obtained from the commercial information shown in Table 14-Table **19**.

The tool was modeled using four rigid bodies: two for the wheels, one for the tool body, and one representing the tank floor. Additionally, a flexible body was used to model the track that fits around the wheels. The inspection tool body encompasses the weight of all of the components except for the tether, wheels and track. To obtain an initial approximation for the weight in the simulation, the weight for two motors, magnets and a camera are used. Since the weight of the camera in

Table 16 was not available, an approximate value was obtained using the same weight as the camera in FIU's peristaltic crawler. For the model, the total weight of the inspection tool body was converted to a distributed mass and defined as 0.0381913 lb/in. Gravity was defined as 32.2 ft/s^2.

The inspection tool will have four wheels, but in this 2D model only two wheels are defined as rigid bodies. To obtain initial simulation results, mass and inertial properties were not used, only the dimensions of the wheels. Constraints were added that define the wheels rotational motion relative to the inspection tool body. An applied torque on the rear wheel was used to model the motor output. Since two motors will be used in the actual tool, the input torque was doubled. For this simulation, the weight of the gears have not been included.

Similarly, two tracks will be used for the inspection tool, one around two wheels on each side of the vehicle. For the 2D model, one track was modeled with twice the width of a single track. This will provide appropriate friction and traction forces for the system. The track is modeled as a hyperelastic body which was approximated using a Neo-Hookean numeric technique with coefficients corresponding to natural rubber material ($C_1 = 1.79 \times 10^{-4}$ psi and $D_1 = 109.21$ psi). The rubber track was modeled using 450 quad elements that provided information on the stress and strain of the track as the wheels rotate. The tank bottom was incorporated into the model as a fixed rigid body with no inertial properties. Friction between the tank wheels and the track and

the track and the tank bottom was also modeled. Standard coefficient of friction values for rubber and carbon steel and for rubber and plastic were used (0.5 and 0.3).

Magnets are used to produce the force necessary to keep the track in contact with the tank and assist in developing the traction force used to propel the tool. In the model, a force has been added to the inspection tool body to emulate the magnetic force between the tank and the inspection tool. Initial force values used in the simulations was based off specifications from off-the-shelf magnets (2 lb/in^2).

The modeling steps for the dynamic simulation included six consecutive steps. Steps one and two involved a pre-tensioning phase where the rubber track was expanded by separating the wheels to provide a realistic stress distribution. In step three, the inspection tool was positioned in contact with the bottom of the tank and in step four, the magnetic force was engaged. In steps five and six, torque was applied to the rear wheel and an increasing force was applied to the tether.

RESULTS & DISCUSSION

Using applied torque values ranging from 0.01118 in-lb to 0.1.006 in-lb, values for the maximum pulling forced developed by the inspection tool were generated. The maximum pulling force attained was 2.888 lb. Figure 67 shows a plot of the maximum pulling forces corresponding to their torque applied on step five of the simulation. These force values can be used to determine how much tether can be pulled by the inspection tool.

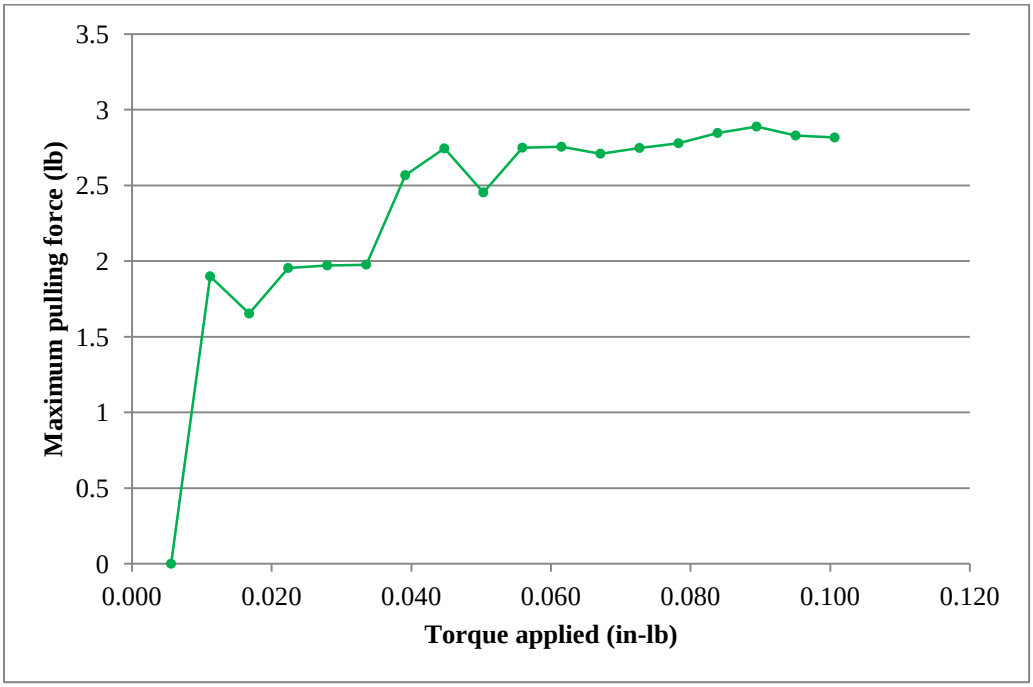

Figure 67. Maximum pulling forces achieved.

Figure 68 shows a sample simulation of the inspection tool as it translates along the bottom of the tank. The stress in the tank tread is provided, since it is the only flexible body in the model. If the maximum pull force of the unit is exceeded, the unit will stall and, with the wheels rotating in a forward direction, the unit will begin to slide backwards.

Figure 68. Inspection tool translating along tank bottom.

CONCLUSIONS

A dynamic simulation model was developed for the proposed inspection tool that will provide video feedback of the AY-102 tank floor and refractory pad. Results from the simulation showed that a maximum pulling force of 2.888 lb was achieved when applying a torque of 0.089 in-lb. Torques greater than the maximum value do not provide higher pulling forces due to slippage of the wheel and the track.

FIU will utilize the model developed to finalize the components (camera, motors, gears, wheels, etc.) in terms of space and load requirements obtained from simulations and drawings. More specifically, estimates for tether size and associated drag forces will be incorporated into the simulation, allowing for optimization of motor size, tread dimensions, magnetic forces, etc. Essentially, any design modifications can be easily incorporated into the model which will be used as a virtual simulator – allowing us to make design changes and understanding the overall ramifications of the changes.

After estimates for tether drag forces have been determined, a first prototype design will be provided for approval by the site and a first prototype will be manufactured. The prototype will demonstrate how the device will maneuver in the complex configuration within the air slots of the refractory pad. The materials for the first prototype will not meet the temperature and radiation specifications, but will provide the foundation for optimizing the size and weight of the components and demonstrate that the power needed to drive the unit is met. A bench scale testbed emulating the geometry of the air slots will be created for testing and demonstration of the concept.

After the first prototype has been designed and validated, a second prototype will be designed with feedback from Hanford engineers. The second prototype will be manufactured with materials that meet all design specifications and will include a video camera with a fiber-optic line for real-time viewing. Testing of the second unit will again be conducted on a bench scale testbed. The navigation and maneuverability of the prototype will be evaluated in addition to its ability to pull the video camera line. If the second prototype is successful, the next step would be to demonstrate the unit's inspection viability onsite, possibly in AY-101 which has a similar tank design and refractory pad as AY-102.

TASK 19.1 FY13 YEAR END TECHNICAL REPORT
Pipeline Corrosion and Erosion Evaluation

EXECUTIVE SUMMARY

Washington River Protection Solutions (WRPS) has implemented a fitness-for-service program which will evaluate the degraded condition of the tank farm waste transfer system. The Tank Farms Waste Transfer System Fitness-for-Service Requirements and Recommendations, includes a requirement to inspect primary piping, encasements, and jumpers for corrosion/erosion.

As part of this study, several jumpers from the 242-A Evaporator Pump room and the AW-02E Feed Pit were removed and inspected via ultrasonic thickness measurements. The jumpers in the 242-A Evaporator Pump room included 18-4, C-4&5, J-13A, 13-K, and 19-5. All of these jumpers were removed permanently except for jumper 19-5 which will be reinstalled for further service. The jumpers from the AW-02E Feed Pit included 1-4 and B-2.

This task provides analysis for the aforementioned jumpers as well as the estimated remaining useful life for the components based on the wall thinning measured (ultrasonic thickness). This analysis includes wear trends and correlations with the volume of fluid transferred.

Jumper 18-4 has not transferred any waste and can be used as a baseline for comparing C-4&5 and 19-5 which transferred approximately 11 and 42 Mgal of slurry, respectively. Average thickness measurements for the sections in Jumper 18-4 were slightly above the manufacture's nominal thickness. Average thicknesses for the sections evaluated in Jumper C-4&5 were very similar with only Straight-5 having an average thickness of 0.001 inch below nominal. This suggests that no erosion has occurred in Jumper C-4&5.

Jumpers J-13A and 13-K transferred approximately 29 and 86 Mgal of supernatant, respectively. Average thicknesses for the sections evaluated in Jumper J-13A were slightly different, demonstrating that there was no erosion trend. Average thickness measurements for the sections in Jumper 13-K were all above the manufacture's nominal thickness and in three of the sections, significantly above nominal. Jumper 13-K transferred approximately three times the supernatant that Jumper J-13A transferred, yet did not have any component below the manufacturer's nominal thickness. This suggests that the variations observed are not due to erosion.

Jumper 1-4 transferred at least 17 Mgal of feed waste in addition to an unknown amount of recirculation waste. This uncertainty makes it difficult to assess erosion trends between the two jumpers. Regardless, average thickness measurements for the sections analyzed for both the 1-4 and B-2 jumpers were above the manufacturer's nominal values.

INTRODUCTION

Washington River Protection Solutions (WRPS) has implemented a fitness-for-service program which will evaluate the degraded condition of the tank farm waste transfer system. The Tank Farms Waste Transfer System Fitness-for-Service Requirements and Recommendations [1], includes a requirement to inspect primary piping, encasements, and jumpers for corrosion/erosion.

The 242-A Evaporator Pump room was upgraded by adding instrumentation to the feed and return jumpers, prior to running the next campaign. As part of this upgrade, several jumpers were removed for disposal and a total of five jumpers were selected for ultrasonic thickness (UT) inspection. The jumpers selected were the following: 18-4, C-4&5, J-13A, 13-K, and 19-5. All of these jumpers will be removed permanently except for jumper 19-5 which will be reinstalled for further service. The UT measurements collected from jumper 19-5 will assist in future 242-A integrity assessments.

As part of this study, several jumpers from the AW-02E Feed Pit were also removed for disposal and two were selected for ultrasonic thickness (UT) inspection. The jumpers selected were the 1-4 and B-2 which were packaged and sent to the 222-S Laboratory for UT assessments [2].

This section provides a summary of the analysis for the jumpers listed above as well as the estimated remaining useful life (ERUL) for its components based on the wall thinning measured. This analysis is based on the ultrasonic thickness measurements of the jumpers and includes wear trends and correlations with the volume of fluid transferred. The complete reports for the jumpers are provided in documents prepared by McDaniel [3, 4].

242-A EVAPORATOR PUMP ROOM JUMPERS

Jumper 19-5

Jumper 19-5 is a 2-in Schedule 40 ASTM A312 TP 304L stainless steel pipe located in the 242-A Evaporator Room positioned between connector 5 and connector 19. In a span of 30 years, it transferred approximately 42 Mgal of slurry. As part of the Tank Farms Waste Transfer System Fitness-for-Service Program, four sections of the jumper have been evaluated via ultrasonic thickness measurements. These sections include Elbow-3, Elbow-4, Straight-3 and Straight-4. Table 20 provides a summary of the average thicknesses measured for each section and the nominal and minimum manufacturing thickness. In all cases, the average thickness was greater than the minimum thickness; however, for three of the four sections, the average thickness was less than the nominal thickness. Trends associated with the thickness measurements for the sections were significantly different and not consistent with erosion patterns. Additionally, the differences between the maximum and minimum thickness values were minimal, suggesting that any thicknesses below nominal values are due to variations from manufacturing. Even though the analysis does not indicated erosion occurred, ERULs for three sections (Elbow-3, Straight-3, Straight-4), were determined based on the volume of slurry transferred and a minimum allowable thickness. Table 21 provides the amount of volume required to reach the minimum allowable thickness as well as the erosion rate for each section. Based on these measurements and estimations, Jumper 19-5 ERUL will significantly extend beyond its expected life in terms of flow volume transferred.

Table 20. Thicknesses Summary for Each Section of Jumper 19-5

Section	Average Thickness (in)	Manufacturer's Nominal Thickness (in)*	Minimum Manufacturing Thickness (in)*
Elbow-3	0.149	0.154	0.135
Elbow-4	0.161	0.154	0.135
Straight-3	0.147	0.154	0.135
Straight-4	0.150	0.154	0.135

*Information is based on straight carbon steel pipes

Table 21. ERUL and Erosion Rate for Each Section of Jumper 19-5

Section	Volume Required for Minimum Thickness (Mgal)	Erosion Rate (in/Mgal)
Elbow-3	1103.8	-1.151E-4
Straight-3	752.4	-1.675E-4
Straight-4	1309.9	-9.619E-5

Jumper C-4&5

Jumper C-4&5 is a 2-in Schedule 40 ASTM A312 TP 304L stainless steel pipe located in the 242-A Evaporator Room. Since 1992, it transferred approximately11 Mgal of slurry. As part of

the Tank Farms Waste Transfer System Fitness-for-Service Program, four sections of the jumper have been evaluated via ultrasonic thickness measurements. These sections include Elbow-5, Straight-5 and Straight-6. Table 22 provides a summary of the average thicknesses measured for each section and the nominal and minimum manufacturing thickness. In all cases, the average thickness was greater than the minimum thickness; however, for one of the three sections, the average thickness was less than the nominal thickness. Thickness trends associated with radial averages for the straight sections were similar with small variances around the average thickness. The single elbow evaluated in this jumper did exhibit radial average thickness trends similar to the Elbow-3 in Jumper 19-5. Additionally, the differences between the maximum and minimum thickness values were minimal, suggesting that any thicknesses below nominal values are due to variations from manufacturing. Even though the analysis does not indicated erosion occurred, ERULs for Straight 5 was determined based on the volume of slurry transferred and a minimum allowable thickness. Table 23 provides the amount of volume required to reach the minimum allowable thickness as well as the erosion rate for the section. Based on these measurements and estimations, the Jumper C-4&5 ERUL will significantly extend beyond its expected life in terms of flow volume transferred.

Table 22. Thicknesses Summary for Each Section of Jumper C-4&5

Section	Average Thickness (in)	Manufacturer's Nominal Thickness (in)*	Minimum Manufacturing Thickness (in)*
Elbow-5	0.161	0.154	0.135
Straight-5	0.153	0.154	0.135
Straight-6	0.155	0.154	0.135

*Information is based on straight carbon steel pipes

Table 23. ERUL and Erosion Rate for Each Section of Jumper C-4&5

Section	Volume Required for Minimum Thickness (Mgal)	Erosion Rate (in/Mgal)
Straight-5	1398.6	-9.009E-5

Jumper 18-4

Jumper 18-4 is a 2-in Schedule 40 ASTM A312 TP 304L stainless steel pipe located in the 242-A Evaporator Room positioned between connector 4 and connector 2. This jumper was not used to transfer any waste and can be used as a baseline for similar jumpers. As part of the Tank Farms Waste Transfer System Fitness-for-Service Program, four sections of the jumper have been evaluated via ultrasonic thickness measurements. These sections include Elbow-1, Elbow-2, Straight-1 and Straight-2. Table 24 provides a summary of the average thicknesses measured for each section and the nominal and minimum manufacturing thickness. In all cases, the average thickness was greater than or equal to the manufacture's nominal thickness. As expected, there is no detectable wear for the 4 components of Jumper 18-4 and ERULs cannot be determined.

Longitudinal averages show different trends for each the elbows and straight sections around the circumference. This information assists in providing a reference of the variance in the

manufacturing of the pipe sections. Radial averages, however, were more consistent for both the elbows and the straight sections, showing very little variations in pipe thickness.

Table 24. Thicknesses Summary for Each Section of Jumper 18-4

Section	Average Thickness (in)	Manufacturer's Nominal Thickness (in)*	Minimum Manufacturing Thickness (in)*
Elbow-1	0.154	0.154	0.135
Elbow-2	0.172	0.154	0.135
Straight-1	0.155	0.154	0.135
Straight-2	0.155	0.154	0.135

*Information is based on straight carbon steel pipes

Jumper 13-K

Jumper 13-K is a 3-in Schedule 40 ASTM A312 TP 304L stainless steel pipe located in the 242-A Evaporator Room positioned between connector 13 and connector K. Since 1983, it transferred approximately 85 Mgal of supernatant. As part of the Tank Farms Waste Transfer System Fitness-for-Service Program, four sections of the jumper have been evaluated via ultrasonic thickness measurements. These sections include Elbow-6, Elbow-7, Straight-7 and Straight-8. Table 25 provides a summary of the average thicknesses measured for each section and the nominal and minimum manufacturing thickness. In all cases, the average thickness was greater than the manufacturer's nominal thickness and therefore, ERULs cannot be determined. Radial thickness trends were significantly different for the two straight sections but were similar for the elbows. Longitudinal average thicknesses were fairly constant for all the sections evaluated. Additionally, the differences between the maximum and minimum thickness values were minimal, suggesting that variations in thicknesses are due to manufacturing.

Table 25. Thicknesses Summary for Each Section of Jumper 13-K

Section	Average Thickness (in)	Manufacturer's Nominal Thickness (in)*	Minimum Manufacturing Thickness (in)*
Elbow-6	0.217	0.216	0.189
Elbow-7	0.232	0.216	0.189
Straight-7	0.227	0.216	0.189
Straight-8	0.228	0.216	0.189

*Information is based on straight carbon steel pipes

Jumper J-13A

Jumper J-13A is a 3-in Schedule 40 ASTM A312 TP 304L stainless steel pipe located in the 242-A Evaporator Room. Since 1983, it transferred approximately 29 Mgal of supernatant. As part of the Tank Farms Waste Transfer System Fitness-for-Service Program, three sections of the jumper have been evaluated via ultrasonic thickness measurements. These sections include Elbow-8, Straight-9 and Straight-10. Table 26 provides a summary of the average thicknesses

measured for each section and the nominal and minimum manufacturing thickness. In all cases, the average thickness was greater than the minimum thickness; however, for one of the three sections, the average thickness was less than the nominal thickness. There was no significant wear trend based on radial thickness averages for the straight sections. Radial thickness averages for the elbow were similar to other jumper elbows with a minor decrease at the edge. Additionally, the differences between the maximum and minimum thickness values were minimal, suggesting that any thicknesses below nominal values are due to variations from manufacturing. Even though the analysis does not indicated erosion occurred, a ERUL for Elbow-8 was determined based on the volume of supernatant transferred and a minimum allowable thickness. Table 27 provides the amount of volume required to reach the minimum allowable thickness as well as the erosion rate for the section. Based on these measurements and estimations, the Jumper J-13A ERUL will significantly extend beyond its expected life in terms of flow volume transferred.

Table 26. Thicknesses Summary for Each Section of Jumper J-13A

Section	Average Thickness (in)	Manufacturer's Nominal Thickness (in)*	Minimum Manufacturing Thickness (in)*
Elbow-8	0.209	0.216	0.189
Straight-9	0.218	0.216	0.189
Straight-10	0.228	0.216	0.189

*Information is based on straight carbon steel pipes

Table 27. ERUL and Erosion Rate for Each Section of Jumper C-4&5

Section	Volume Required for Minimum Thickness (Mgal)	Erosion Rate (in/Mgal)
Elbow-8	749.1	-2.403E-4

OVERALL ANALYSIS FOR 242-A EVAPORATOR PUMP ROOM JUMPERS

To accommodate the Tank Farms Waste Transfer System Fitness-for-Service Requirements and Recommendations 1, 5 jumpers from the 242-A Evaporator Pump Room have been evaluated via ultrasonic thickness measurements. Table 28 provides the type of material transferred, volume transferred and the diameter of each jumper.

Jumper 18-4 has not transferred any waste and can be used as a baseline for comparing C-4&5 and 19-5 which transferred approximately 11 and 42 Mgal of slurry, respectively. Average thickness measurements for the sections in Jumper 18-4 (one 5D elbow, one long radius elbow and two straight sections) were slightly above the manufacture's nominal thickness (see Table 24). Average thicknesses for the sections evaluated in Jumper C-4&5 (one long radius elbow and two straight sections) were very similar with only Straight-5 having an average thickness of 0.001 inch below nominal. This suggests that no erosion has occurred in Jumper C-4&5.

Table 28. Summary of Jumper Information for the 242-A Evaporator Jumpers

Jumper	Material Transferred	Volume Transferred (Mgal)	Jumper Diameter (in)
18-4	Slurry	0	2
C-4&5	Slurry	11	2
19-5	Slurry	42	2
J-13A	Supernatant	29	3
13-K	Supernatant	86	3

Jumper 19-5 has transferred approximately 4 times the volume that Jumper C-4&5 transferred. Average thickness measurements for Jumper 19-5 were also similar to the nominal thickness; however, three sections (one 5D bend elbow and two straight sections) were slightly below nominal (see Table 20). For these three sections, the ERULs were determined and the required transfer volume well exceeds the volume transfer required for the life of the plant. The 5D bend elbows from 18-4 and 19-5 had similar longitudinal averages with expected thinning at the extrados of the elbow due to the manufacturing process. The long radius jumpers from each of the three jumpers also showed the thinning at the extrados, but slight variations in thicknesses at the top and bottom of the elbows suggest that the variances observed are random and due to manufacturing processes. The straight sections from 18-4 had different trends associated with the average longitudinal measures. Straight-1 thickness averages were consistent around the circumference while Straight-2 had an increase towards the bottom. This demonstrates the potential variance that should be expected in terms of the manufacturing process, since 18-4 has not transferred any waste. Straight-5 and Straight-6 from Jumper C4&5 also had consistent averages around the radius with averages very similar to nominal. The straight sections in Jumper 19-5 showed very different longitude average trends, with Straight-3 slightly increasing as the position rotates clockwise and Straight-4 having an oscillatory trend as the position rotates clockwise. These variances are small and the trends do not suggest that erosion has occurred.

Jumpers J-13A and 13-K transferred approximately 29 and 86 Mgal of supernatant, respectively. Average thicknesses for the sections evaluated in Jumper J-13A (one long radius elbow and two straight sections) were slightly different with Elbow-8 being below nominal, Straight-9 being just above nominal and Straight-10 being significantly above nominal (see Table 26). The different averages for each section do not demonstrate an erosion trend for this jumper. Average thickness measurements for the sections in Jumper 13-K (one 5D elbow, one long radius elbow and two straight sections) were all above the manufacture's nominal thickness (see Table 25) and in three of the sections, significantly above nominal. Jumper 13-K transferred approximately three times the supernatant that Jumper J-13A transferred, yet did not have any component below the manufacturer's nominal thickness. This suggests that the variations observed are not due to erosion. The long radius elbows in J-13A and 13-K did have similar longitudinal average trends with thinning at the outer extrados; however t J-13A transferred a lower volume of supernatant, yet had the lower thickness average when compared with 13-K. This is not consistent with any type of erosion. The straight sections in 13-A had fairly consistent longitudinal averages around the circumference; however, on section was slightly above nominal and the other was significantly above nominal. Jumper 13-K straight sections were both significantly above nominal, but each section had different longitudinal average trends.

AW-02E FEED PUMP PIT JUMPERS

Jumper 1-4

Jumper 1-4 was manufactured with 3-in Schedule 40 ASTM A53 Type S Grade B or ASTM A106 Grade B carbon steel and was coated with Amercoat No. 187 primer followed by Amercoat No. 33 protective coating. It was located in the AW-02E Feed Pump Pit and has transferred approximately 17 million gallons of evaporator feed waste since 1997. It was also connected to the re-circulation loop and transferred an unknown amount of waste during any re-circulation processes. The exact amount of waste transferred through this jumper is unknown. As part of the Tank Farms Waste Transfer System Fitness-for-Service Program, seven sections of the jumper have been evaluated via ultrasonic thickness measurements. These sections include Elbow-1, Straight-1, Straight-2, Straight-3, Straight-4, Connector-1 and Connector-4. Table 29 provides a summary of the average thicknesses measured for each section and the nominal and minimum manufacturing thickness. In all cases, the average thickness was greater than the minimum thickness. Thickness trends for the straight sections are oscillatory in nature around the circumference and do not vary significantly along the axis of the pipe. Little variation in thickness is also observed with the connectors, indicating that erosion has not taken place. In general, the differences between the maximum and minimum thickness values were minimal, suggesting that any thicknesses measurements below nominal values are due to variations from manufacturing.

Table 29. Thicknesses Summary for Each Section of Jumper 1-4

Section	Average Thickness (in)	Manufacturer's Nominal Thickness (in)	Minimum Manufacturing Thickness (in)
Elbow-1	0.244	0.216*	0.189*
Straight-1	0.250	0.216	0.189
Straight-2	0.231	0.216	0.189
Straight-3	0.234	0.216	0.189
Straight-4	0.232	0.216	0.189
Connector-1	0.994	0.970	0.940
Connector-4	0.994	0.970	0.940

*Information is based on straight pipe sections

Jumper B-2

Jumper B to 2 was manufactured with a 3” schedule 40 pipe made of ASTM A53 Type S Grade B carbon steel and was coated with Amercoat No. 86 primer followed by Amercoat No. 33 protective coating. After being installed in 1980, it transferred approximately 42 Mgal of evaporator feed waste. As part of the Tank Farms Waste Transfer System Fitness-for-Service Program, seven sections of the jumper have been evaluated via ultrasonic thickness measurements. These sections include Elbow-1, Elbow-2, Straight-1, Straight-2, Straight-3, Connector-B and Connector-2. Table 30 provides a summary of the average thicknesses measured for each section and the nominal and minimum manufacturing thickness. In all cases, the average thickness was greater than the minimum thickness. Thickness trends for the straight

sections are oscillatory in nature around the circumference and vary minimally along the axis of the pipe. Little variation in thickness is also observed with the connectors, indicating that erosion has not taken place. Thicknesses in the elbows were smallest at the center locations of the extrados which is consistent with thinning due to rotary die bending. Compensation for the thinning showed more consistent data. In general, the differences between the maximum and minimum thickness values were minimal, suggesting that any thicknesses measurements below nominal values are due to variations from manufacturing.

Table 30. Thicknesses Summary for Each Section of Jumper B-2

Section	Average Thickness (in)	Manufacturer's Nominal Thickness (in)	Minimum Manufacturing Thickness (in)
Elbow-1	0.263	0.216*	0.189*
Elbow-2	0.246	0.216*	0.189*
Straight-1	0.233	0.216	0.189
Straight-2	0.236	0.216	0.189
Straight-3	0.231	0.216	0.189
Connector-B	0.988	0.970	0.940
Connector-2	0.994	0.970	0.940

*Information is based on straight pipe sections

OVERALL ANALYSIS FOR AW-02E FEED PUMP PIT JUMPERS

To accommodate the Tank Farms Waste Transfer System Fitness-for-Service Requirements and Recommendations 1, 2 jumpers from the AW-02E Feed Pump Pit Room have been evaluated via ultrasonic thickness measurements. Table 31 provides the type of material transferred, volume transferred and the diameter of each jumper.

Table 31. Summary of Jumper Information for the AW-02E Feed Pump Pit Jumpers

Jumper	Material Transferred	Volume Transferred (Mgal)	Jumper Diameter (in)
1-4	Feed Waste	17*	3
B-2	Feed Waste	42	3

* 1-4 transferred an unknown amount recirculation waste

Jumper 1-4 transferred at least 17 Mgal of feed waste in addition to an unknown amount of recirculation waste. This uncertainty makes it difficult to assess erosion trends between the two jumpers. Regardless, average thickness measurements for the sections analyzed for both the 1-4 and B-2 jumpers were above the manufacturer's nominal values. Similar trends were observed the straight sections in both jumpers. Longitudinal averages around the circumference of the pipe had thickness trends that were oscillatory but radial averages along the length of the pipe were fairly consistent. Of the three types of components analyzed, the connectors had the least amount of thickness variation. This was also true for both jumpers. The elbows did not show any consistent thickness trends for the two jumpers in terms of longitudinal averages. The radial averages for each of the elbows were all consistent along the length of the pipe.

REFERENCES

1. RPP-RPT-52206, (2012), *Tank Farms Waste Transfer System Fitness-for Service Requirements and Recommendations*, Becht Nuclear Services, Richland, Washington.
2. RPP-PLAN-55015 (Revision 0), (2013), *242-A Evaporator Jumper Ultrasonic Test Plan*, Washington River Protection Solutions LLC, Richland, Washington.
3. Erosion Analysis of Jumpers in the 242-A Evaporator Pump Room, Summary Report, Florida International University, Miami, FL.
4. Erosion Analysis of Jumpers in the AW-02E Feed Pump Pit, Summary Report, Florida International University, Miami, FL.

APPENDIX

The following report is available at the DOE Research website for the Cooperative Agreement between the U.S. Department of Energy Office of Environmental Management and the Applied Research Center at Florida International University: http://doeresearch.fiu.edu

1. Florida International University, *Project Technical Plan,* Project 1: Chemical Process Alternatives for Radioactive Waste.